BOUNDARY ELECTRON DOSIMETRY

BOUNDARY ELECTRON DOSIMETRY:

RADIOCHROMIC FILM MEASUREMENT AND MONTE CARLO SIMULATION

OF ELECTRON ABSORBED DOSE NEAR TISSUE INTERFACES

By

Fuad A. Khan, B.Eng.Mgt., P.Eng.

A Project

Submitted to the School of Graduate Studies

in Partial Fulfilment of the Requirements for the Degree

Master of Science

McMaster University

MASTER OF SCIENCE (1995) McMaster University

(Physics) Hamilton, Ontario

TITLE: BOUNDARY ELECTRON DOSIMETRY: RADIOCHROMIC FILM MEASUREMENT AND MONTE CARLO SIMULATION OF ELECTRON ABSORBED DOSE NEAR TISSUE INTERFACES

AUTHOR: Fuad A. Khan, B.Eng.Mgt. (McMaster University)

SUPERVISOR: Dr. C. S. Kwok

NUMBER OF PAGES: vii, 158

ABSTRACT

Tissue heterogeneity effects present a major challenge to electron beam dosimetry in radiotherapy and radiation protection. The perturbation of the absorbed dose distribution in tissue due to the presence of heterogeneous material boundaries was investigated in this work. Experiments were conducted in a tissue-equivalent phantom in order to quantify electron backscatter from various materials. For these experiments, irradiations were performed using a 6MeV (nominal) electron beam under conditions of one-dimensional geometry. Depth-energy degradation of the electron beam provided mean electron energies of 2.3MeV, 1.9MeV, and 1.4MeV at interface locations. Backscatter phenomena were investigated for the following interface geometries: polystyrene/air, polystyrene/cortical-bone-equivalent plastic, polystyrene/copper, and polystyrene/bismuth. Novel radiochromic film dosimetry techniques were developed for these experiments, and the dose and energy response characteristics of GAFChromic Type 37-041 film were investigated. Monte Carlo simulations of the experiments were performed in parallel, using the ITS TIGER code, and methodologies were developed to determine appropriate input parameters to these simulations. From experimental and Monte Carlo results, the backscatter factor at the interface, its spatial variation with depth, and its dependence on electron energy and scatterer atomic number were investigated.

ACKNOWLEDGEMENTS

I wish to thank McMaster University, the Hamilton Regional Cancer Centre, and Dr. Cheuk Kwok for providing the opportunity and the means to undertake this project. In addition, I thank the following individuals, each of whom has contributed to this work: Daniel Ritt (Radiological Imaging Technologies, Inc.), Dr. William Prestwich, Aleks Cenic, Sandi Bosnic, Carrie-Lynn Swift, and John Blenkey. Special thanks also to Joanne for continuing to love and humour me throughout.

TABLE OF CONTENTS

ABSTRACT iii
ACKNOWLEDGEMENTS iv
TABLE OF CONTENTS v
LIST OF TABLES viii
LIST OF FIGURES ix

PART I: INTRODUCTION 1

1. Overview 2
   1.1 Background 3
2. The Interaction of Electrons with Matter 6
   2.1 Electron Interaction Processes 6
   2.2 The Continuous Slowing Down Approximation 9
   2.3 Energy Deposition 12
   2.4 Practical Considerations for Clinical Linear Accelerators 14
      2.4.1 Beam Spectra 14
      2.4.2 Depth-dose 15
3. Monte Carlo Simulation of Electron Transport 21
4. Radiochromic Film Dosimetry 24

PART II: MATERIALS AND METHODS 28

5. The Experiments 29
   5.0 Irradiations and Dosimetry Standards 29
      5.0.1 6MeV Electrons 29
      5.0.2 ^{60}Co Irradiations 31
   5.1 Spectrophotometry 32
   5.2 Radiochromic Film Sensitometry 34
      5.2.1 Nominal 6MeV Electron 35

5.2.2 6MeV Electron Depth Dose in Water 36
5.3 Backscattering Experiments 38
5.3.1 Measurement Phantom 43
6. The Monte Carlo Simulations 46
6.1 Use of the ITS codes 46
6.2 Determination of Electron Beam Energy Spectra from Central-Axis Depth-Dose Distributions 49
6.3 Correction for SSD 52
6.4 Simulations 55
6.4.1 Homogeneous Geometry 55
6.4.2 Heterogeneous Geometry 56

PART III: RESULTS 58
7.1 Electron Beam Energy Spectrum Determination 59
7.1.1 100cm SSD Beam Energy Spectrum Determination from Water Tank Depth-Dose Measurements 59
7.1.2 Beam Energy Spectrum Corrected to 60cm SSD 65
7.2 Monte Carlo Simulation of Homogeneous Conditions 67
7.2.1 Depth-Energy in Water 67
7.2.2 Depth-Dose and Depth-Energy in Polystyrene . 68
7.3 Spectrophotometry 72
7.3.1 Spectral Response of GAFChromic Type 37-041 Radiochromic Film for 6MeV Electrons . . 72
7.3.2 Spectral Response: ^{60}Co Irradiations 80
7.3.3 Batch #2 Results 83
7.4 Sensitometry 86
7.4.1 Nominal Dose Response 86

7.4.2 Determination of the Energy Dependence of GAFChromic Films 95
7.5 Backscatter Experiments 97
7.5.1 Data Analysis 97
7.5.2 Characterization of Backscatter 103
7.5.4 Spatial Distribution of Backscatter B(x): TIGER and Strip Film Results 107
7.5.5 Application of Empirical Backscatter Relationships 123

PART IV: DISCUSSION AND CONCLUSIONS 127
8. Techniques and Results 128
8.1 Determination of Beam Energy Spectra for Monte Carlo Simulations 128
8.2 Radiochromic Film Dosimetry 131
8.2.1 Sensitometry of GAFChromic Type 37-041 Film 131
8.2.2 Experimental Technique: Strip Film Measurements 134
8.3 Heterogeneity Experiments 138
8.3.1 Comparison of Experimental Results and Monte Carlo Simulations 138
8.3.2 Characterization of Backscatter 141
9. Summary and Recommendations for Future Work 146

APPENDIX I PROGRAM LISTING: BEAMSPEC.BAS 148

REFERENCES 154

LIST OF TABLES

Table 5.1: Linear Accelerator Settings for 6MeV Irradiations 30

Table 5.2: Material Properties of Scatterers 41

Table 5.3: Composition of Layer 1 in Backscattering Experiments 42

Table 7.1: Fitting Parameters 61

Table 7.2: Derived Energy Parameters 61

Table 7.3: Mean and most probable energies at d_{max}, R_{20}, and R_5 68

Table 7.4: Relative sensitivity of ^{60}Co to 6MeV electron irradiations . 80

Table 7.5: Backscatter Factor at interface B(0) from spot film measurements and Monte Carlo calculations 106

Table 7.6: Backscatter factors B(0) from single exponential fitting of strip film and Monte Carlo results 120

Table 7.7: Relaxation lengths x_0 from single exponential fitting of strip film and Monte Carlo results 121

Table 7.8: Proportionality Constants for Empirical Backscatter Relationships 124

LIST OF FIGURES

Figure 2.1: Typical electron beam depth-dose distribution in a semi-infinite homogeneous medium 16
Figure 5.1: Spectrophotometer 33
Figure 5.2: Water tank penetration for depth-dose measurement. 37
Figure 5.3: Backscattering experiment geometry 40
Figure 5.4: Measurement Phantom 44
Figure 6.1: TIGER simulation geometry. 57
Figure 7.1: TIGER simulation of depth-dose profiles for monoenergetic electron beams in water: 0.5MeV (left), 1.0MeV, ... , 7.5MeV, 8.0MeV (right). 60
Figure 7.2: Derived beam energy spectra for 21-A and 21-B 6MeV electron beams 62
Figure 7.3: Derived 6MeV electron beam energy spectrum for 21-C (top). Spectrum based on BEAM simulation of treatment head and applicator (below) by Ding *et al.* 63
Figure 7.4: 6MeV electron depth-dose distribution measurements (lines) and TIGER simulations in water for three CLINAC 2100-C linear accelerators (symbols) 64
Figure 7.5: Results of CSDA SSD Correction. Top panel, 100cmSSD spectrum (continuous) used to derive 60cmSSD spectrum (dotted). Bottom panel, 60cmSSD (continuous) spectrum simulated at $\Delta x = 40$cm (dotted). 66

Figure 7.6: Depth-mean energy distribution for 6MeV electrons in water based on TIGER simulation (□), and Harder's approximation (dotted) 67
Figure 7.7: 6MeV electron absorbed dose (+) and mean energy (□) distributions in polystyrene at 60cm SSD based on TIGER simulations 69
Figure 7.8: Depth-dose distribution in polystyrene, TIGER simulation (○) and parallel plate ionization chamber measurements (+) 70
Figure 7.9: TIGER simulated electron energy distribution at several depths in polystyrene (surface, d_{max}, R_{20}, and R_5) *[colour]* 71
Figure 7.10: Absorption spectra for 6MeV electron doses of 263Gy, 132Gy, 79Gy, 52Gy, and 26Gy *[colour]* 75
Figure 7.11: Absorption spectra for 6MeV electron doses of 13Gy, 52Gy, 2.6Gy, 1.3Gy, and 0.5Gy *[colour]* 76
Figure 7.12: Absorption spectra for 6MeV electron doses of 263Gy to 26Gy with logarithmic ordinate (logarithmic plot of Figure 7.10) 77
Figure 7.13: Dose's optical density response of main absorption peak (●) and peak location (○) for 6MeV electron irradiations 78
Figure 7.14: Single wavelength dose response for 6MeV electrons 79
Figure 7.15: Single wavelength dose response for ^{60}Co and 6MeV electron irradiations *[colour]* 82
Figure 7.16: Batch #2 results, 6MeV electrons *[colour]* 84
Figure 7.17: Batch #2 results for ^{60}Co *[colour]* 85
Figure 7.18: 6MeV electron calibration at d_{max} analyzed on the RIT113 scanning densitometer 87

Figure 7.19: Response correction factor 89
Figure 7.20: Optical density profile of a uniformly irradiated film (109Gy) showing uniformity and edge artifact. (□) indicate standard error at each measurement 93
Figure 7.21: Fold artifact; OD profile of unirradiated, folded film 93
Figure 7.22: Radiochromic film (line) and diode detector (□) measured depth-dose in water. Nominal dose at d_{max} is approximately 20Gy 96
Figure 7.23: Energy response function $\zeta(x)$. Dotted lines indicate $\pm 5\%$ 96
Figure 7.24: Homogeneous films at d_{max}, R_{20}, and R_5, showing fold artifact spikes 102
Figure 7.25: Alignment of the homogeneous strip films using the fold artifact. Interface locations are shown as vertical bars (dotted). 102
Figure 7.26: B(x') for bismuth at d_{max}, strip film measurements (+) and TIGER simulation (O). 108
Figure 7.27: B(x') for copper at d_{max}, strip film measurements (+) and TIGER simulation (O). 109
Figure 7.28: B(x') for bone-equivalent plastic at d_{max}, strip film measurements (+) and TIGER simulation (O). 110
Figure 7.29: B(x') for air at d_{max}, strip film measurements (+) and TIGER simulation (O). 111
Figure 7.30: B(x') for bismuth at R_{20}, strip film measurements (+) and TIGER simulation (O). 112
Figure 7.31: B(x') for copper at R_{20}, strip film measurements (+) and TIGER simulation (O). 113
Figure 7.32: B(x') for bone-equivalent plastic at R_{20}, strip film measurements (+) and TIGER simulation (O) 114

Figure 7.33: B(x') for air at R_{20}, strip film measurements (+) and TIGER simulation (O). 115
Figure 7.34: B(x') for bismuth at R_5, strip film measurements (+) and TIGER simulation (O). 116
Figure 7.35: B(x') for copper at R_5, strip film measurements (+) and TIGER simulation (O). 117
Figure 7.36: B(x') for bone-equivalent plastic at R_5, strip film measurements (+) and TIGER simulation (O). 118
Figure 7.37: B(x') for air at R_5, strip film measurements (+) and TIGER simulation (O). 119
Figure 7.38: Empirical backscatter factor relationship (Baily 1980) *[colour]* 125
Figure 7.39: Empirical backscatter relationship (Mladjenovic 1970) *[colour]* 126

PART I: INTRODUCTION

1. Overview

The goal of this project was to characterize the perturbation of absorbed dose in tissue resulting from the presence of heterogenous material boundaries. This was accomplished through experimental work using radiochromic film dosimetry media, and through computer simulation of electron transport using Monte Carlo techniques. The four introductory chapters of this report outline the context in which this work was undertaken, describe the physical basis for electron backscatter phenomena, and discuss the principles of methodologies employed for data collection and analysis.

Experiments were designed to obtain measurement of the depth-dose variation in a tissue-equivalent phantom under various backscatter geometries. In addition, the dose response characteristics of the radiochromic film used for these experiments were investigated. Methods employed in these experiments, and in Monte Carlo simulations performed in parallel, are described in Part II.

Analysis of results (Part III) involved quantification of backscatter at the interface through single point measurements, and analysis of the variation of backscatter with distance from the interface. Results were analyzed to compare observed backscatter phenomena to Monte Carlo predictions, and to

investigate the variation of backscatter with material properties and electron energy. Findings are discussed in Part IV in the context of current knowledge of electron backscattering and the underlying physics which govern these phenomena. Finally, conclusions are drawn and recommendations for future work are made.

1.1 Background

The potential use of electron radiation for radiotherapy was recognized almost immediately after Kerst's development of the first practical source of high-energy electrons, the betatron, in 1941. Electron beam therapy became an established treatment modality within the next decade (Harvey 1952). Clinical radiotherapy applications of electron beams with energies of 6-18MeV currently include the treatment of cancers of the skin, breast and chest wall, upper respiratory and digestive tract, and neck. Higher energy beams (>18MeV) are used in the treatment of cancers of the bladder, lungs, cervix, colon, and rectum (Klevenhagen 1988).

One of the major challenges of electron-beam dosimetry is the problem of tissue heterogeneities (Khan 1990). In clinical radiotherapy applications there exists the possibility of tissue over-dosage near interfaces due to electron backscatter (Klevenhagen 1981). Early investigation of the effects of

heterogeneities on electron beam dose distributions (Laughlin 1965, Almond 1967) revealed that the magnitude of dose perturbation is related to the electron density, effective atomic number, shape and size of the heterogeneity. Subsequent work in this area has used experimental measurement, computer simulation, and application of analytical models to investigate heterogeneity effects for electron beams of various energies and for various β-emitting radioisotope sources.

Eisen *et al.* (Eisen 1972) have measured the electron dose distribution from a 2MeV beam in two layer slab absorbers comprised of polystyrene, copper, tin, and gold. Their work utilized a prototype version of the radiochromic media used in this work, and also included Monte Carlo simulation of experimental conditions. While their work demonstrated the feasibility of this type of study, restrictions in computing power and poor reproducibility in the dye film dosimetry methods available at the time of their investigation restricted the accuracy of the backscatter effects observed. Eisen's work, however, spawned further research and has provided benchmark data for subsequent attempts to illuminate electron backscatter phenomena (Berger 1986).

The effects of scatterer atomic number and thickness and electron energy on backscatter, over the range of 3-35MeV, was investigated by

Klevenhagen *et al.* (Klevenhagen 1981). For high energy beams, the increase in backscatter with atomic number was found to exhibit exponential character, and a decrease in backscatter with increasing electron energy was observed. However, the trends in backscatter behaviour at low energies were less clear, and they have indicated the need for further research in this area.

Electron dosimetry and beta dosimetry bear a high degree of similarity. Recent work by Kwok *et al.* (Kwok 1986, Kwok 1991) and Nunes (Nunes 1992) have investigated backscatter in the context of β-particle dosimetry and radioimmunotherapy. These studies differ from this work in that backscatter was investigated under conditions of lower electron energy and of point-, rather than beam-geometry.

This work was therefore aimed to continue in the vein of Eisen *et al.* with the benefit of improved radiochromic dosimetry and Monte Carlo capabilities. The energy dependence of backscatter at low electron beam energies is specifically addressed to provide data over the range where considerable uncertainty in backscatter behaviour currently exists.

2. The Interaction of Electrons with Matter

Quanta of energy transported by radiation fields, manifested in particles as kinetic energy or in photons as inherent energy, can be given up to matter through which the radiation passes via various interaction processes. The field of radiation dosimetry is concerned with the fate of radiations in their interactions with both living and non-living matter; and ultimately with the quantity and distribution of absorbed energy, or dose, received by these media. A brief summary of some of the general concepts of radiation dosimetry is presented in this chapter, with emphasis on those concepts relevant to the methods employed in this work.

2.1 Electron Interaction Processes

Electrons are produced in nature through the decay of radioisotopes: in the processes of β-emission, Auger electron emission, internal conversion, and photo-electric effect. Artificial means of electron production include linear accelerators, betatrons, and electron synchrotrons (Attix 1986). Each of the electron's physical characteristics, including mass, charge, and spin, contributes to various complex forms of interactions with matter. While rigorous treatment of electron interaction phenomena can be found in the

literature (Attix 1986, Evans 1955), the following will attempt to give a rather simplistic and general picture of electron transport.

As a charged particle, the electron can interact with both atomic nuclei and atomic electrons through collision phenomena and through Columbic interactions. Since atomic nuclei are massive compared to electrons, only a small fraction of the electron's energy is transferred, on average, through electron-nucleus interactions. These interactions, however, can significantly alter the course of the incident electron, leading to large angle scattering and the production of Bremsstrahlung radiation. A travelling electron, as a particle, is identical to an atomic electron. Since the two have equal mass, electron-electron interactions result in much greater energy transfers, up to the energy of the incident electron. Thus after interacting, the knock-on electron and primary electron are indistinguishable. As a consequence of identical-particle scattering, spin complicates theoretical models of electron-electron (Møller) scattering. As a further complication to any consideration of high energy electron interactions, the rest mass energy of an electron (0.511MeV) is usually small in comparison to its kinetic energy. Relativistic effects must therefore be accounted for when considering electrons with energies above a few thousand electron-volts.

A fundamental parameter for characterizing a radiation field is its fluence $\Phi(r,t)$. Fluence rate, a scalar quantity differentiable in energy and angle, is defined as the product of the number density and velocity. It can thus be thought of as the number of quanta of radiation passing through a sphere of unit cross-sectional area per unit time. Interactions are processes which lead to a change of state in two objects when they achieve proximity. If one considers the radiation field to be composed of projectiles, and the atoms in which the radiations interact as targets, the idea of an interaction cross-section can be introduced. The cross-section σ for a particular type of interaction can be conceptualized as the effective area presented by the target atom to the incident radiation. Thus, the probability of interaction dW in time dt (per target) is given by the product of the cross-section and the fluence rate.

$$dW = \sigma \Phi \, dt$$

Electron interactions can be characterized by the relative size of an impact parameter b with respect to the atomic radius a. The impact parameter represents the perpendicular distance between the line of motion of the projectile and target atom. Thus, encounters fall into three general categories: soft collisions, where $b >> a$, are interactions between radiation and the atom as a whole; hard or "knock-on" collisions occur with atomic electrons ($b \sim a$); and close collisions ($b << a$) involve interactions with target nuclei. Interactions

result in scattering and energy losses experienced by the electron and the deposition of energy in the target medium.

Scattering and energy loss events occur at a very high frequency along the electron's torturous path, and energy losses from individual events are usually slight. It is estimated that an electron with initial energy of 0.5MeV, travelling in aluminium, will typically undergo in the order of 10^4 collisions in the course of experiencing energy loss to 1keV (Andreo 1991). The electron can thus be thought of as undergoing a continuous process of slowing down.

2.2 The Continuous Slowing Down Approximation

A simplistic approach to electron transport is the CSDA or continuous slowing down approximation. The key parameter of this model is the stopping power S(E), which is defined as the energy loss dE per unit path length x experienced by an electron with instantaneous energy E:

$$S(E) = -\frac{dE}{dx}$$

Since there are distinctly different mechanisms for radiative and collision interactions, it is possible to separate these two components of the total stopping power.

$$S(E) = S(E)_{rad} + S(E)_{coll}$$

Collisional losses resulting in specific energy loss through ionization and excitation for fast electrons have been characterized by Bethe (Knoll 1988) in the following expression:

$$S(E)_{coll} = \frac{2\pi NZ}{m_0 v^2}\left(\ln\frac{m_0 v^2 E}{2I^2(1-\beta^2)} - (ln2)\left(2\sqrt{1-\beta^2} - 1 + \beta^2\right)\right.$$
$$\left. + (1-\beta^2) + \frac{1}{8}\left(1-\sqrt{1-\beta^2}\right)^2\right)$$

The radiative stopping power which arises from radiative losses in the form of Bremsstrahlung radiation is given by (Knoll 1988):

$$S(E)_{rad} = \frac{NEZ(Z+1)e^4}{137(m_0c^2)^2}\left(4\ln\frac{2E}{m_0c^2} - \frac{4}{3}\right)$$

In the above expressions, N and Z are the number density and atomic number of the target atoms, v is the electron velocity, m_0 is the electron rest mass, e is the electron charge, β is defined as v/c, and I represents the average ionization and excitation potential of the absorber.

The following general properties of these expressions should be noted. The radiative stopping power is approximately proportional to E and Z^2 and as

such, radiative losses are more significant for high electron energies and high atomic number targets. The ratio of radiative to collision stopping powers shows that radiative losses are typically only a small fraction of collisional energy losses and are significant only in high Z materials. Empirically, this ratio is given by (Knoll 1988):

$$\frac{S(E)_{rad}}{S(E)_{coll}} \approx \frac{EZ}{700}$$

where E is in units of MeV.

The CSDA range R_0 is defined as the total distance over which an electron completely loses its initial energy E_0. Thus,

$$R_0 = \int_0^{E_0} \frac{dE}{S(E)}$$

As a consequence of the CSDA, fluence is inherently assumed to be constant over the region $0<x<R_0$ and equal to zero for $x>R_0$. In reality, the random nature of interactions will result in a distribution of individual ranges for electrons. Therefore, the true range of a beam of monoenergetic electrons will not bear a well-defined end-point. The statistical nature of energy deposition and range are referred to as energy loss straggling and range straggling. In

neglecting the effects of straggling, the CSDA model breaks down in describing energy loss for low energy (keV) electrons and for high energy electrons nearing the end of their range.

2.3 Energy Deposition

Primary modes by which energy is lost by the radiation field through interactions with target media are ionization, excitation, and Bremsstrahlung emission. Excitation occurs when relatively small amounts of energy (in the order of a few eV) are transferred from the incident radiation to an atom, promoting a bound electron to a higher energy state. Upon returning to its ground state, the atom gives off this energy through photon or electron emission. In ionization, an atom receives sufficient energy from the radiation field to eject an orbital electron, thus forming an ion-pair. The average energy required to form an ion pair in air is roughly 33.7eV (Knoll 1988). If the ejected electron is from an inner (K or L) shell, then a vacancy is left. To form a lower energy state, an electron from a higher orbital will fall to fill this vacancy, giving up the excess energy as a photon with characteristic energy corresponding to the difference in orbital energies. Both the emitted photons and ejected electrons contribute to the radiation field since they become energy carriers and can cause subsequent ionization and excitation. Bremsstrahlung radiation is created when a high-energy charged particle experiences a close interaction

with an atomic nucleus, resulting in a substantial change of direction and loss of energy. The energy lost by the charged particle is emitted in the form of X-radiation. Since the initial orientation of the incident particle and target nucleus is essentially random, Bremsstrahlung radiation appears as a continuous spectrum with maximum energy equal to that of the maximum energy of the incident charged particles.

Absorbed dose D(r) is defined as the energy per unit mass received by the material from the radiation field, while kerma G(r) is the energy given up by the radiation field per unit mass of the medium. These quantities are not necessarily equal since energy given up by the radiation field can be transported by secondary radiations further into the medium before it is absorbed. For the case of electrons, absorbed dose is related to energy and fluence according to the following relationship (ICRU 35):

$$D(x) = -\int_0^{E_0} \Phi_{E,x}(x)\,\frac{dE}{dx} + E\frac{d\Phi_{E,x}(x)}{dx}\,dE$$

In the above expression, the first term of the integrand represents the energy deposited by the radiation field in the course of travel along a distance dx, while the second is the energy deposited by electron coming to rest in dx.

2.4 Practical Considerations for Clinical Linear Accelerators

2.4.1 Beam Spectra

Electron beams produced by clinical linear accelerators must traverse several layers of various materials before reaching the patient surface or phantom. These materials include the accelerator exit window, scattering foils, monitor chambers, and air. While the electron energy distribution on the inner side of the accelerator exit window is nearly monoenergetic, energy losses resulting from interactions in the intervening materials both shift and broaden the energy spectrum at the surface. Thus, the energy spectrum at the surface $\Phi_0(E)$ consists of a peak which drops abruptly at higher energies and tails off gradually towards lower energies. The two parameters most commonly used to characterize the energy spectrum are the mean energy $<E_0>$ and "most probable energy" $E_{p,0}$.

Techniques used to directly measure the energy spectrum of an electron beam include magnetic spectrometry and luminescent crystal spectrometry (ICRU 35), while single parameters can be characterized through range measurements or threshold reaction methods (Khan 1984). Range parameters from depth-dose measurements in water are suitable for routine quality assurance in a clinical setting. Previously, investigators have reported

successful reconstruction of electron beam energy spectra from depth-dose distributions. Kovář *et al.* applied a non-linear least-squares Gauss-Newton iteration method (Kovář 1983) to reconstruct 4MeV and 8MeV beam energy spectra, while Altschuler *et al.* (Altschuler 1992) applied a similar composite kernel methodology for a 9MeV beam. We have applied a similar methodology in which energy deposition kernels for monoenergetic electron beams in water were generated through Monte Carlo simulation. The energy fluence spectrum at the surface was then determined through an iterative process, where weights were assigned to these kernels and subsequently optimized through variance reduction, to recover the measured depth-dose profile. This derived energy spectrum was subsequently used in Monte Carlo simulation of experiments.

2.4.2 Depth-dose

The depth-dose distribution of an electron beam in a semi-infinite homogeneous medium (Figure 2.1) is characterized by four regions: dose build-up, dose maximum, dose fall-off, and Bremsstrahlung contamination. Dose build-up occurs due to increased inclination of primary electron tracks, through build-up of secondary electrons, and (to a lesser extent) secondary and Bremsstrahlung photons. Both total electron fluence and absorbed dose reach maxima simultaneously and fall off rapidly with depth past d_{max}. The central

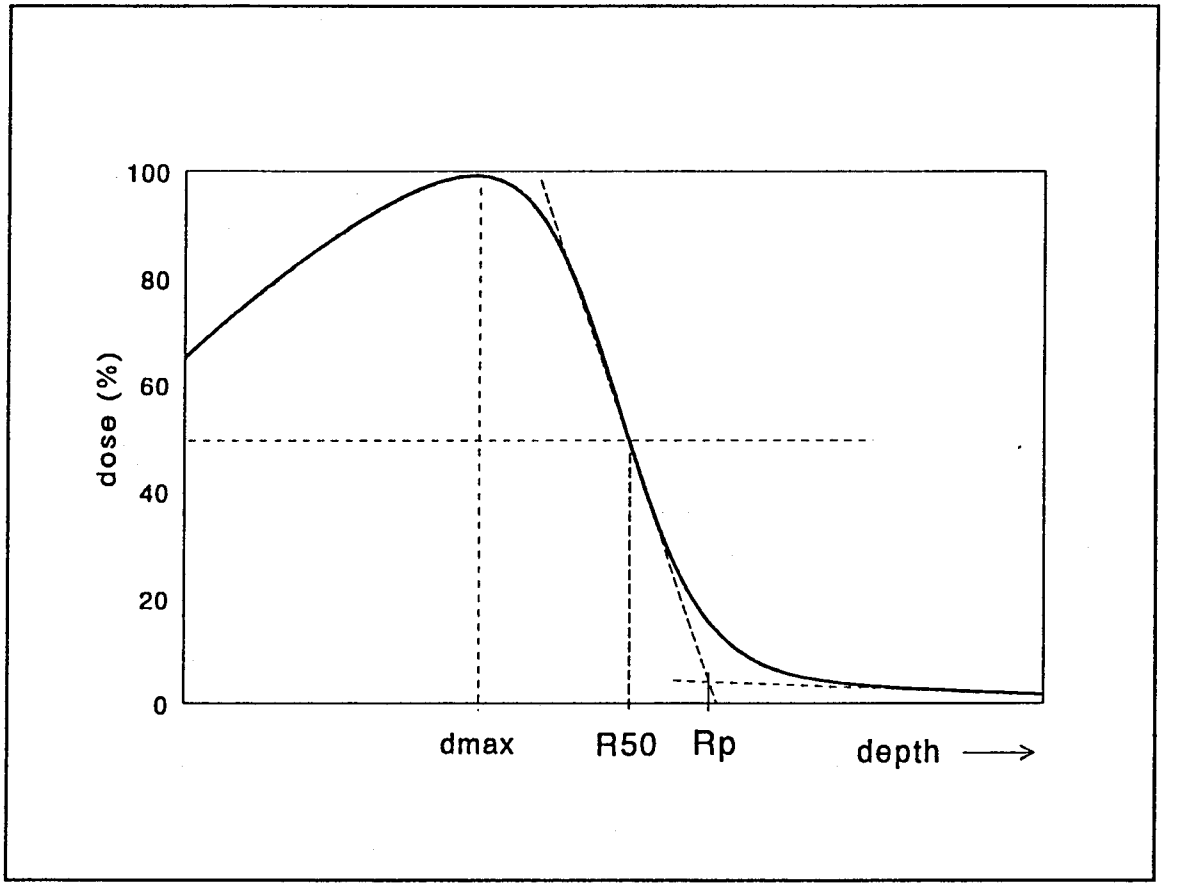

Figure 2.1: Typical electron beam depth-dose distribution in a semi-infinite homogeneous medium

portion of the dose fall-off is essentially linear. Due to range straggling, the fall-off region flattens asymptotically as it approaches zero dose. The final region of non-zero dose is due to contamination from Bremsstrahlung radiation produced both within the treatment head and within the medium. Since the mean free path of a photon of a given energy greatly exceeds that of an electron with the same energy, the Bremsstrahlung tail is relatively flat and extends deeply into the medium. Range parameters typically used to characterize depth-dose curves are as follows: d_{max} is the depth corresponding to D_{max}, R_{50} is the depth corresponding to $0.5D_{max}$, and R_p is the most probable range. R_p is determined by extrapolating the tangent to the depth-dose curve at R_{50} to the depth where it intersects the extrapolated Bremsstrahlung contamination.

2.5 Boundary Electron Transport

An electron incident from one side of an interface may undergo sufficient deflection from its course such that it reemerges from the surface through which it entered. This is the phenomenon of backscattering. A dose enhancement ratio DER is defined as the ratio of the dose received in the presence of a heterogenous scatterer to that of the homogeneous case. The backscatter factor B is defined as:

$$B = DER - 1$$

The interactions leading to significant angular scattering of electrons are electron-electron (hard) and electron-nucleus (close) scattering. In the non-relativistic limit of identical particle elastic (Rutherford) scattering, the maximum deflection in the lab system experienced by either particle is $\pi/2$ (Attix, 1986). Single events thus lead only to forward-directed scattering, and backscattering is possible only through multiple scattering events. However, if one considers the baseline (non-relativistic) case of Rutherford scattering between electrons and nuclei, single events can lead to very large angular deflections such that scattering angles from 0 to π are possible. Therefore, the primary mechanism for backscatter is through elastic electron-nucleus interactions, while multiple electron-electron interactions contribute to a lesser extent.

The differential cross section for Rutherford scattering in the non-relativistic limit of electron-nuclear interaction is given by (Rutherford 1911):

$$\frac{d\sigma}{d\Omega} = \frac{Z^2 e^4}{4\,(mv^2)^2} \frac{1}{\sin^4 \frac{\theta}{2}}$$

where Ω is the solid angle, θ is the scattering angle, Z is the atomic number of the target atom, and e and mv are the electron charge and momentum. The

above expression predicts that backscatter would be more pronounced for scatterers with high atomic number and for electrons with low incident energy. Experimental results are consistent with this prediction (Knoll 1988). In addition, the Rutherford cross-section is approximately proportional to Z^2, while the collision stopping power varies as Z. As a result, the energy of backscattered electrons from a high-Z scatterer will be greater, on average, than that in the homogeneous situation.

The inherent complexity of models of individual electron interactions renders derivation of analytical descriptions of the bulk phenomenon of backscatter inextricable. However, the following empirical descriptions relating the backscatter factor B, immediately upstream of an interface, to atomic number Z and atomic mass M of the scatterer have been proposed:

$$B \propto \sqrt{\frac{Z(Z+1)}{M}}$$

(Mladjenovic 1970)

$$B \propto \log(Z+1)$$

(Baily 1980)

Backscatter is a spatially varying quantity of the form B(x) for the one-dimensional case where x is the distance from the interface. While the above attempts to characterize backscatter amplitude at the interface B(0), work by Nunes (Nunes 1991) has characterized B(x) with single and double exponential models. These relationships for the backscatter factor and its spatial variation have been explored in this work.

3. Monte Carlo Simulation of Electron Transport

In the context of radiation transport, Monte Carlo methods simulate the trajectories, or *histories*, of individual radiation quanta in their interactions with matter. This is achieved through random number sampling from known probability distributions relevant to, and governing, the individual interactions. By simulating a suitably large number of histories in this fashion information regarding bulk properties, such as energy deposition, can be scored by averaging over many histories. While analytical solutions to relatively simple radiation transport problems have proven intractable due to the inherent complexity of electron and photon interactions, Monte Carlo techniques have proven invaluable in the modelling of radiation transport problems. Various applications for these techniques have been found in medical and health physics, specifically in radiation dosimetry and radiotherapy physics (Andreo 1991). In this chapter, some of the general underlying principles of Monte Carlo simulation are introduced, and the specific properties of the Integrated Tiger Series of Codes (Halbeib 1992) employed in this work are discussed.

Pioneering work in Monte Carlo simulation as applied to radiation physics focused primarily on photon and neutron transport in the context of nuclear reactions. These early methods simulated interactions on an individual basis.

The fundamental differences in electron interaction processes, however, render this approach unfeasibly time-consuming in application to electron transport. The two major problems encountered are the large number of interactions comprising an electron history and the numerous cascades of secondary radiations produced. Condensed history techniques (Berger 1963) consider the electron path as a series of steps in which effects of large numbers of interactions are grouped together. Multiple scatter theories are drawn upon to account for the net effects of many deflections caused by elastic scatter. Similarly, the composite effect of many small energy losses are derived from energy loss models such as the CSDA or those based upon the Landau distribution (Landau 1944). Condensed history techniques thus combine conventional Monte Carlo techniques with theory in the simulation of combinations of individual sequences of events.

The Monte Carlo electron transport codes which have evolved fall into two general classes based on their treatment of the generation of secondary radiations (Berger 1963). Class I (ETRAN-based) algorithms group the effects from all interactions of a certain type together in each step. As a result, the energy lost by the primary electron is determined without correlation to the generation of secondary radiations. In Class II procedures a distinction is made between energy loss that leads to production of secondary radiations (above a threshold energy) and other types. This correlation of energy loss and

secondary radiation has implications in the treatment of energy loss straggling. The Integrated TIGER Series of Codes (ITS) employed in this work follow a Class I algorithm. As such, energy loss distributions are sampled explicitly to determine fluctuations in energy loss.

Any Monte Carlo radiation transport simulation code is composed of four basic elements: the cross-section data, the particle transport algorithm, geometry specification, and a module for scoring, collection, and analysis of the information generated in the course of the simulation. The first two components deal with the underlying physics of the radiation transport problem in terms of the probability distributions for events and the simulation of their manifestations. The latter components offer the Monte Carlo user flexibility as to the specification of a particular problem and in the format of the final output of the simulation. The ITS package includes three codes based on different geometries: TIGER is a one-dimensional (laterally-infinite slab geometry) code, CYLTRAN uses cylindrical symmetry, and ACCEPT offers specification of three-dimensional geometries. The codes provide output in terms of energy deposition and charge deposition in user-specified zones, and also allow for the scoring of fluence in terms of energy and direction within user-defined ranges. Details regarding problem specification and the use of these codes in this work are described in Chapter 6.

4. Radiochromic Film Dosimetry

Radiochromic dosimetry media are chemical radiation sensors which experience a measurable colour change upon exposure to ionizing radiation. This colour change comes about through the polymerization of dye precursors (leuco dyes) within a solid or liquid solution, without the need for post-processing. Radiochromic media in the form of films and liquid solutions have been applied to measurement of absorbed dose for photon and electron irradiation over the 10^{-2}Gy to 10^{6}Gy range (McLaughlin 1985). Commercially available thin radiochromic films, with a useful range of 10^{3}Gy to 10^{6}Gy, are used routinely in high-dose industrial irradiation applications including sterilization of food and medical devices (McLaughlin 1991). Recently, a more sensitive type of thin radiochromic film has been developed (GAFChromic Type 37-041, ISP Technologies Inc.) which offers a 10^{3} increase in sensitivity and is therefore suitable for measurements in the Gray to kiloGray range. There has been considerable interest in this new film within the medical physics community since it offers the potential for measurement of absorbed dose approaching a suitable range for radiotherapy applications. The radio-chemical properties of radiochromic film can offer distinct advantages over many routinely used dosimeters, including thermo-luminescent dosimeters (TLDs) and ionization chambers.

GAFChromic dosimetry films are comprised of a thin ($\sim 7\mu m$) micro-crystal monomer imaging layer which is coated onto a highly uniform, transparent, polyester base ($\sim 100\mu m$ thick). Since radiochromic film is both thin and composed of elements of low atomic number, it is an excellent dosimeter for measurement in tissue phantoms. The film is transparent, grainless, and experiences a colour change upon exposure to ionizing radiation, turning from light to deep blue. The dye-polymerization process responsible for this colour change involves the breaking of $\equiv$C-CN bonds within the leuco dye molecules (McLaughlin 1977). Energy deposited by the radiation field (i.e. absorbed dose) and transferred to the receptive part of the dye precursor molecule initiates this polymerization process. This energy must be deposited in a single event with energy exceeding the bond strength ($\sim 4eV$). A single energy deposition event is thus amplified through the creation of many dye molecules. The density of dye molecules formed, and therefore the degree of colourization, is directly dependant upon the absorbed dose received. No processing is required to bring about the colour change, which begins immediately upon exposure and fully stabilizes within 5 to 24 hours post-irradiation.

The film's dose response is manifest as an increase in absorbance over the entire visible spectrum. The absorption spectrum of an irradiated film contains a major absorption peak centred at 660-670nm and a secondary peak

centred at 590-610nm. Techniques used to recover absorbed dose from absorbance include densitometry, spectrophotometry, colour photometry, and scanning densitometry. The sensitometry of low sensitivity radiochromic film (GAFChromic Type 37-040) has been studied by McLaughlin *et al.* (McLaughlin 1990). They showed that the film is robust with respect to normal environmental conditions including temperature, humidity, and ambient light, and that very high resolution measurements (>1200 lines/mm spatial resolving power) can be achieved through scanning densitometry. The same dose response in terms of change in absorbance per unit dose was observed for 10MeV electrons and ^{60}Co photons. Chiu-Tsao et al. (Chiu-Tsao 1994) observed a significant variation in response for the high-sensitivity (GAFChromic Type 37-041) film with photon energy (for ^{125}I, ^{137}Cs, and ^{60}Co sources). Radiochromic film has been shown to exhibit a considerably smaller energy dependence on low energy photon radiation than lithium-fluoride TLDs and silver-halide film (Meuench 1991).

In this work, high-sensitivity (GAFChromic Type 37-041) radiochromic film was used in a novel method for the measurement of depth-dose profiles through the incorporation of the film within a tissue-equivalent phantom. The physical characteristics of this dosimetry medium allow for measurement of the dose distribution with minimal perturbation of the radiation field. Since this work involved the measurement of dose within a spatially and energetically

varying radiation field, it was essential to characterize the energy response of radiochromic film to electron energies of 6MeV and below. Spectrophotometry methods were employed to characterize the film's dose response for various types of radiation, and scanning densitometry was used to measure spatially varying dose distributions obtained through phantom measurements.

PART II: MATERIALS AND METHODS

5. The Experiments

The main objective of the experiments was to obtain measurement of electron depth-dose distributions in a tissue equivalent phantom under various backscattering geometries. In order to accomplish this goal, it was first necessary to characterize the dose response of the radiochromic film to electrons of different energies. This chapter describes the preliminary spectrophotometry and sensitometry experiments performed, and the methodology applied in the backscatter experiments.

5.0 Irradiations and Dosimetry Standards

5.0.1 6MeV Electrons

All 6MeV electron irradiations were performed at the Hamilton Regional Cancer Centre using a Varian[1] CLINAC 2100-C linear accelerator (coded as '21-A'). Since the optimum range of sensitivity for the radiochromic film was found to be much higher than typical therapeutic doses, high dose irradiations were carried out under the following high dose rate conditions. A HDTSE (high

[1]Varian, Inc., Palo Alto, U.S.A.

dose total skin electron) applicator permitted the use of a high dose rate while maintaining a large enough field size at the surface to ensure semi-infinite lateral geometry. Dose rate was further increased by shifting from a 100cm SSD (source to surface distance) to a 60cm SSD. These configurations are summarized in Table 5.1 and shall be referred to as *standard* and *high dose* throughout the remainder of this report.

Table 5.1: Linear Accelerator Settings for 6MeV Irradiations

	Configuration	
	Standard	High Dose
Radiation	6MeV (nominal) electrons	
SSD	100 cm	60 cm
Applicator	10x10 standard	HDTSE
Field Size (cm x cm)	10 x 10 @ 100cmSSD	15 x 15 @ 60cmSSD (25 x 25 @ 100cm SSD)
Nominal Dose Rate (at d_{max} in polystyrene)	2.4Gy/min	88Gy/min

Nominal dose measurements for the experiments were made by calibrating the LINAC's internal beam current monitor to a highly accurate external ionization chamber (Capintec[2] PR-06). The output of the beam current monitor is adjusted to give 1MU (monitor unit) approximately equal to

[2]Capintec, Inc., New Jersey, U.S.A.

1cGy in water under the *standard* configuration. This dose conversion factor, nominally equal to 0.97MU/cGy (Wyman 1994), was corrected for temperature and pressure according to the TG21 protocol (Schultz 1983), and used directly to determine dose for all irradiations in the *standard* configuration. The external ionization chamber was used to measure exposure per monitor unit (R/MU) under both configurations. The ratio of exposure at 60cm SSD to that at 100cm SSD was found to be 3.30 ± 0.01, and dose under *high dose* configuration was determined by multiplying the corrected *standard* dose conversion factor by this ratio.

5.0.2 ^{60}Co Irradiations

Irradiation of radiochromic film was also performed using a ^{60}Co radiotherapy treatment unit (Theratron-80[3]) at the Hamilton Regional Cancer Centre. Films were placed within a polystyrene slab phantom, stacked along the beam central axis, at a standard calibration depth of 4.33cm and irradiated at 80cm SSD. The nominal dose rate under these conditions was 0.815Gy/min. The dose rate was measured at the time of each experiment using the same ionization chamber as above, and applying temperature and pressure corrections according to the TG21 protocol. Dose for each film was then determined as the product of dose rate and irradiation time.

---

[3]Theratronics International, Inc., Kanata, Canada.

5.1 Spectrophotometry

The spectral dose response of GAFChromic film was explored using a specially designed spectrophotometry system at McMaster University (Figure 5.1). A halogen light source coupled through a monochromater provided spectral selection for illumination of uniformly irradiated spot films. Transmitted intensity was measured with a diode detector coupled to a personal computer via a voltage to frequency convertor. A film holder designed for spot film measurements (Cenic 1994) provided an effective beam size of 1cmx1cm. Transmission measurements for spot films were made over the range of 560nm to 700nm with a 2nm step size. Net optical density OD of a measurement film was determined from the measured intensity as follows:

$$OD(\lambda) = \log\left(\frac{I_0(\lambda)}{I(\lambda)}\right)$$

where $I(\lambda)$ and $I_0(\lambda)$ were the transmission intensities of the measurement film and a reference film, respectively. The reference film consisted of an unirradiated film which was otherwise treated identically to irradiated films both prior to and after irradiation.

Irradiations were performed using 6MeV electrons (*high dose* configuration) and ^{60}Co for two batches of GAFChromic Type 37-041 film.

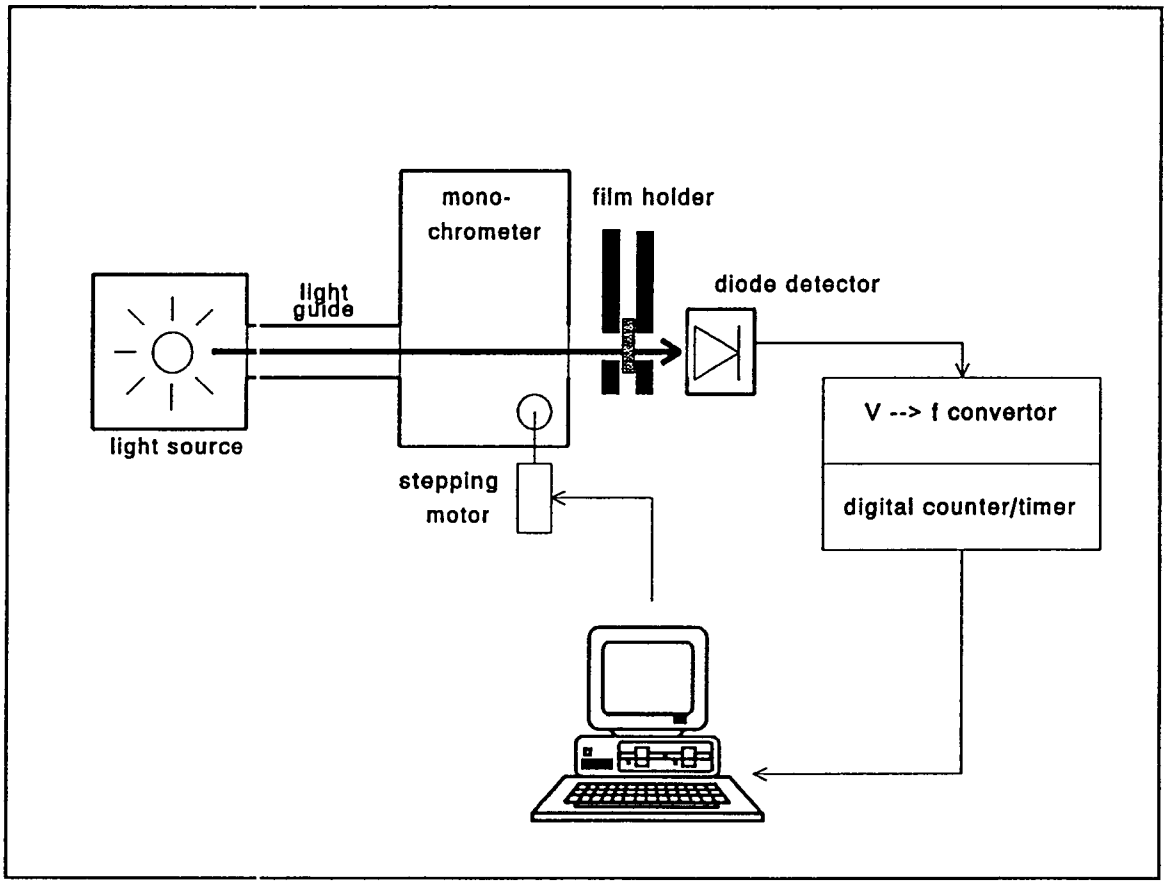

Figure 5.1: Spectrophotometer

"Batch#1" refers to films from a sample pack (provided by Nuclear Associates, Inc.) and Batch#2 films were from Lot#920813 (all subsequent experiments were carried out with film from the latter batch). 1.5cmx1.2cm spot films from both batches were separately irradiated with 6MeV electrons (*high dose*) or ^{60}Co photons at the appropriate d_{max} in a thick multiple-slab polystyrene phantom. For each irradiation, replicate data was obtained by stacking three films central to the beam axis.

5.2 Radiochromic Film Sensitometry

Spatially varying optical density profiles were measured using scanning densitometry techniques for films irradiated with 6MeV electrons. Films were analyzed using a RIT113 high performance film dosimetry system (Radiological Imaging Technologies Inc., Colorado). The film reading service was provided by Radiological Imaging Technologies as part of a collaborative effort. Both this system and this service were offered commercially at the time of the writing of this work. The system consisted of a Lumiscan 100 film digitizer (Lumysis, Sunnyvale California) and purpose-designed image processing software running on a personal computer. The digitizer used a HeNe (632.8nm) laser source, with an illumination spot size of 100μm diameter, and a photo-multiplier tube detector. Films were scanned to 100μm resolution in 2 perpendicular directions (x and y). The digitizer was capable of scanning a total area of 28cmx43cm,

permitting nearly simultaneous measurement of multiple films. An unirradiated background film was included in each scan for net optical density reference measurements.

The digitizer was configured to output intensity to 12-bit resolution, and transformed on a logarithmic scale. High resolution measurement of optical density was thus provided over a large range of intensity (~3.5 decades). The value assigned to each pixel translated to a 12-bit word corresponding to increments of 10^{-3} in optical density. For example, a pixel value PV of 2000 represented an optical density of 2.000. Net optical density at a particular location $OD_{x,y}$ was obtained through subtraction of the pixel value at that location $PV_{x,y}$ from the nominal pixel value of the reference film PV_0:

$$OD_{x,y} = [\, PV_{x,y} - PV_0 \,] \times 10^{-3}$$

5.2.1 Nominal 6MeV Electron Dose Response

Spot films irradiated with 6MeV electrons (*high dose* configuration, at d_{max}) were analyzed on the RIT113 scanning densitometer in order (i) to determine the range of sensitivity for the film dosimetry system, (ii) to obtain a calibration factor from optical density to dose, and (iii) to estimate the inter- and intra- film variation in dose response and hence the precision of the

dosimetry system employed. From these data, the nominal 6MeV calibration function $C_0(OD,D_0)$ was determined as a function of measured net optical density OD and the dose D_0 received at d_{max}.

$$C_0(OD, D) = \frac{D_0}{OD}$$

5.2.2 6MeV Electron Depth Dose in Water

The depth-dose distribution in water over the entire 6MeV electron range was recorded on a strip of radiochromic film as follows. The film was held vertically in a water tank by a special device consisting of paired polystyrene frames, thin polyethylene sheets, and polystyrene support arms (Figure 5.2). The frames sandwiched the radiochromic film by means of the polyethylene sheets, and this apparatus was subsequently compressed and evacuated to remove enclosed air. To ensure semi-infinite geometry, both the enclosed height of the frame and the lateral distance from the inside edges of the frame to the film exceeded the electron range. Since the film and the polyethylene sheets were approximately water-equivalent, the dose recorded by the film was therefore assumed to correspond to the true dose in water. The film and tank were positioned using the LINAC's laser alignment system such that the film's upper edge and water surface both fell at 100cm SSD, and such that the film

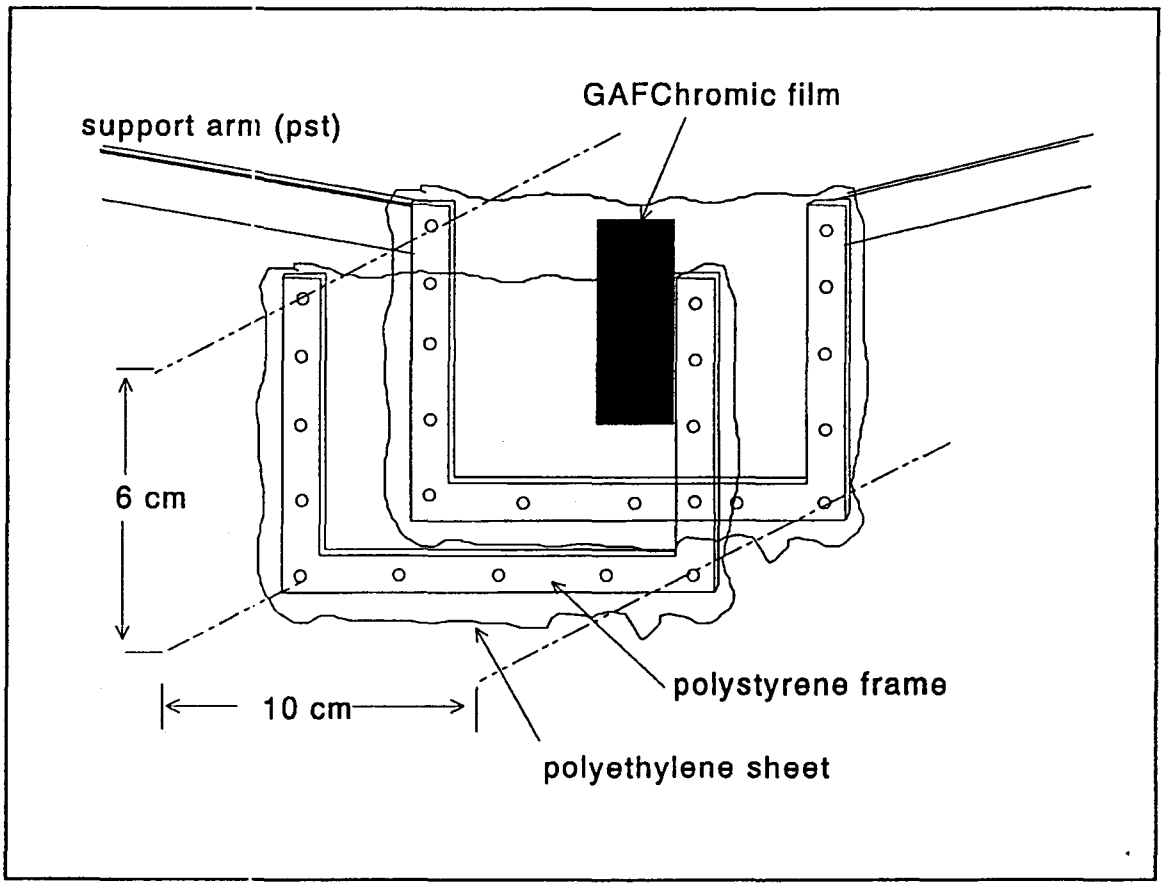

Figure 5.2: Water tank penetration for depth-dose measurement.

lay along the beam central axis. The film was irradiated under the *standard* configuration, at a nominal dose of 20Gy at d_{max}.

The depth-dose distribution D(x) of 6MeV electrons in water measured with an electronic diode detector (Scanditronix RFA 300) was used as the standard in comparison to the dose distribution $D_0(x)$ derived from the film measurements. A relative dose sensitivity factor $\zeta(x)$ with respect to the 6MeV nominal dose response was calculated as a function of depth:

$$\zeta(x) = \frac{D_0(x)}{D(x)}$$

where $D_0(x)$ is the dose predicted by the nominal calibration function as described in section 5.2.1. By applying the distribution of electron beam energy with depth derived from Monte Carlo simulation, the relative energy sensitivity $\zeta(E)$ could then be unfolded from $\zeta(x)$ as function of energy parameters, rather than depth.

5.3 Backscattering Experiments

The goal of the backscattering experiments was to provide high spatial resolution measurement of the absorbed dose along the central axis of a 6MeV electron beam in a two-layer, laterally semi-infinite, heterogeneous medium.

The basic experimental geometry is shown in Figure 5.3. The first layer consisted of a polystyrene measurement phantom and several polystyrene sheets of variable thicknesses. Heterogeneous media were created by introducing a second-layer of different scattering materials. Depth-dose measurements along the central axis were made using strips of radiochromic film placed within the measurement phantom. This phantom was then aligned perpendicularly to the beam of the LINAC with slabs of various scattering materials aligned distally. The following two-layer slab absorbers were thus created:

- Polystyrene/Polystyrene
- Polystyrene/Air
- Polystyrene/Cortical Bone Equivalent Plastic
- Polystyrene/Copper
- Polystyrene/Bismuth

The most clinically relevant interfaces are those involving tissue, bone, and air. Thus, bone equivalent plastic and air were employed as backscattering materials. In Chapter 2 it was explained that dose enhancement due to backscatter increases with the atomic number of the scattering material. Therefore, in order to verify the accuracy of Monte Carlo predictions with greater precision, experiments were also conducted with Copper and Bismuth. Table 5.2 summarizes the properties of the materials used in the backscatter

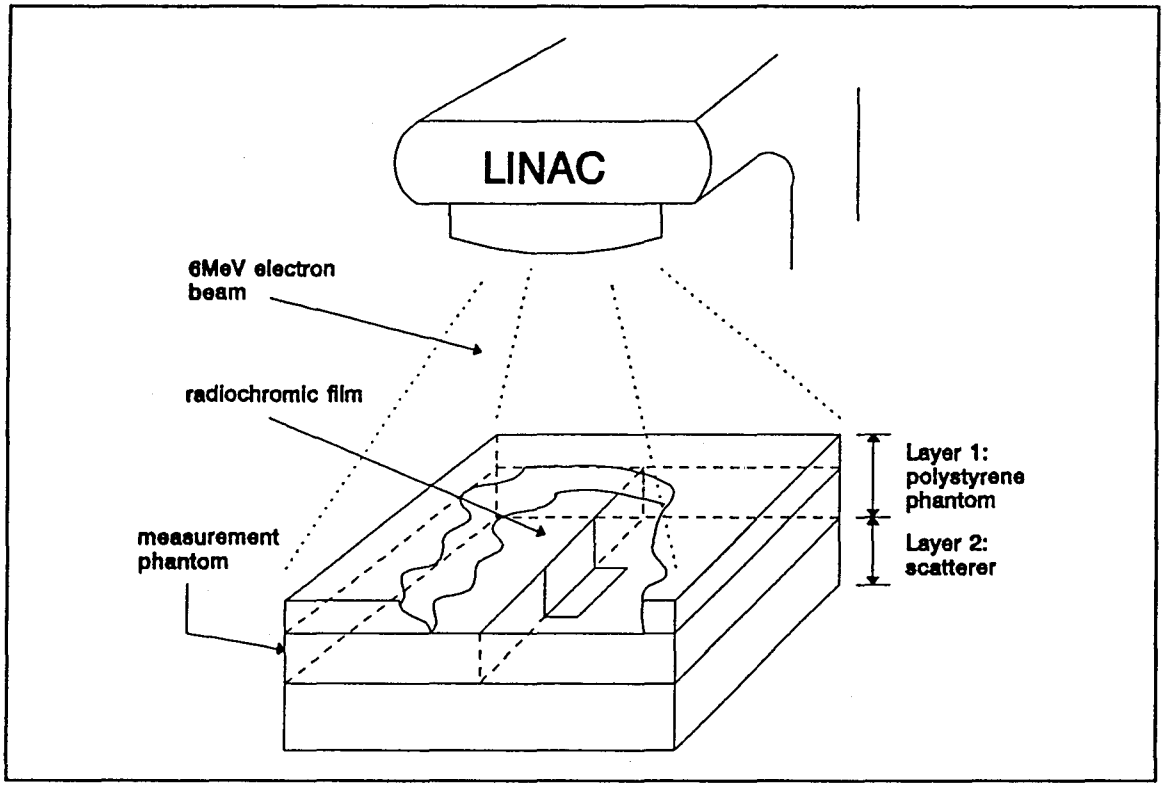

Figure 5.3: Backscattering experiment geometry

experiments.

Table 5.2: Material Properties of Scatterers

Material	Composition in Weight Fraction	Z_{eff}†	Density (g/cm^3)	Dimensions in cm
Water	H: 0.111 O: 0.889	6.60	1.000	-
Polystyrene	C: 0.923 H: 0.077	5.29	1.045 ‡	30 x 30 x 10
ICRP Muscle		6.65	1.136	-
Air	N: 0.754 O: 0.223 Ar: 0.013	7.36	1.21×10^{-3} (@STP)	N/A
Cortical Bone Equivalent Plastic	C: 0.284 Ca: 0.267 O: 0.403 H: 0.025 N: 0.009 Cl: 0.005 S: 0.004 Mg: 0.003	10.3	1.90	7.62 x 7.62 x 1.60
Copper	Cu: 1.000	29	8.93	5.08 x 5.08 x 0.3
Bismuth	Bi: 1.000	83	9.8	6.2(radius) x 0.6

‡measured (V.Peters 1994)

†The effective atomic number Z_{eff} listed in Table 5.3 is given by (Cross 1968):

$$Z_{eff} = \frac{\sum_{i=1}^{n} w_i \frac{Z_i^2}{M_i}}{\sum_{i=1}^{n} w_i \frac{Z_i}{M_i}}$$

where w_i, Z_i, M_i are the weight fraction, atomic number, and atomic mass of i^{th} constituent element of the material.

Additional polystyrene sheets were inserted in layer 1, above the measurement phantom, in order to provide depths corresponding to approximately 100%, 20%, and 5% of the maximum dose (d_{max}, R_{20}, and R_5, respectively) for the heterogeneous interface. A parallel plate ionization chamber (Capintec[4] PS-033) was used to determine these depths. Table 5.3 lists the arrangement of the measurement phantom and polystyrene sheets used to position the interface at the desired locations.

Table 5.3: Composition of Layer 1 in Backscattering Experiments

Nominal Depth	Layer 1 Thickness (cm)	Thicknesses (cm)		
		Measurement Phantom	Total Additional Sheets	Individual Sheets
d_{max}	1.330	1.330	-	-
R_{20}	2.593	1.330	1.263	0.660 0.226 0.225 0.077 0.075
R_5	2.935	1.330	1.605	1.380 0.225

Two film orientations were used in the backscatter experiments. Strip films held within the phantom recorded the spatially-varying dose distribution along the beam central axis. Additional spot films were placed horizontally in

[4]Capintec, Inc., New Jersey, U.S.A.

the interstices between layers 1 and 2 in order to confirm the backscatter dose at the interface. Analysis of spot films was used to determine the backscattering amplitude at the interface, while the strip films recorded the spatial distribution of backscatter upstream of the interface.

5.3.1 Measurement Phantom

Figure 5.4 shows the polystyrene measurement phantom used in the backscattering experiments. It consisted of a bisected polystyrene slab which held a strip of radiochromic film at an angle of 10° to the beam central axis. For commonly used silver halide dosimetry films (e.g. Kodak XV-2, Kodak XTL, and Kodak Industrex M) it has been shown that perpendicular and parallel arrangement of film give the same result under correct conditions (Dutreix 1969). In the parallel configuration, however, streaming of electrons through thin air gaps, introduced by the presence of film along the beam central axis, can perturb the radiation field over the initial 20%-30% of the electron range (Dutriex 1969). Compensation for the effects of streaming was achieved through the introduction of a small (10°) obliquity in the position of the film along the beam central axis. Spatial measurements along the film were corrected by a factor of cos(10°) to correspond to depth along the central axis.

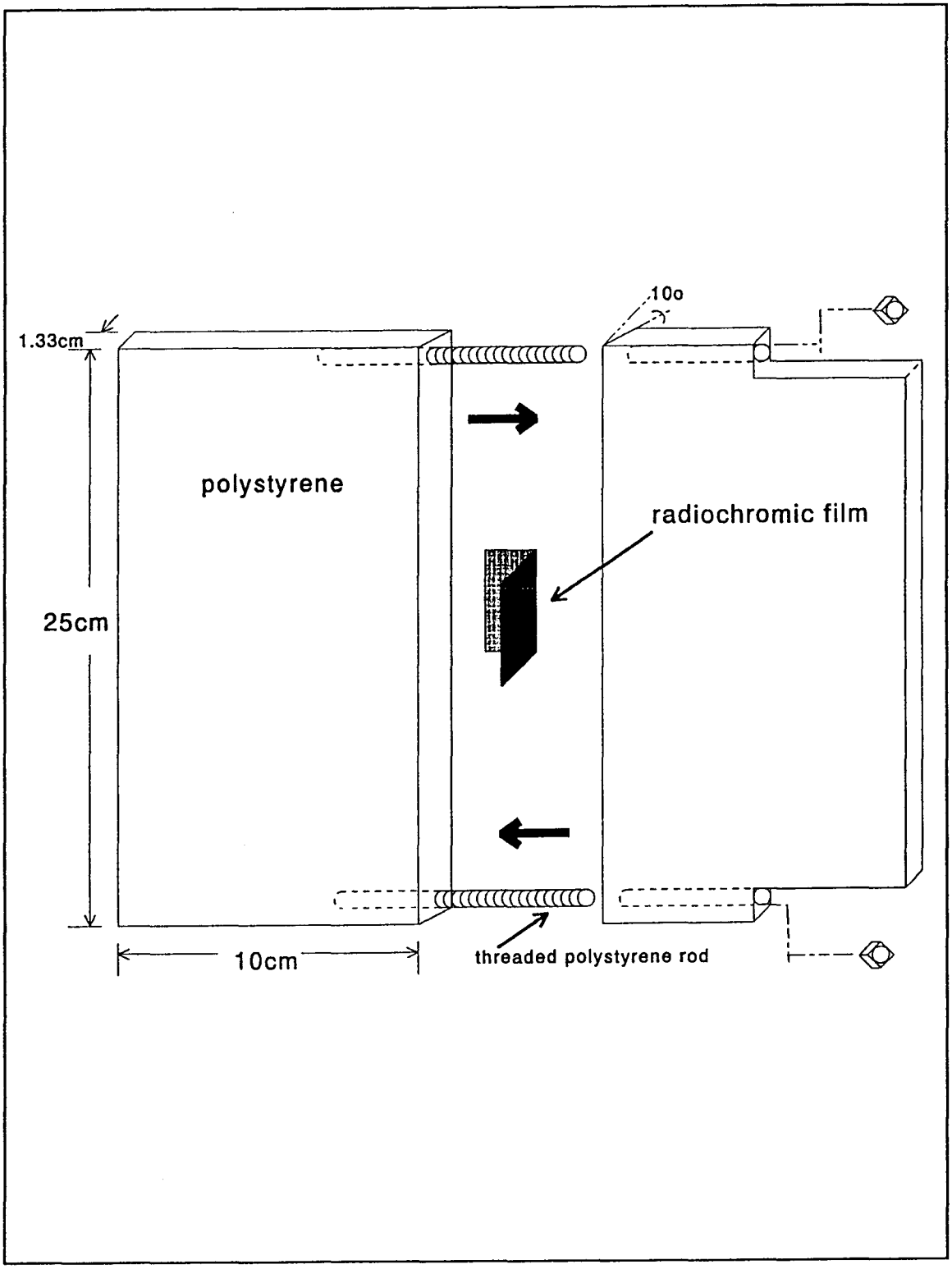

Figure 5.4: Measurement Phantom

Polystyrene is a suitable solid substitute phantom material for pure water (ICRU 35). By accounting for small discrepancies in material properties, dosimetric quantities in polystyrene can be corrected to correspond to measurements in water (Khan 1991). Lateral dimensions of the measurement phantom were chosen to be larger than twice the maximum electron range in polystyrene to maintain semi-infinite lateral geometry. The thickness of the measurement phantom was chosen to correspond to d_{max} for the 21-A linear accelerator.

A strip of GAFChromic film was inserted into the measurement phantom and aligned flush with the proximal face prior to each irradiation. An SSD of 60cm, measured to the top surface of layer 1, was maintained for all experiments. In order to compensate for edge artifacts seen by the scanning densitometer (Section 7.4.1), the length of the film was increased from 1.33cm to 2.0cm such that the film would extend beyond the distal edge. The excess length was folded along the interface between the phantom and scatterer during irradiation. Films were flattened prior to scanning.

6. The Monte Carlo Simulations

Computer simulations of all experiments were carried out using the ITS TIGER code (Halibleib 1992) and are described in Section 6.1. Section 6.2 outlines the method used to reconstruct the incident beam energy spectrum from Monte Carlo simulation of monoenergetic electron energy deposition kernels in water and the measured depth-dose distribution of the electron beam in water. Also, since backscattering experiments were conducted with a different SSD than that with which water tank measurements were made, it was necessary to develop a methodology for correcting for energy degradation in the air gap (Section 6.3).

6.1 Use of the ITS codes

Use of the ITS Code Package involves first running the cross-section generating code XGEN and then on of the Monte Carlo program files (TIGER, CYLTRAN, or ACCEPT). An input file was constructed for XGEN, in which the relevant material properties (composition, density, state) were specified for the materials used in the experiments. XGEN was executed to generate a data file containing electron and photon cross-sections for these materials for energies below 6.75MeV (the maximum beam energy) and above the minimum cut-off

energy at which a history is terminated (in this case 0.3375MeV for electrons and 0.001MeV for photons). This data file specified the material dependant properties for the Monte Carlo simulation, and a second input file was required to specify source parameters, geometry, and output options for a given problem. The following summarizes these parameters and their specification in the simulations.

SOURCE

The source was specified as a mono-directional beam, normally incident onto the face of the first slab. The beam energy distribution was specified as a histogram with energies ranging from 0.25MeV to 6.75MeV.

HISTORIES

The precision of any Monte Carlo calculation is determined inherently by counting statistics, and thus the number of histories followed. Applying Poisson statistics, the relative statistical uncertainty associated with the dose in a given region from a run of n histories varies as $n^{-1/2}$. Therefore, the number of histories must be quadrupled in order to half the statistical uncertainty. A practical consideration is that the computing time required for a particular run is directly proportional to the number of histories sampled. In this work, 10^5 electron histories were typically

sampled to provide sufficient precision (0.5%-2%) for all the relevant dose scoring regions in the TIGER code.

GEOMETRY

The experimental geometries were simulated by specification of the composite slab layer materials and thicknesses. Since the ITS codes permit the use of subzoning of up to 100 dose scoring regions, the thick slabs were further subzoned into thin dose scoring regions (1mm-100μm) in the direction perpendicular to the region of interest occupied by the radiochromic strip films. Specific problem geometries are discussed in Section 6.5.

OUTPUT

The energy deposition in each sub-zone was determined for each run. The ITS codes provide dose information in the form of the energy deposited per source quanta, thus normalizing dose with respect to the number of histories. For simulations of homogeneous geometries, the energy distribution was also determined by scoring the electron fluence within defined energy bins at various depths.

6.2 Determination of Electron Beam Energy Spectra from Central-Axis Depth-Dose Distributions

Depth-dose profiles in water of 6MeV (nominal) electron beams produced by three Varian CLINAC-2100C linear accelerators were measured with an electronic diode detector system (Scanditronix RFA 300). These three accelerators were coded as 21-A, 21-B, and 21-C. For each, 34 measurement points were taken at 1mm intervals along the beam central axis in order to obtain the depth-dose distribution for a 10x10cm field at 100cm SSD. The practical range R_p and depth R_{50} of 50% dose were determined from the water tank measurements. The following relationships can be used to estimate the most probable energy $E_{p,0}$ and mean energy $<E_0>$ at the surface from R_p and R_{50}, respectively (Brahme 1976):

$$E_{p,0} = 0.22 + 1.98 R_p + 0.0025 R_p^2$$

$$<E_0> = 2.33 R_{50}$$

In the above expressions, $E_{p,0}$ and $<E_0>$ have units of MeV and R_p and R_{50} are specified in cm.

One-dimensional Monte Carlo simulations of the central axis depth-dose distribution in water were generated for mono-energetic electron beams of 16

energies ranging from 0.5MeV to 8.0MeV in increments of 0.5MeV, using the TIGER code. One-dimensional geometry is assumed to apply to treatment fields much larger than the maximum electron range in water (i.e. 10x10cm or greater). The dose scoring regions were defined as 35 1mm sub-zones in a water slab 3.5cm thick. In the simulations, these regions were backed by a 10cm thick water region to ensure semi-infinite backscatter geometry along the beam central axis. The energy deposited, normalized to a single incident particle, was scored in each region.

Each of these depth-dose curves can be assigned a weight, w_i, such that:

$$D(x_j) = \sum_{i=1}^{m} w_i D(x_j, E_i)$$

where m(=16) is the number of energy bins, $D(x_j)$ is the dose at point x_j from the nominal 6MeV beam, and $D(x_j, E_i)$ is the dose contribution at point x_j from electrons of initial incident energy E_i. The resulting depth-dose curve was then normalized to correspond to the format of the measured depth-dose curve $D_e(x_j)$ for the nominal 6MeV beam as follows:

$$D^*(x_j) = \frac{D(x_j)}{\max[D(x_j)]}$$

For a given set of w_i, a normalized sum of variance statistic (v^2) can be calculated such that

$$v^2 = \sum_{j=1}^{n} \frac{[D_e(x_j) - D^*(x_j)]^2}{D_e(x_j)}$$

for a total number of n(=35) dose points. The computer program BEAMSPEC.BAS used to perform the optimization is listed in Appendix I.

The resultant optimized weights served as an estimate of the energy distribution (histogram) of the incident beam energy spectrum. Since the ITS codes permit the use of a histogram for the initial beam energy spectrum, the derived spectrum was then fed back into the source term of the TIGER simulation to verify the consistency of methodology. Characteristic beam energy parameters obtained from this method were compared to those derived from range measurements. In addition, the spectrum obtained for the 21-C by this method was compared to that obtained by Ding *et al.* (Ding 1994). They obtained this spectrum through the use of another Monte Carlo code (BEAM) in the three-dimensional simulation of the beam path through the treatment head and applicator.

6.3 Correction for SSD

While the depth-dose measurements in water used to estimate the incident electron beam spectrum were measured at a SSD of 100cm, the backscattering experiments were performed at a SSD of 60cm. The air gap traversed by the incident beam was reduced by 40cm (0.0482g/cm^2); thus, the incident spectrum at 60cm SSD experienced less energy degradation. Since the mass-thickness of the air gap is relatively small, its effect on the spectrum can be expected to be similarly small. With this assumption, the CSDA stopping power was used to adjust each of the energy bins from the 100cm surface spectrum upwards in energy to correct for beam energy degradation in the air gap.

The CSDA stopping power is defined as:

$$S(E) = -\frac{dE}{dx}$$

Thus, the change in energy experienced by an electron in travelling from 60cmSSD to 100cm SSD is given by:

$$\int dE = \int_{100}^{60} S(E)\, dx$$

Since the air gap (and hence the change in energy) is relatively small, the following approximation to the above was used:

$$E_i' = E_i + S(E_i)_{air}\, \Delta x$$

where E_i and E'_i are the energies at 100cm and 60cm, and Δx is the mass-thickness of the air gap.

To apply this methodology numerically, the total CSDA stopping power in air was determined for each of the energy bin end points, $0.25 < E_i < 6.75$MeV. Each E_i was then incremented by an amount equal to the energy assumed to be lost while traversing the air gap. This was equated to as the product of the CSDA total stopping power at that energy $S(E_i)$ and the mass thickness of the air gap. New end points (E'_i) for the spectrum at 60cm were generated through this process.

This new histogram had bins of equal height as the initial spectrum, but different bin energies and bin widths (since the energy shift is non-linear). Thus, the next step was to normalize the energy histogram at 60cm SSD, using

the same energy bin width as in the initial spectrum. Consider the corrected energy spectrum histogram before normalisation, which has bins of height (y'_i) between the limits E'_i and E'_{i-1}. To find the histogram y_i with bins at E_i, the following approximation was used:

$$y_i = y'_{i-1}(E'_i - E_i) + y'_i(E_{i+1} - E'_i)$$

The above was based on conservation of area, and assumes rectangular energy bins.

The energy spectrum at 60cm SSD, expressed as a histogram with the same energy bin definitions as the original spectrum, was thus evaluated. To verify this methodology, the derived 60cm SSD spectrum was used as input in a TIGER simulation of energy degradation in a thick slab of air. Energy fluence was scored at a nominal distance of 40cm into the slab. The resultant spectrum was compared to the initial spectrum at 100cm SSD.

6.4 Simulations

6.4.1 Homogeneous Geometry

Preliminary Monte Carlo simulation of homogeneous conditions played a role in optimizing conditions for the experiments and in analysis of the sensitometry results. Simulation of electron transport in semi-infinite water was used in energy spectrum determination and also in determination of the energy response of the radiochromic film over the range of relevant electron energies. Additionally, a Monte Carlo run was performed to determine depths corresponding to R_{20} and R_5 in semi-infinite polystyrene, in order to supplement the parallel-plate measurements of the depth-dose distribution.

TIGER simulations were performed to determine the depth-dose and depth-energy distributions for both water and polystyrene. The simulation geometry consisted of 40 identical zones, each of 1mm in thickness (TIGER does not permit subzoning in energy scoring). The energy deposition in each zone was scored to determine the depth-dose distribution. The energy distribution in each zone was sampled by scoring the energy fluence in 50 evenly spaced energy bins from the maximum source energy (6.75MeV) to the cutoff energy (0.3375MeV). The average energy as a function of depth $\langle E \rangle(x)$ was determined as the simple weighted average of the product of

mean bin energy and fluence scored in each energy bin. Mean bin energy was taken at the mid-point of the energy bin. The most probable energy $E_p(x)$ was taken as the mid-point energy of the bin showing the maximum fluence at that depth.

6.4.2 Heterogeneous Geometry

Simulation of the backscatter experiments was designed to match experimental conditions. Since the film has the advantages of being thin and equivalent in composition to the polystyrene in which it was held, it was not necessary to simulate the presence of film explicitly in any Monte Carlo runs. Subzones for the film-containing region of the phantom were defined to be 100μm thick in order to correspond to the step size of the scanning densitometer. Since this requires a greater number of subzones than the code permits, two runs of each geometry were performed, with scoring in 100μm regions from 0.00mm to 0.43mm and from 0.43mm to 1.33mm, respectively. Simulation geometry is shown in Figure 6.1.

Since the electron range in air greatly exceeds the dimensions of the phantom, the condition of semi-infinite geometry for air is not met. To compensate, TIGER simulations were carried out using a vacuum as the scatterer, rather than air.

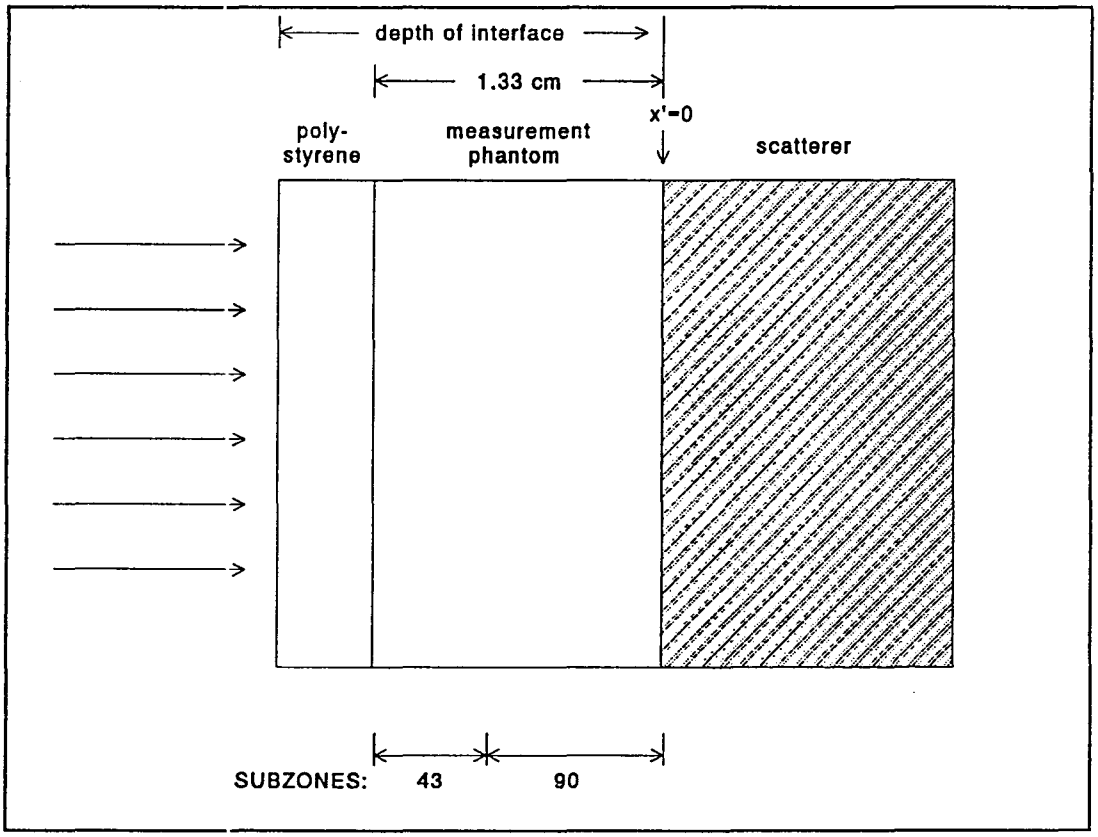

Figure 6.1: TIGER simulation geometry.

PART III: RESULTS

7.1 Electron Beam Energy Spectrum Determination

7.1.1 100cm SSD Beam Energy Spectrum Determination from Water Tank Depth-Dose Measurements

Electron beam energy spectra were determined for three CLINAC 2100C (Varian, Inc., Palo Alto CA) linear accelerators (coded as 21-A, 21-B, and 21-C) using the least-squares variance reduction method outlined in Section 5.1. Figure 7.1 shows the monoenergetic electron energy deposition kernels in water generated by the TIGER code. The v^2 fitting statistic is shown in Table 7.1 for each accelerator, and the 6MeV electron beam energy histograms obtained for 21-A and 21-B are shown in Figure 7.2. Figure 7.3 shows the energy histogram obtained for the 6MeV electron beam from the 21-C linear accelerator through this method in comparison to that obtained by Ding *et al.* (Ding 1993) using the BEAM code. For each histogram, the energy parameter $E_{p,0}$ was taken as the mode of the distribution, and $<E_0>$ was calculated as the simple weighted average of mean bin energies. The beam energy parameters derived from this work, those derived from Ding's energy histogram, and those derived from the water tank measurements are compared in Table 7.2. The 6MeV depth-dose curves reconstructed from the monoenergetic deposition kernels (symbols) are shown with the water tank measurements (lines) in Figure 7.4. Results of the TIGER simulation of depth-dose in water using the

spectrum determined through BEAM simulation for the 21-C (□) were included in the same plot.

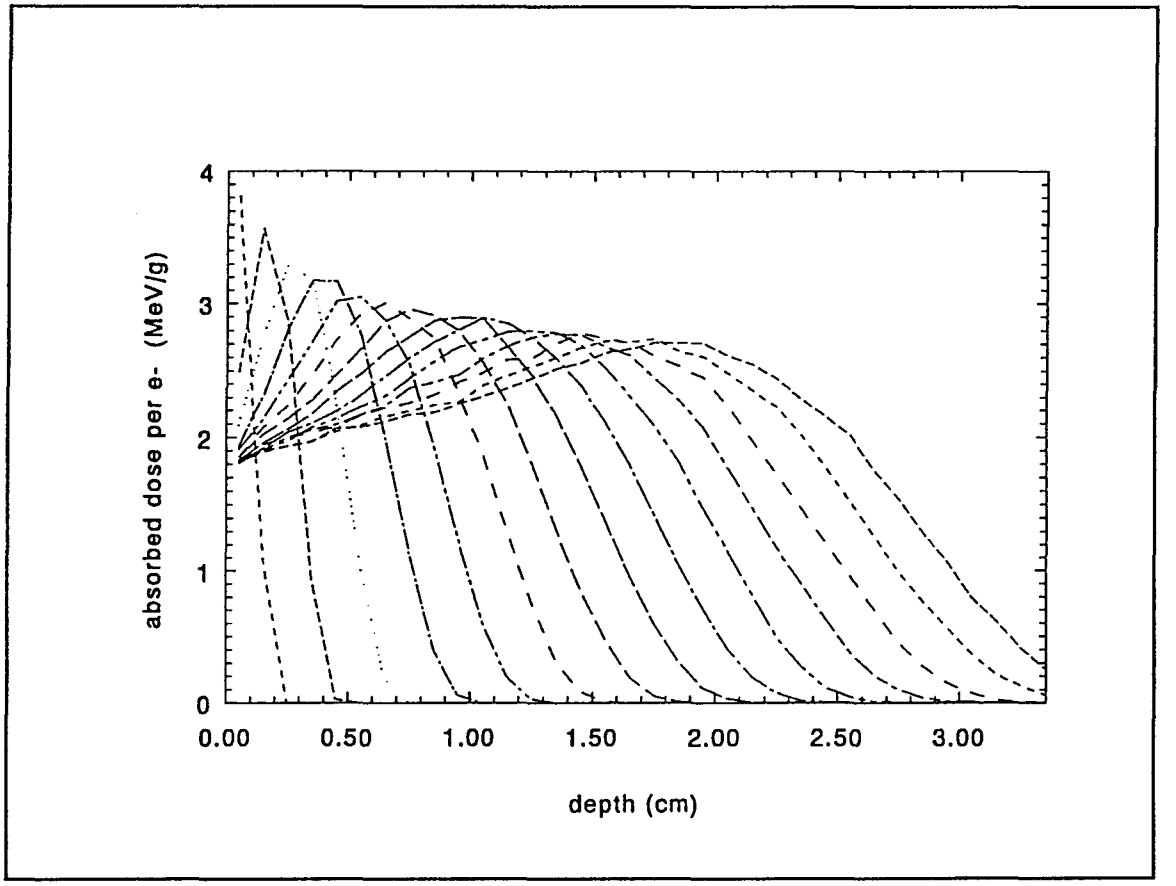

Figure 7.1: TIGER simulation of depth-dose profiles for monoenergetic electron beams in water: 0.5MeV (left), 1.0MeV, ... , 7.5MeV, 8.0MeV (right).

Table 7.1: Fitting Parameters

LINAC	Data Points	Energy Bins	v^2
21-A	34	13	2.2E-03
21-B	34	14	2.1E-03
21-C	34	15	7.3E-04

Table 7.2: Derived Energy Parameters (6MeV electron beams at 100cm SSD)

LINAC	Spectral Energy Parameters (MeV)			BEAM Simulation: Spectral Energy Parameters (MeV)			Measured Ranges in Water		Energy Parameters Derived from Water Tank Data (MeV)	
	E_{max} ±0.25	$E_{p,0}$ ±0.25	$<E_o>$	E_{max}	$E_{p,0}$	$<E_o>$	R_{50} (cm)	R_p (cm)	$E_{p,0}$	$<E_o>$
21-A	6.5	5.5	5.05				2.16	2.71	5.60	5.03
21-B	7.0	6.0	5.28				2.30	2.84	5.86	5.36
21-C	7.5	7.0	5.87	7.1	6.85	6.11	2.60	3.21	6.60	6.06

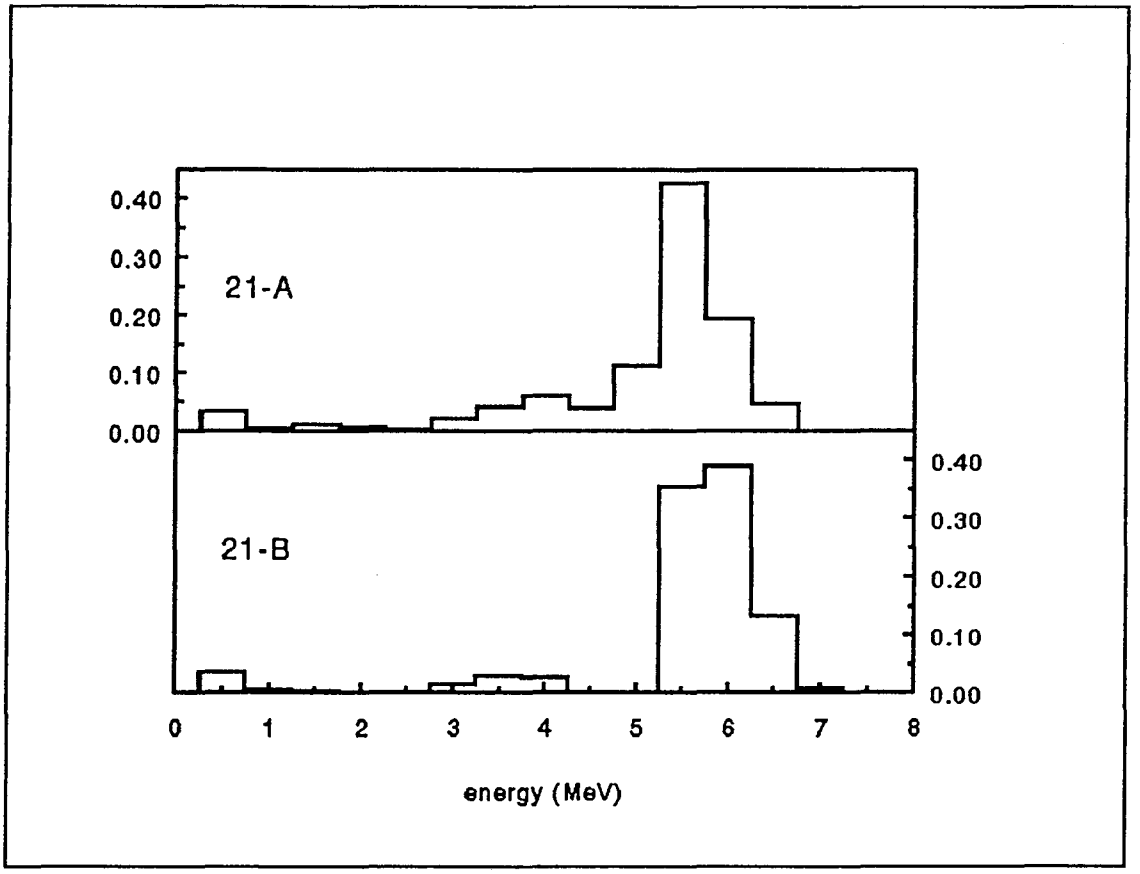

Figure 7.2: Derived beam energy spectra for 21-A and 21-B 6MeV electron beams

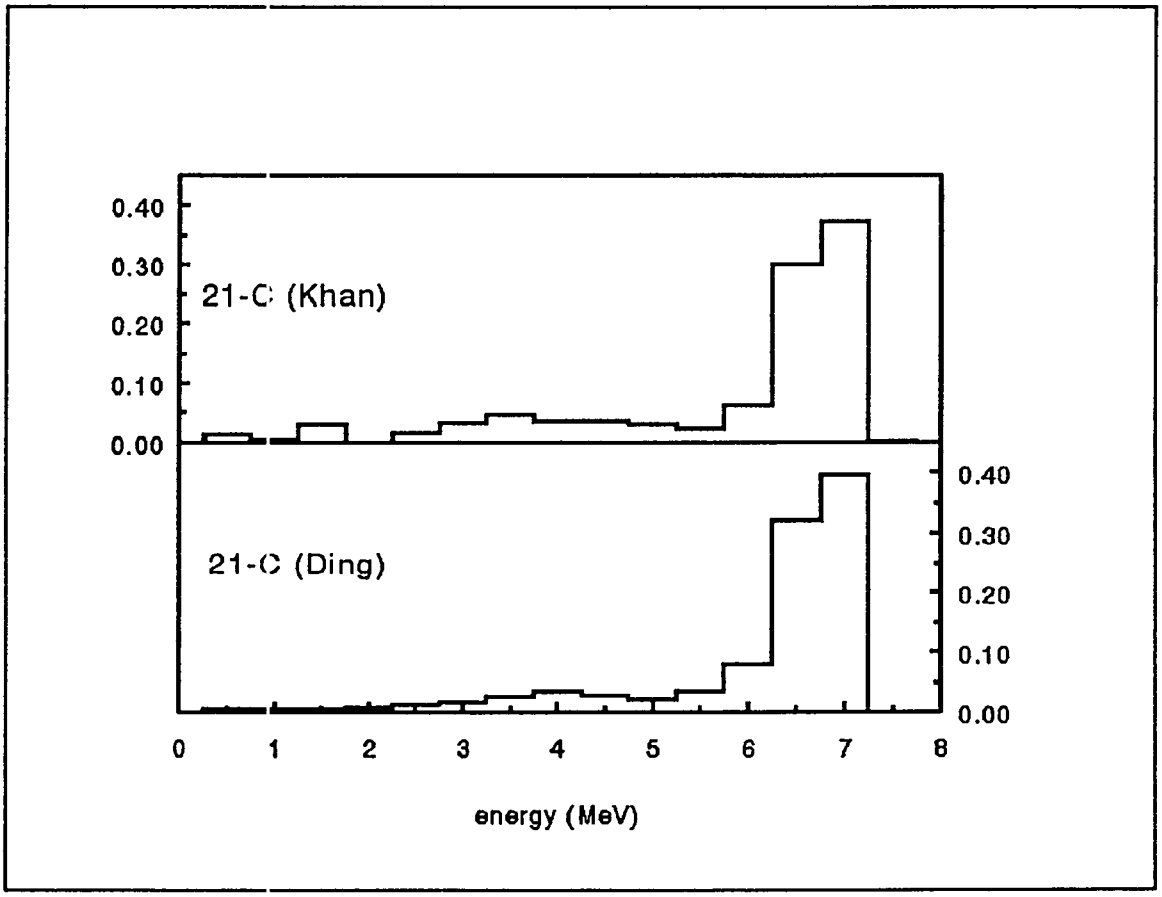

Figure 7.3: Derived 6MeV electron beam energy spectrum for 21-C (top). Spectrum based on BEAM simulation of treatment head and applicator (below) by Ding *et al.*

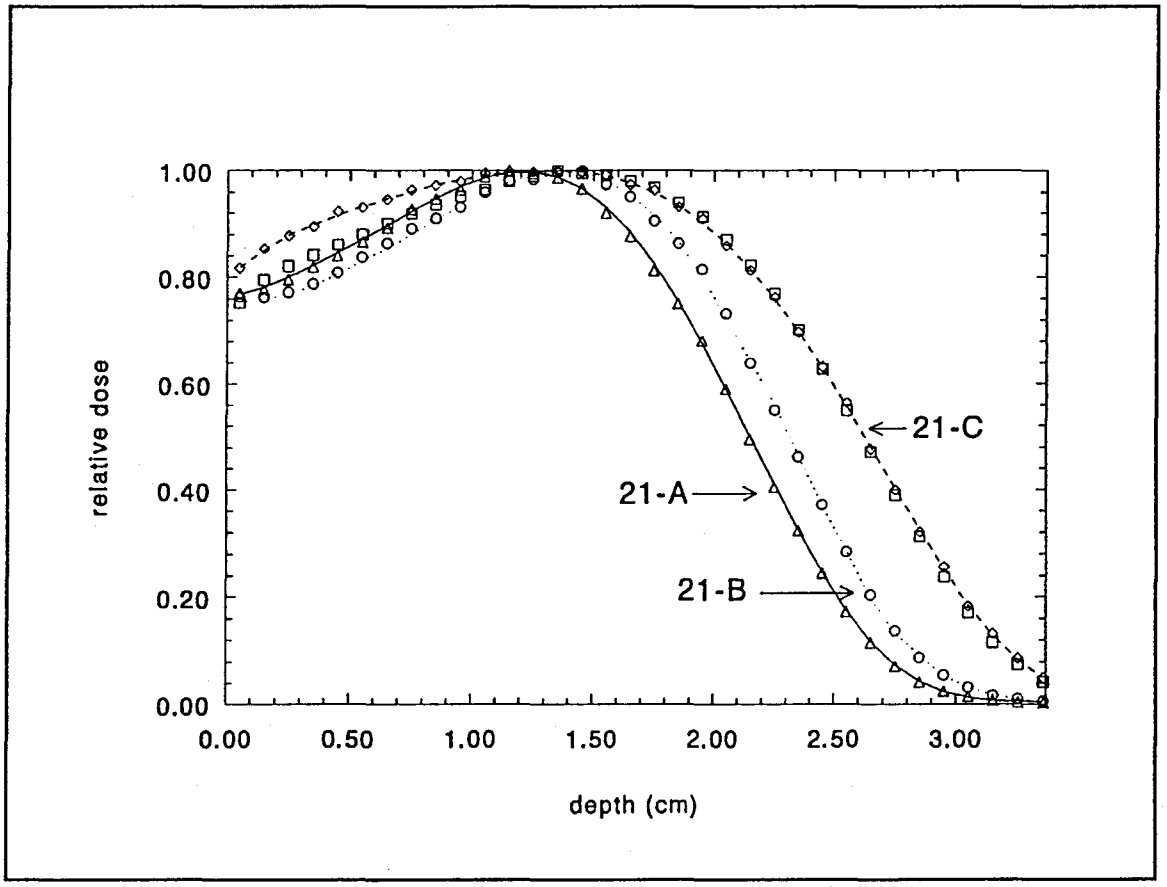

Figure 7.4: 6MeV electron depth-dose distribution measurements (lines) and TIGER simulations in water for three CLINAC 2100-C linear accelerators (symbols)

7.1.2 Beam Energy Spectrum Corrected to 60cm SSD

The energy spectrum for linac 21-A at 60cm SSD (dotted curve, top panel), as determined through the applied CSDA correction to the spectrum at 100cm SSD (solid curve, top panel) is shown in Figure 7.5. To verify the methodology used, the CSDA corrected spectrum at 60cm SSD was used as the input source spectrum in a TIGER simulation of electron transport in a 40cm thick, laterally infinite, slab of air. The energy fluence spectrum was sampled in a 1cm scoring region centred at a depth of 40cm, backed by 20m of air. The lower panel of Figure 7.5 shows the derived 60cm SSD spectrum (solid) and the fluence scored at a depth corresponding to 100cm SSD (dotted). Through this validation process, the original energy spectrum at 100cm was recovered to within 0.18 (5% of maximum) for each bin overall, and to within 0.005 (1%) for energy bins greater than 0.5MeV. The CSDA corrected energy spectrum at 60cm SSD, as shown in Figure 7.5 (top panel, dotted), was used in all subsequent Monte Carlo runs in simulating experimental conditions that used 60cm SSD.

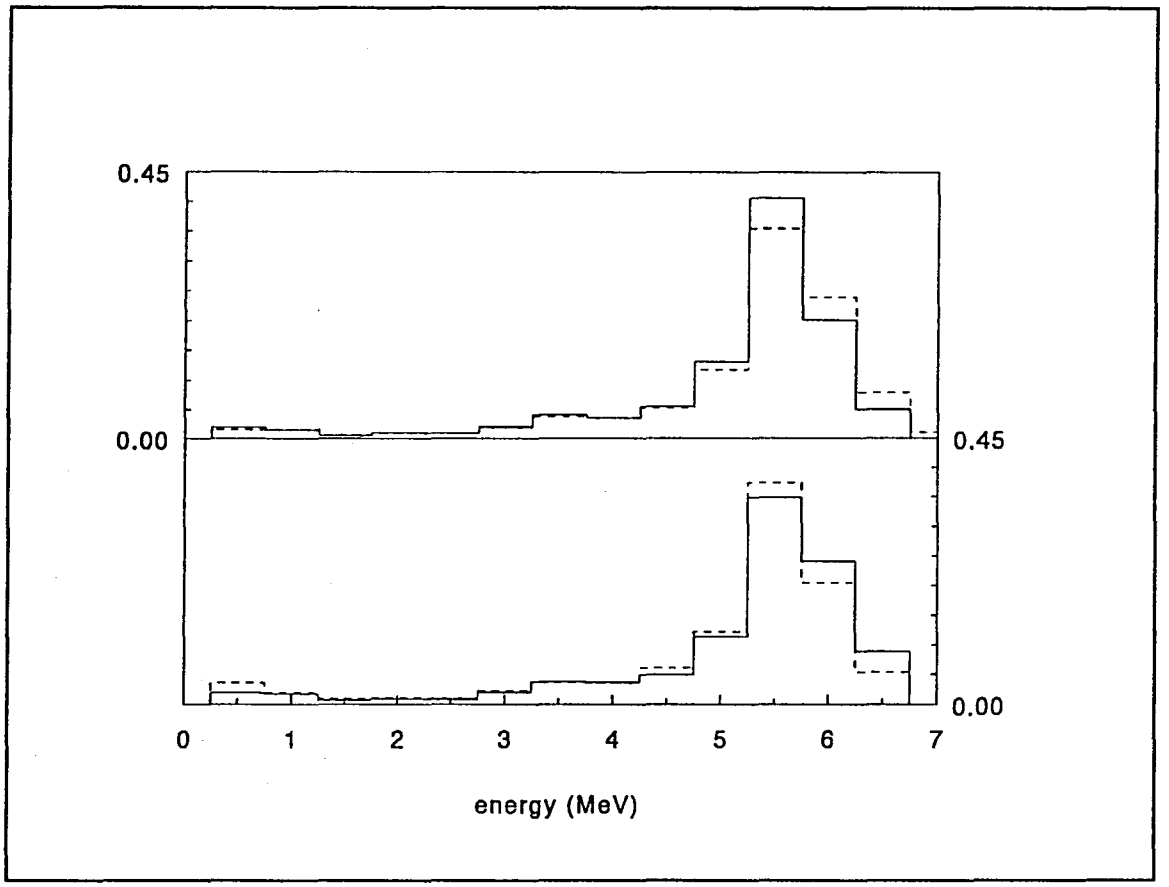

Figure 7.5: Results of CSDA SSD Correction. Top panel, 100cmSSD spectrum (continuous) used to derive 60cmSSD spectrum (dotted). Bottom panel, 60cmSSD (continuous) spectrum simulated at $\Delta x = 40$cm (dotted).

7.2 Monte Carlo Simulation of Homogeneous Conditions

7.2.1 Depth-Energy in Water

The depth-mean energy distribution in water for linac 21-A at 100cm SSD determined through TIGER simulation is shown below in Figure 7.6, with Harder's approximation (Harder 1966).

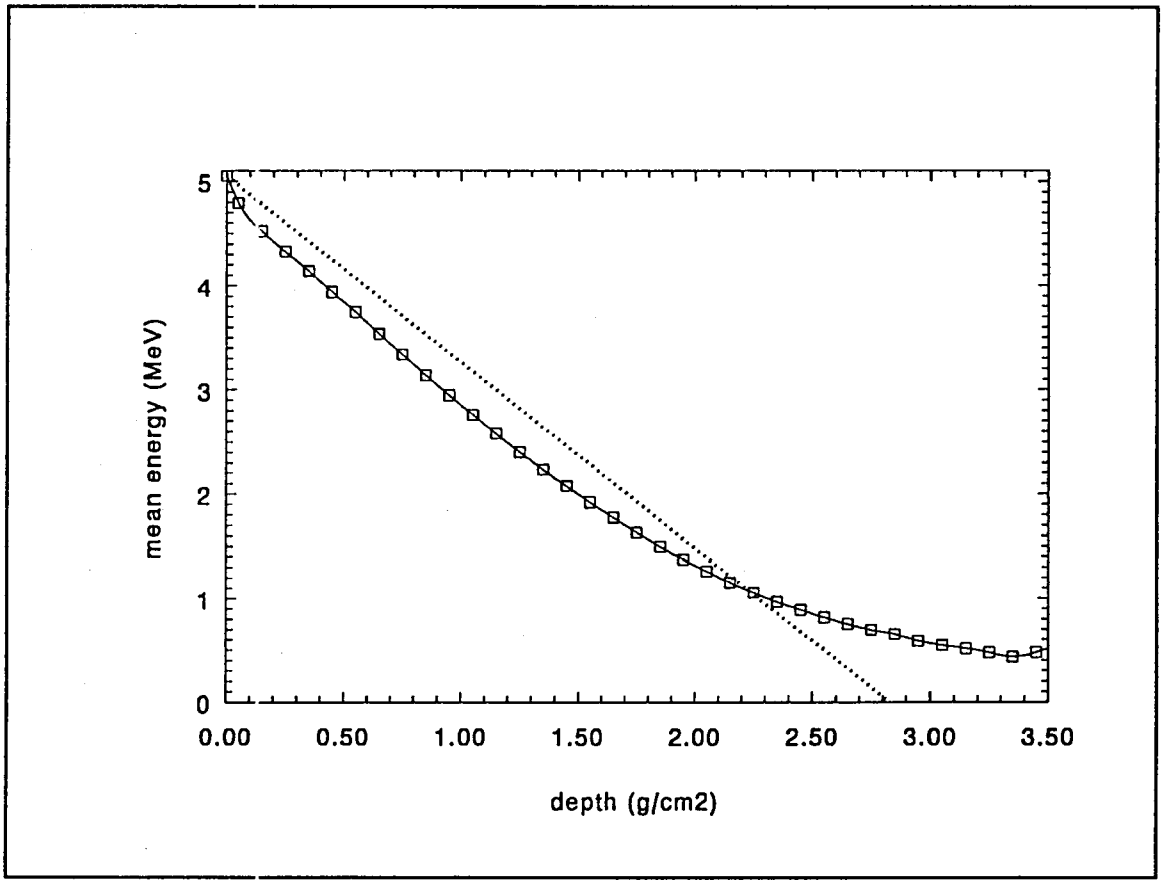

Figure 7.6: Depth-mean energy distribution for 6MeV electrons in water based on TIGER simulation (□), and Harder's approximation (dotted)

7.2.2 Depth-Dose and Depth-Energy in Polystyrene

TIGER simulation of the depth-dose and depth-energy distributions in a semi-infinite polystyrene phantom is shown in Figure 7.7 for linac 21-A (60cm SSD). The depth-dose distribution obtained was verified against parallel plate ionization chamber measurements (Figure 7.8). These results showed agreement within 5% over the region from the surface to 2.2g/cm^2 (~55% dose), and to within 10% up to R_5. Uncertainties in the simulation values were 0-2%, while the uncertainty in parallel plate measurements was negligible since relative measurements were used.

The energy fluence distributions scored at depths corresponding to placement of the interfaces in the backscatter experiments are shown in Figure 7.9. Mean and most probable energies at each of these depths are summarized in Table 7.3, below.

Table 7.3: Mean and most probable energies at d_{max}, R_{20}, and R_5

	Depth in polystyrene		% Dose (nominal)	$<E_0>$ (MeV)	$E_{p,0}$ (MeV)
	(cm)	(g/cm^2)			
d_{max}	1.330	1.390	100	2.26 ± 0.01	2.90 ± 0.07
R_{20}	2.593	2.710	20	0.79 ± 0.02	0.54 ± 0.07
R_5	2.935	3.086	5	0.58 ± 0.03	0.34 ± 0.07

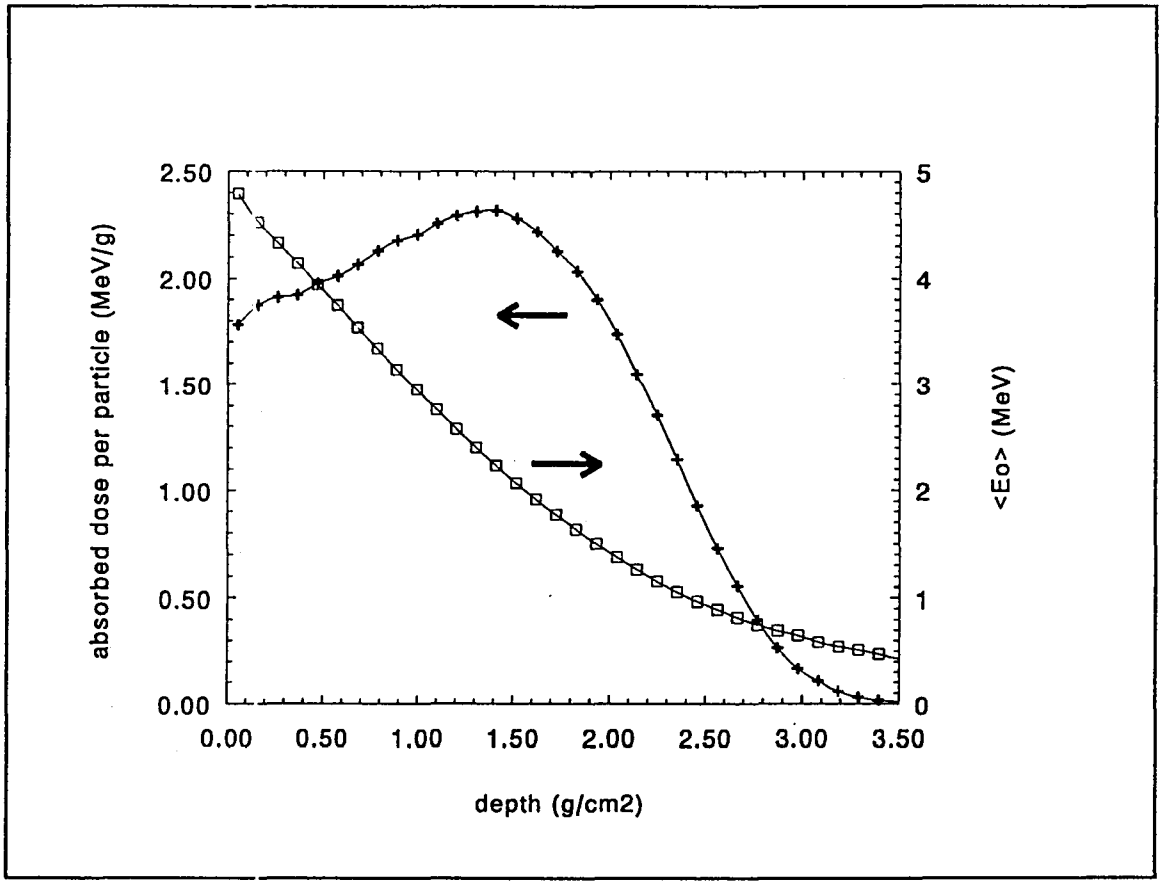

Figure 7.7: 6MeV electron absorbed dose (+) and mean energy (□) distributions in polystyrene at 60cm SSD based on TIGER simulations

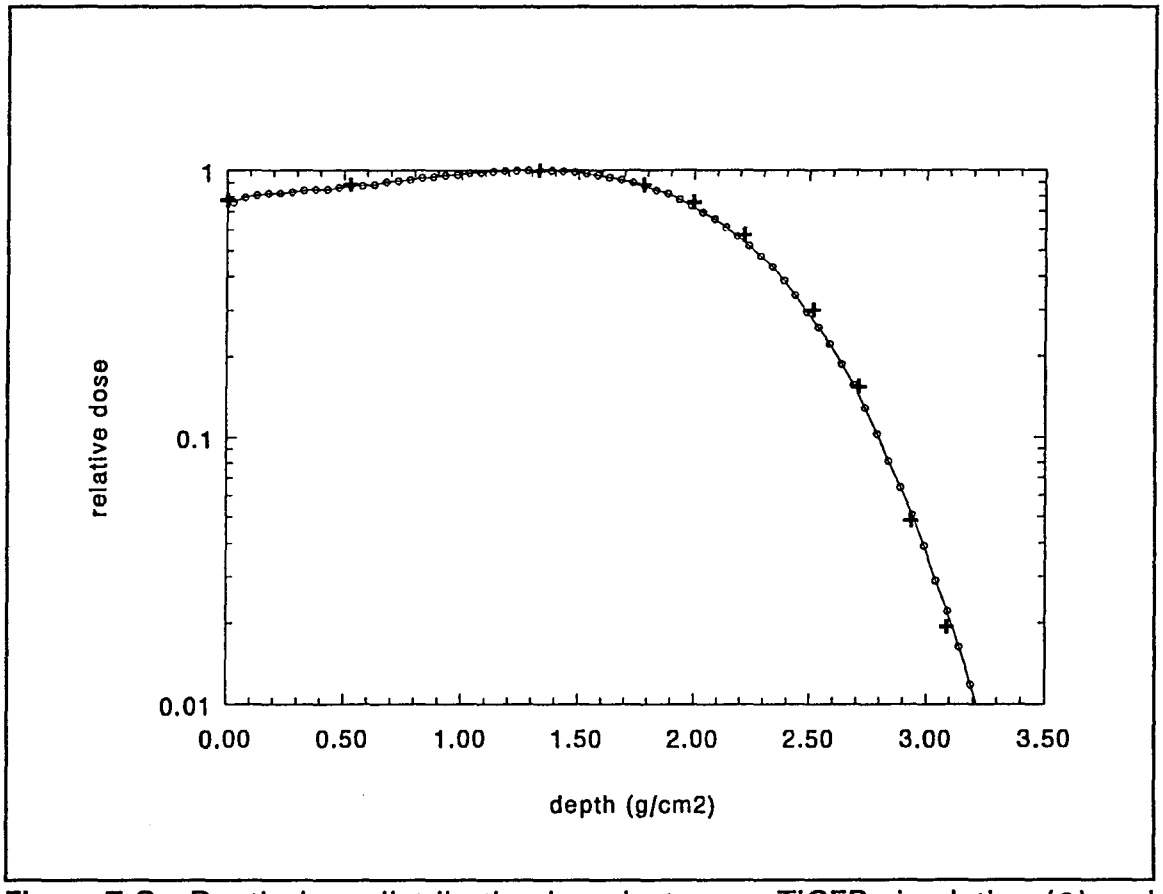

Figure 7.8: Depth-dose distribution in polystyrene, TIGER simulation (o) and parallel plate ionization chamber measurements (+)

Fig 7.9: TIGER simulated e- energy dist'n at surface, Dmax, R20, and R5

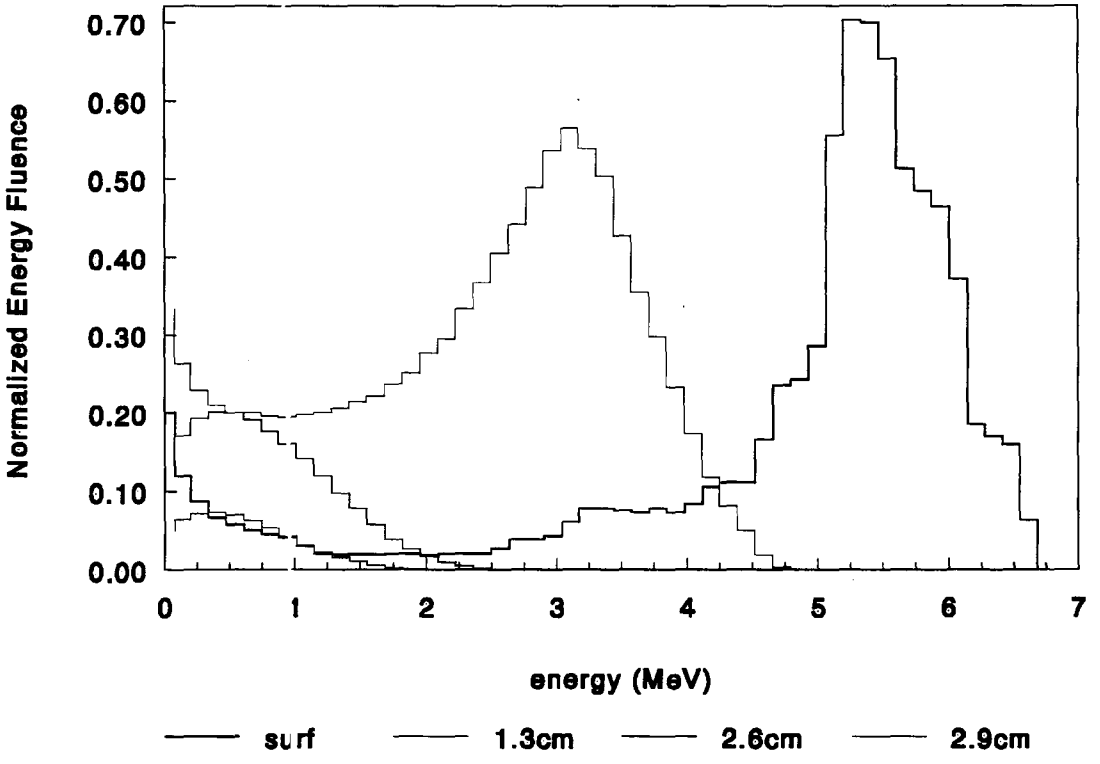

7.3 Spectrophotometry

The spectral dose response of GAFChromic Type 37-041 film was analyzed using the spectrophotometry techniques outlined in Section 5.2 for films uniformly irradiated with 6MeV electron and ^{60}Co (1.2MeV average energy) photon radiations. Results are presented for two batches of film, coded as "Batch #1" and "Batch #2" (Section 5.1).

7.3.1 Spectral Response of GAFChromic Type 37-041 Radiochromic Film for 6MeV Electrons

The spectral dose response was determined for Batch#1 radiochromic films which were uniformly irradiated with 6MeV electrons. Transmission measurements were made for each film, over the range of wavelengths $440nm \leq \lambda \leq 760nm$, at doses ranging from 0.5Gy to 263Gy. Each film was scanned over the above wavelength range using a 2nm step size. Irradiated film measurements were performed alternately with those for a non-irradiated background film in order to minimize the effects of instability in the spectrophotometer. Optical density $OD(\lambda)$ for each film i (i=1 to 3) was calculated as:

$$OD(\lambda)_i = \log\left[\frac{I_0(\lambda)_{i-1} + I_0(\lambda)_{i+1}}{2}\right] - \log\left[I_i(\lambda)\right]$$

where $I_0(\lambda)_{i-1}$ and $I_0(\lambda)_{i+1}$ are the transmitted intensities of the background film read prior to and after the i^{th} irradiated film, and $I_i(\lambda)$ is the transmitted intensity of the irradiated film.

The average dose responses for three replicate films which were irradiated at 26-236Gy and 0.5-13Gy are shown in Figures 7.10 and 7.11, respectively. Error bars in these plots indicate one standard deviation, determined from the three replicate films. The characteristic absorption spectrum in Figure 7.10 consists of a main and a minor peak, as well as shifts of these peaks to lower wavelength with increasing dose. A logarithmic plot of the absorption spectra for the films in Figure 7.10 (Figure 7.12) reveals that the shape of the response curve remains constant, and that the increase in absorbance with dose over the entire visible range is accompanied by an overall shift to lower wavelengths.

Figure 7.13 shows the magnitude of absorbance and location of the main peak as a function of absorbed dose. A linear least-squares fit performed on the former showed excellent linearity in the response of maximum OD to dose ($r=0.999$). The shift in the location of the absorbance peak with increasing dose (from 680nm at 0Gy to 660nm at 263Gy) is non-linear.

Nominal 6MeV dose response functions (Figure 7.14) were generated using the OD values obtained at single wavelengths ranging from 560nm to 672nm. The curves on this figure represent the best-fit second order polynomial for each data set. The following general observations describe the single wavelength dose response characteristics. Since 560nm corresponds to the lower tail of the secondary absorbtion peak, this wavelength shows relatively low sensitivity to dose. 600nm corresponds to the location of the minor absorbtion peak at high dose, and thus shows greater sensitivity. Maximum sensitivity occurs in the region of 660nm, since this corresponds to the location of the major absorption peak at high doses. The effect of the frequency shift with dose can be seen well in the 672nm response curve, which initially shows high sensitivity to dose but saturates at approximately 260Gy as the main peak shifts away from this wavelength.

Fig 7.10: Absorption spectra for 6MeV doses of 263, 132, 79, 52, and 26 Gy

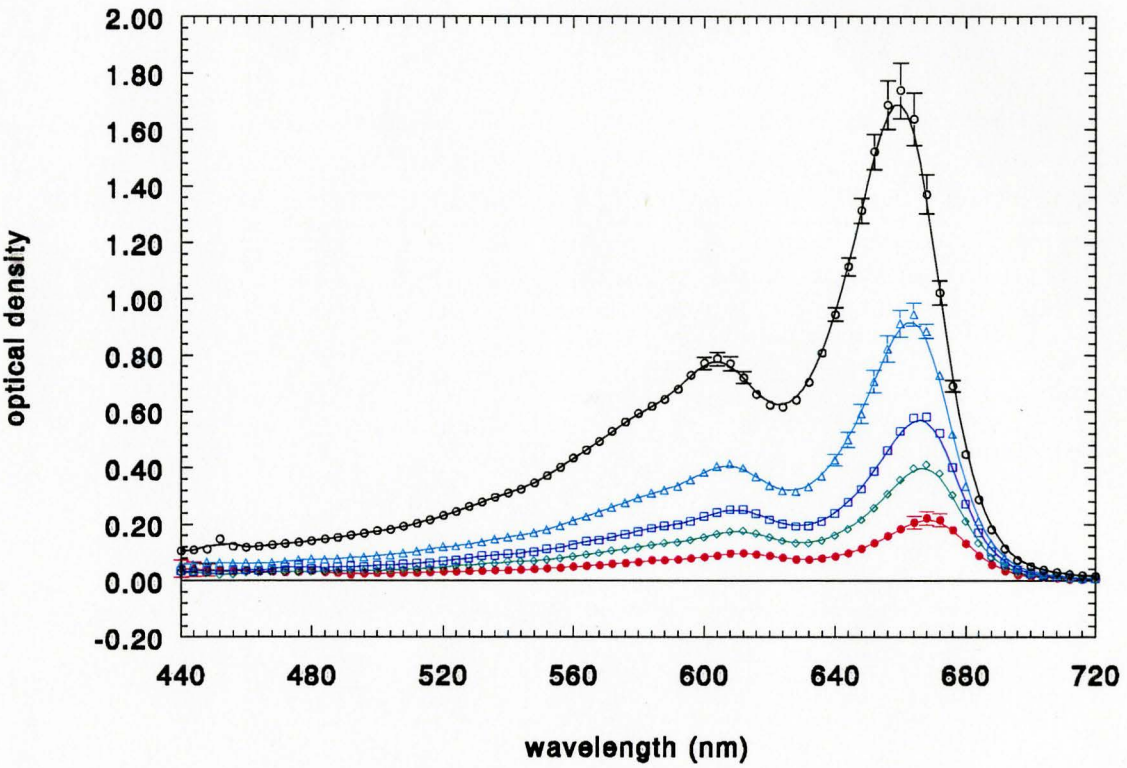

Fig 7.11: Absorption spectra for 6MeV doses of 13, 5.2, 2.6, 1.3, 0.5 Gy

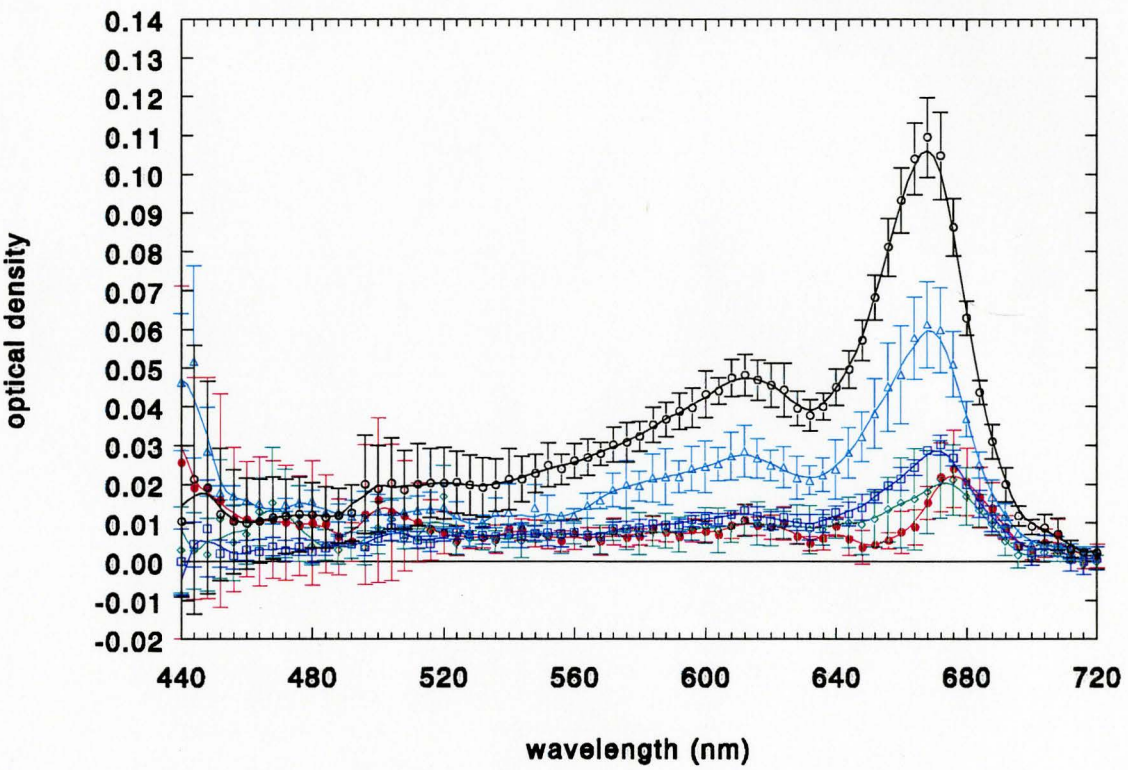

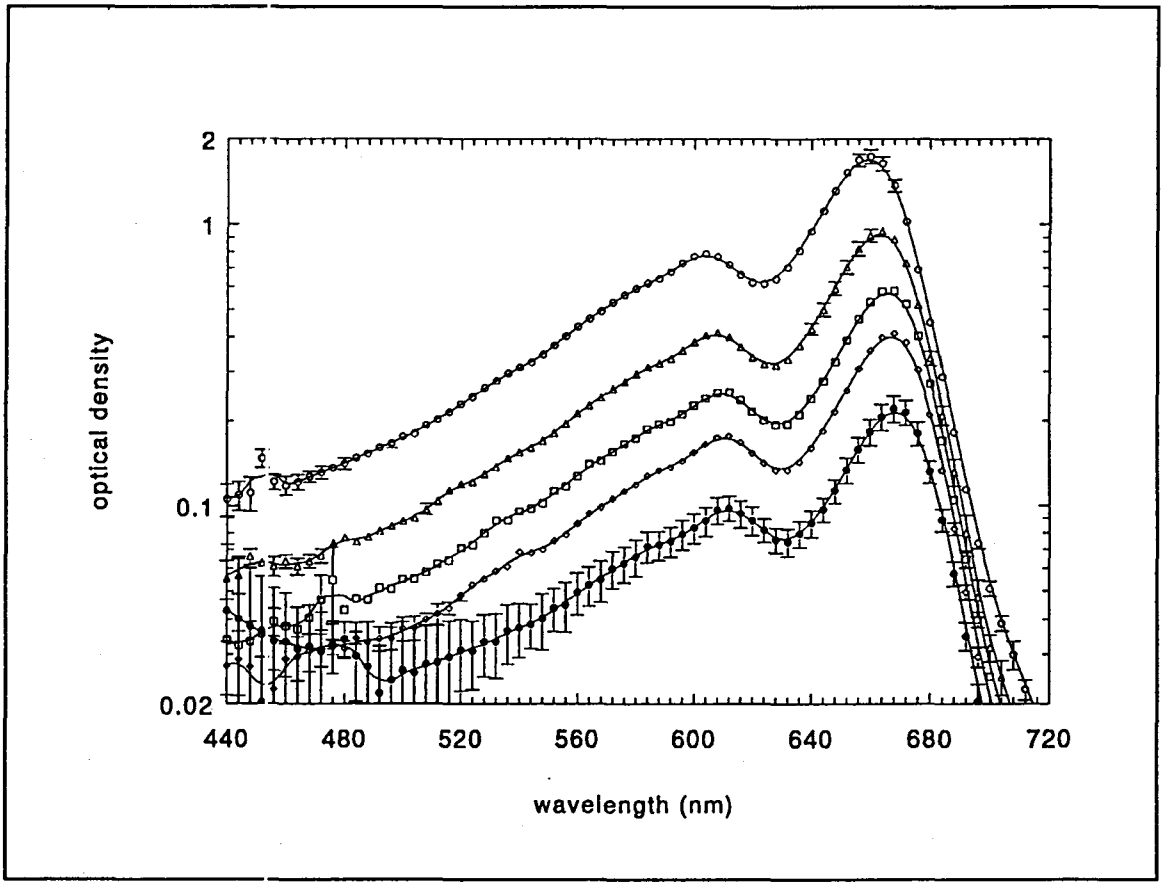

Figure 7.12: Absorption spectra for 6MeV electron doses of 263Gy to 26Gy with logarithmic ordinate (logarithmic plot of Figure 7.10)

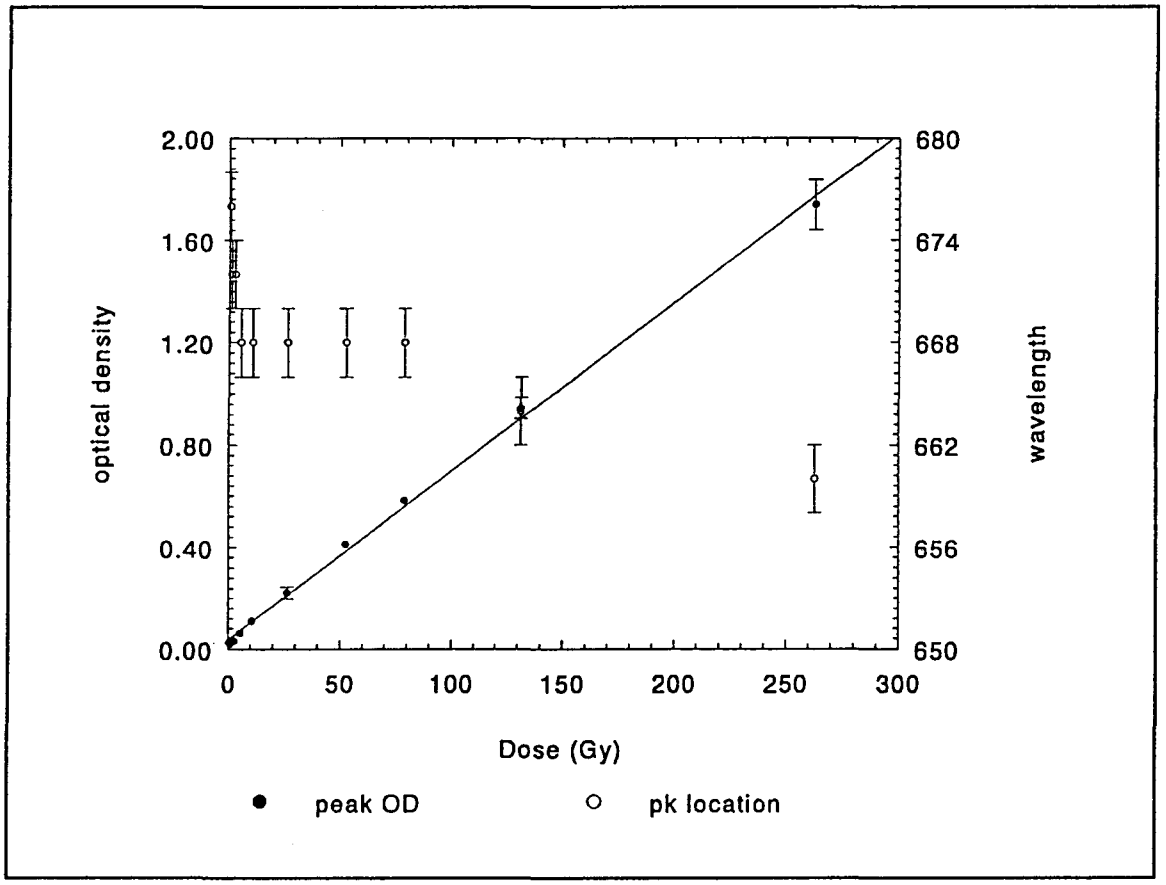

Figure 7.13: Dose's optical density response of main absorption peak (●) and peak location (○) for 6MeV electron irradiations

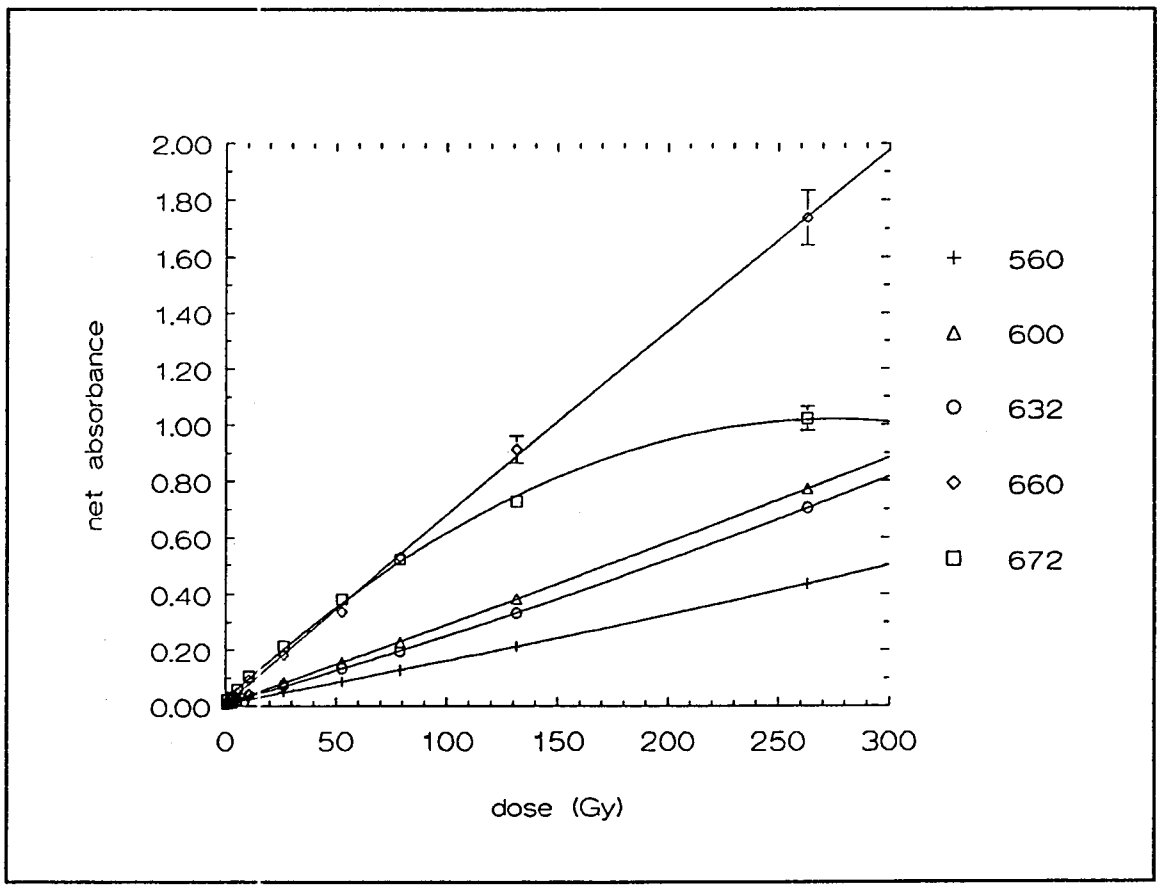

Figure 7.14: Single wavelength dose response for 6MeV electrons

7.3.2 Spectral Response: ^{60}Co Irradiations

A plot of the dose response of Batch #1 films irradiated with ^{60}Co photons (Figure 7.15) reveals a significant decrease in sensitivity, relative to the same batch of films irradiated with 6MeV electrons. The relative sensitivity for ^{60}Co radiation with respect to 6MeV electrons was investigated by calculating the ratio of doses required to produce a prescribed OD (0.5 and 1.0) from the fitted calibration functions at 600nm, 632nm, and 660nm for both types of radiation (Table 7.4).

Table 7.4: Relative sensitivity of ^{60}Co to 6MeV electron irradiations

wavelength (nm)	OD	dose value for prescribed OD (Gy)		$\frac{\text{electron dose}}{^{60}\text{Co dose}}$
		^{60}Co	6MeV electron	
600	0.5	206.6	171.9	0.80
632	0.5	235.8	192.6	0.78
660	1.0	170.0	148.2	0.85

These findings indicate a significant energy dependence of the sensitivity of Batch #1 films for ^{60}Co and 6MeV electron radiations. A reduction in sensitivity with decreasing photon energy was observed by Chiu-Tsao *et al.* (Chiu-Tsao 1994). They have reported relative sensitivities of 0.93 for ^{137}Cs and 0.56 for ^{125}I (^{60}Co = 1.00) for OD measurements with both 632.8nm and broadband densitometers. The above findings are inconsistent with the results of previous

sensitometry work using GAFChromic Type 37-040 (McLaughlin 1990) and claims by the distributor of the Type 37-041 film that there is no energy dependence for these films.

Figure 7.15: Single wavelength dose response for Co-60 and 6MeV electrons

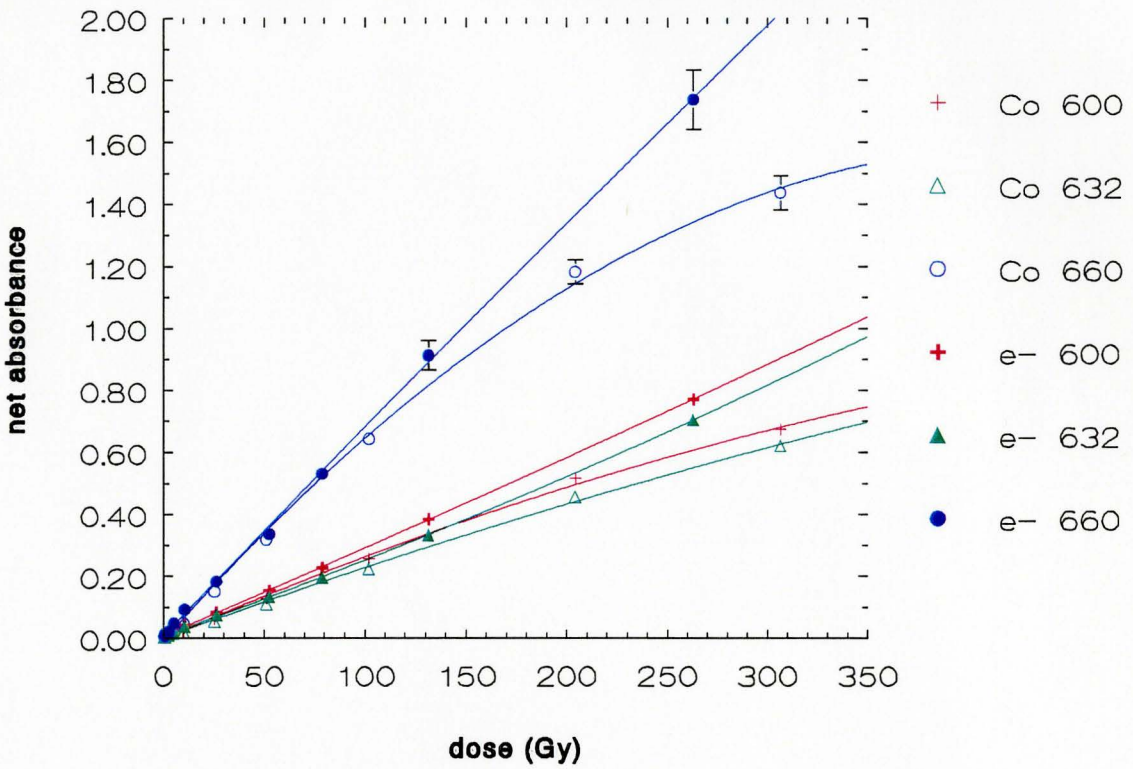

7.3.3 Batch #2 Results

Preliminary analysis of results from 6MeV irradiations of films from Batch #2 indicated that the sensitivity of these films was much greater than that of Batch #1. The above experiments (Sections 7.3.1 and 7.3.2) were subsequently repeated using films from Batch #2. The corresponding single wavelength calibration curves (Figures 7.16 and 7.17) indicate that film from this batch was approximately four times more sensitive than those from Batch #1. However, similar response characteristics (taking overall sensitivity into account) including energy dependence were observed for both Batch #1 and #2 film. Results of further analysis of response characteristics of this film and investigation of the electron energy response are presented in Section 7.4.

Figure 7.16: Batch #2 results for 6MeV electrons

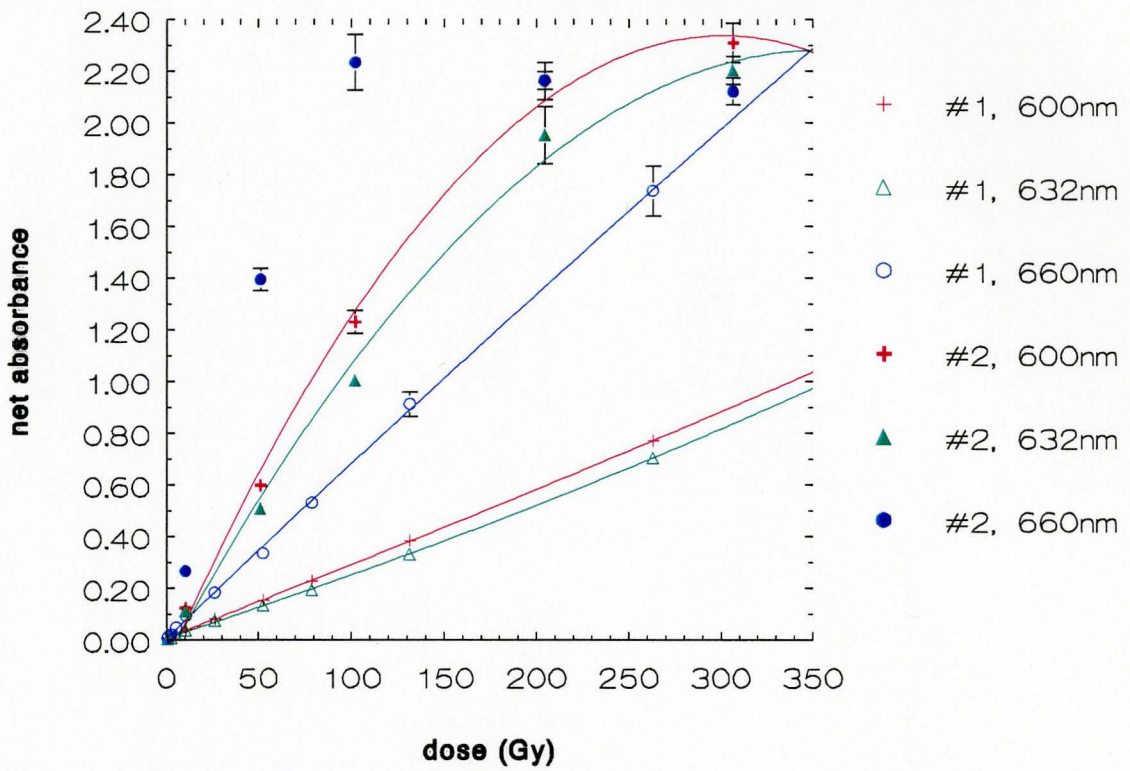

Figure 7.17: Batch #2 results for Co-60

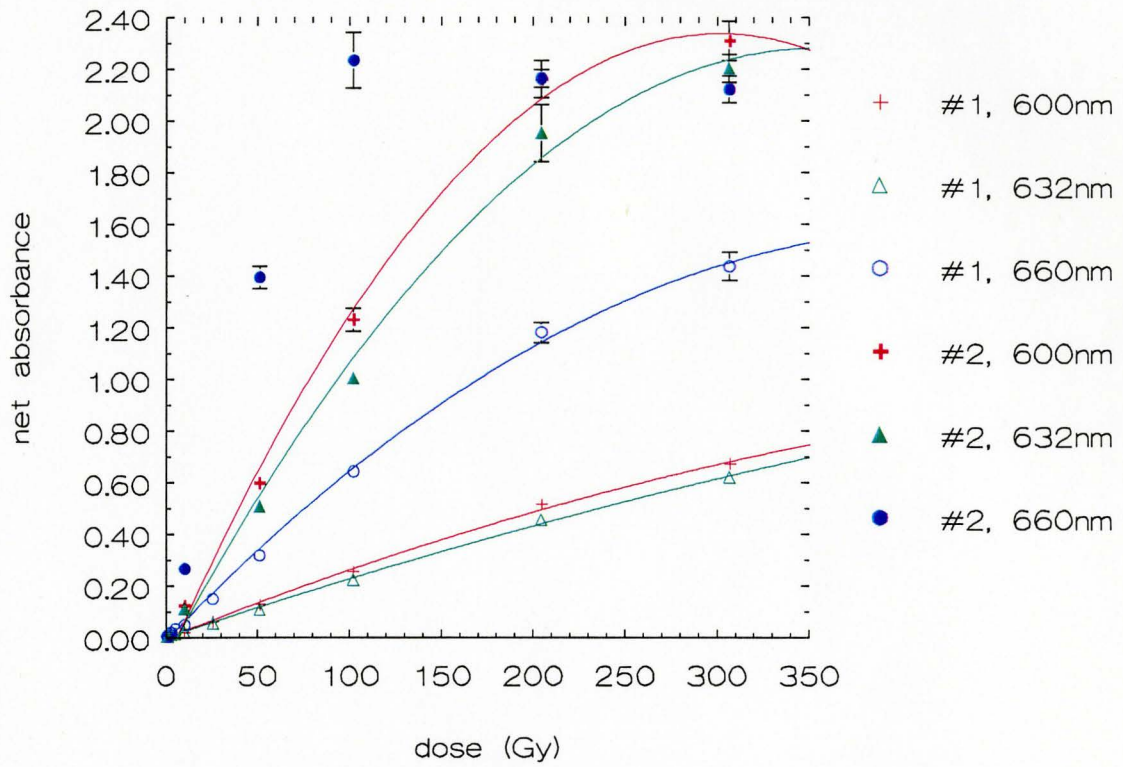

7.4 Sensitometry

7.4.1 Nominal Dose Response

6MeV Electron Calibration Curve at d_{max}

The calibration curve for 6MeV electrons obtained with the RIT113 system for Batch #2 film is shown in Figure 7.18. A least-squares fit of a linear function to the calibration data yielded the following calibration function (Section 5.2):

$$D = OD \times C_0$$

$$C_0 = 102.2 \pm 0.7\ Gy$$

The correlation coefficient r for the fit was 0.9990. Since the calibration function is linear, relative measurements can be compared directly. For example, consider the dose values D_1 and D_2, different positions 1 and 2 in a film. Since dose response is linear, the relative dose is given by the simple relationship:

$$\frac{D_1}{D_2} = \frac{OD_1}{OD_2} = \frac{PV_1 - PV_0}{PV_2 - PV_0}$$

where D_i, OD_i, and PV_i are the dose, net optical density, and pixel value (total

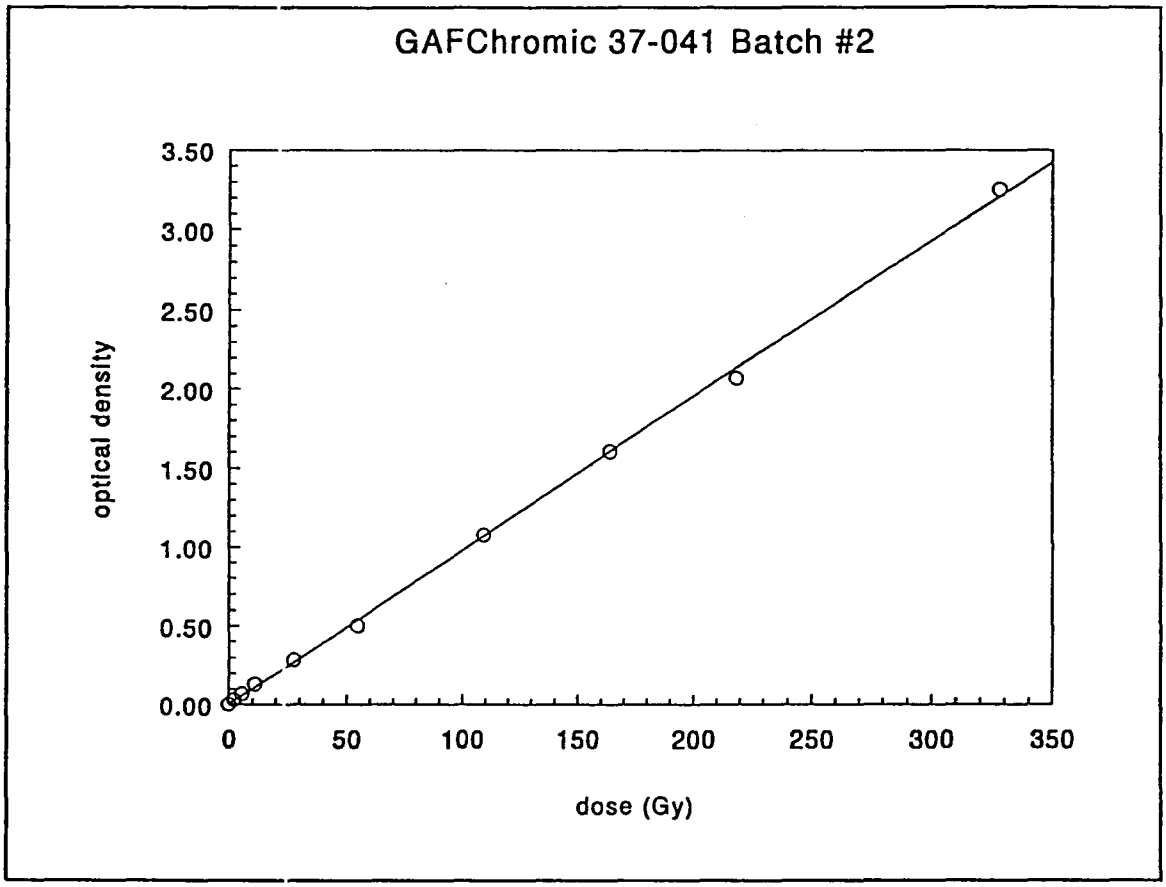

Figure 7.18: 6MeV electron calibration at d_{max} analyzed on the RIT113 scanning densitometer

optical density) of the film at a particular location i, and PV_0 is the nominal pixel value of an unirradiated film.

Response Function

In the course of optical density measurement of films irradiated in the water tank and backscatter experiments, scanning densitometer calibration on the RIT113 system was performed. A wedge-type graduated calibration filter (0.15OD to 2.86OD) was scanned on the system in order to determine true OD response. This calibration indicated that some drift had occurred, either in the photomultiplier tube or in the electronics, in the time since measurement of the calibration films (Ritt 1994). The effect of this drift was that a linear relationship could no longer be assumed to exist between measured optical density and dose. In order to compensate for drift, the following correction was made for the change in system response to optical density.

The ratio of true optical density OD_{true} to measured optical density OD_m was determined (Figure 7.19) and quadratic fit was performed on this data. This ratio, termed the response correction factor RCF, is given by:

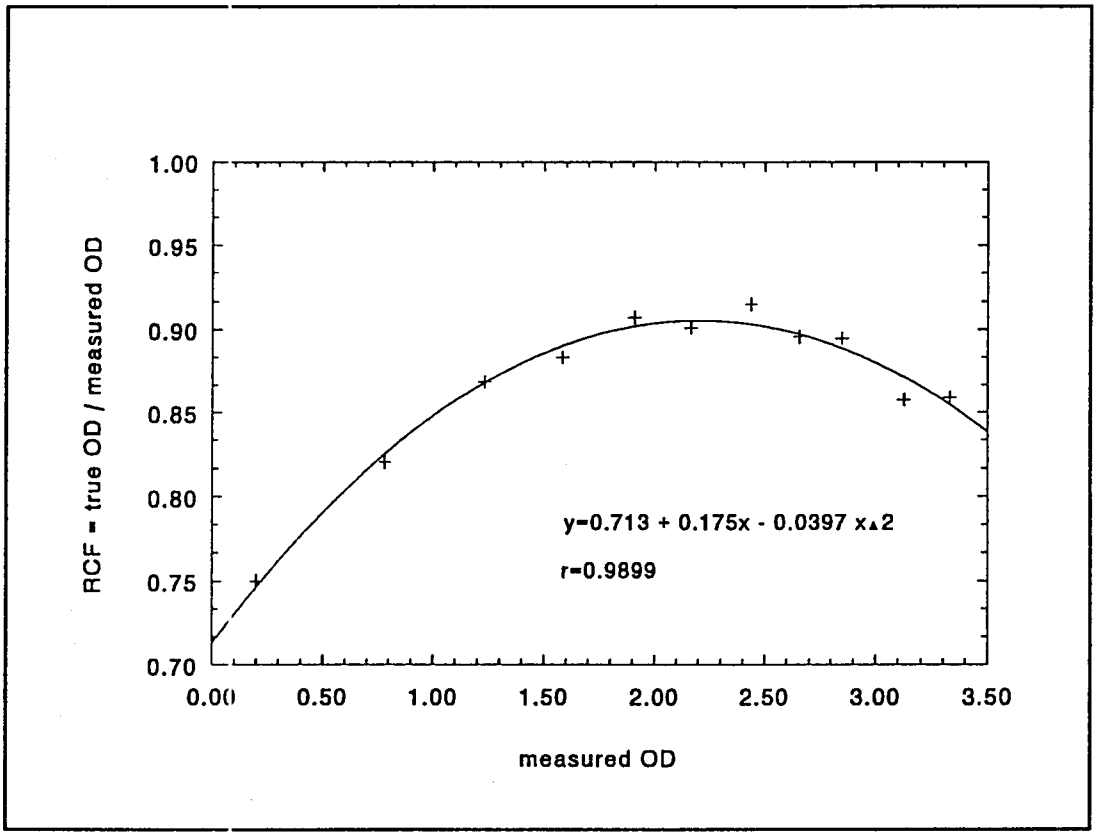

Figure 7.19: Response correction factor

$$OD_{true} = OD_m \times RCF(OD_m)$$

$$RCF(OD_m) = a_0 + a_1 \cdot OD_m + a_2 \cdot OD_m^2$$

Least-squares fitting yielded the following coefficients: $a_0 = 0.712 \pm 0.008$, $a_1 = 0.18 \pm 0.01$, $a_2 = -0.040 \pm 0.002$, and $r^2 = 0.977$.

The RCF was applied to all optical density measurements for films irradiated in the water tank and backscatter experiments.

Uncertainty Analysis

Based on the above calibration and correction, the dose D for a given pixel with uncorrected optical density x, where x = PV/1000, is given by:

$$D = x \cdot C_0 \cdot RCF(x) = x \cdot C_0 \cdot (a_0 + a_1 x + a_2 x^2)$$

Assuming the calibration function and response correction function are uncorrelated, the relative uncertainty in D is given by the following expression:

$$\frac{\Delta D}{D} = \sqrt{\left(\frac{\Delta C}{C}\right)^2 + \left(\frac{\Delta a_0}{a_0}\right)^2 + \left(2\frac{\Delta a_1}{a_1}x\right)^2 + \left(3\frac{\Delta a_2}{a_2}x^2\right)^2}$$

Evaluation of the above expression showed that $\Delta D/D$ was equal to $1.5\% \pm 0.1\%$ over the range of sensitivity encompassing all experimental

measurements ($0.1 < x < 3$). Since the uncertainty in dose is nearly constant, the uncertainty in relative dose, given by:

$$\frac{\Delta (D_1 / D_2)}{D_1 / D_2} = \sqrt{(\frac{\Delta D_1}{D_1})^2 + (\frac{\Delta D_2}{D_2})^2}$$

is approximately equal to $\sqrt{2} \bullet (\Delta D/D)$ or $2.1 \pm 0.1\%$ over the entire range of experimental data (approx. 2Gy-300Gy).

Data Extraction

The raw data files were received from Radiological Imaging Technologies Inc. via electronic mail. Each file was composed of a large 2-dimensional array of numbers, corresponding to the pixel values (optical density) of points physically separated by 100μm in each perpendicular dimension. The following methodology of data extraction was used.

A central block of data, 10 columns in width, was extracted along the length of the file and the mean and standard deviation of these 10 points were calculated. The upstream film edge was detected as the first non-zero value on the scan (since the net optical density of air relative to unexposed film is negative). The distance from the edge of the film was calculated as the

product of the step size and number of points from the edge. The stepping mechanism of the RIT113 scanner is a precision lead screw type, and the resulting precision in position is $\pm 25\mu m$ along its travel. Thus, the relative position of any point within a given film segment was known accurately to within a half-step, or $50\mu m$.

Uniformity

Figure 7.20 shows the optical density profile for a uniformly irradiated film. While the dose is nearly constant over the entire film, there is a marked decrease in the optical density measured near the film edges. From this, it can be seen that optical density read within a distance of roughly 0.5mm from the film edge is perturbed. For measurements beyond 2mm from the edges, however, the standard error in optical density (and hence, dose) was observed to be less than 1% within a single film and also within 1% for replicate films over the entire set of calibration films (2Gy-300Gy).

Fold Artifact

A plot of the OD scan of an unirradiated film which was placed in the phantom, folded, and then unfolded prior to scanning (Figure 7.21) shows the peak artifact (at $\sim$1.5cm from the upper film edge) introduced by the folding of the film. The artifact is due to opacity introduced through plastic deformation of the film along the fold line. The peaks present at the edges are

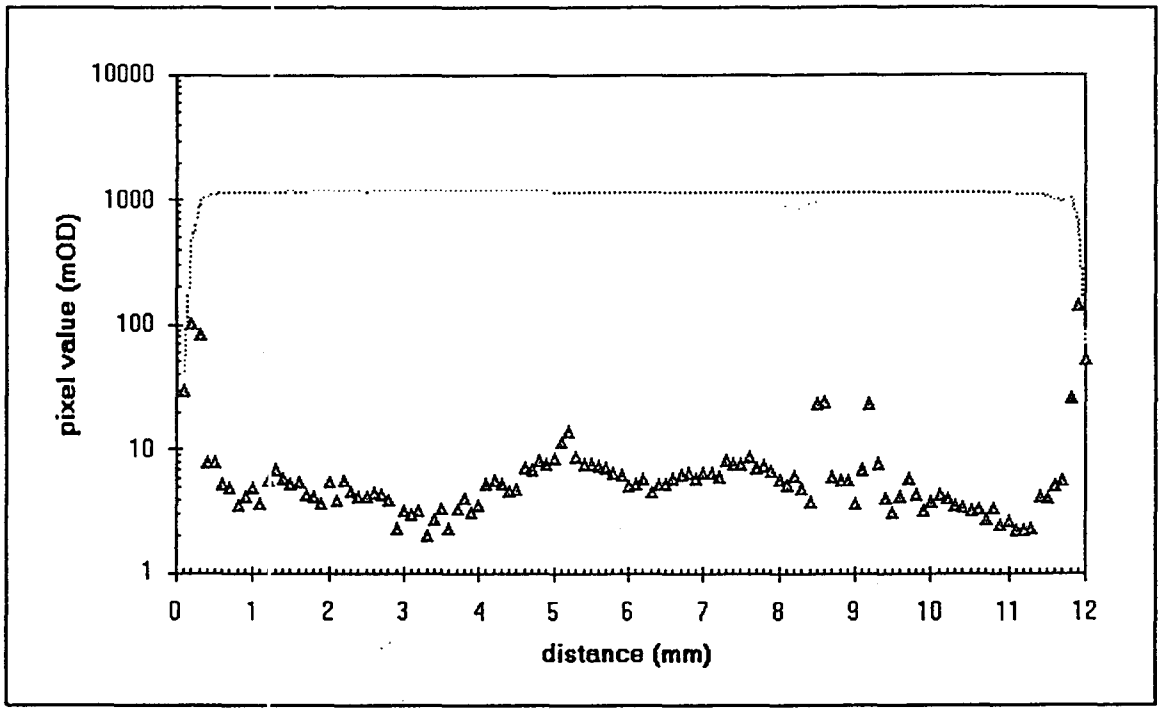

Figure 7.20: Optical density profile of a uniformly irradiated film (109Gy) showing uniformity and edge artifact. (□) indicate standard error at each measurement

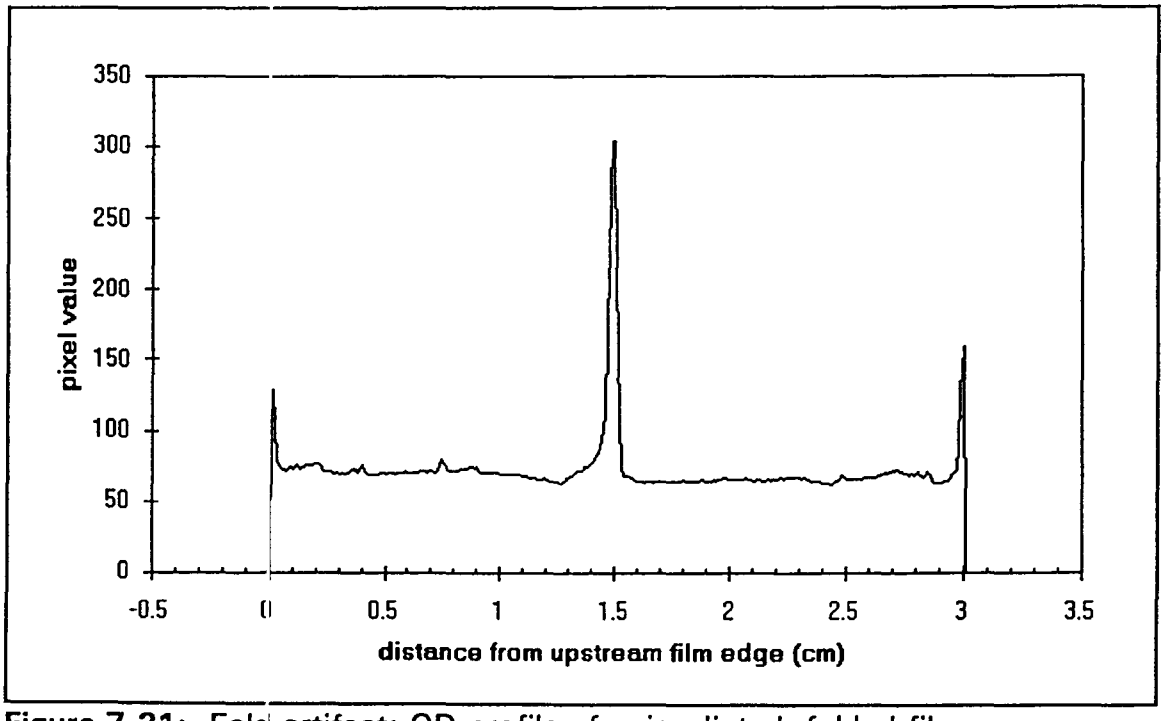

Figure 7.21: Fold artifact; OD profile of unirradiated, folded film

due to film deformation at cutting (outer peaks were masked on films which received doses in excess of 2Gy). It can be seen that the useful portion of the film (that within the phantom) is not appreciably affected by the folding and unfolding of the film. The peak, however, was observed on the irradiated films to be bracketed by regions of low optical density. Optical density data for the region within 200-500μm of the interface was perturbed due to the fold artifact and was subsequently excluded from the analysis (Section 7.5.4) for all folded films.

7.4.2 Determination of the Energy Dependence of GAFChromic Films

Figure 7.22 shows the measured 6MeV electron depth-dose distributions recovered from radiochromic film exposure and from diode detector measurements in the water tank. The latter were corrected according to the TG21 protocol (Schulz 1983). The relative energy sensitivity $\zeta(x)$ (as defined in Section 5.2.2) derived from this data is shown in Figure 7.23. From this figure, it can be seen that the variance between the two sets of measurements is less than $\pm 5\%$ for all data points corresponding to depths of up to 2.6 cm. Since the doses recorded by the film were very low ($<<2$Gy) in the remaining region, it was impossible to conclude from this data whether the apparent decrease in sensitivity was due to energy response, or due to inaccuracy of using the film and system below their minimum sensitivity. Subsequent analysis for the backscatter experiments assumed no inherent energy dependence on film sensitivity to depths of 2.95cm in polystyrene.

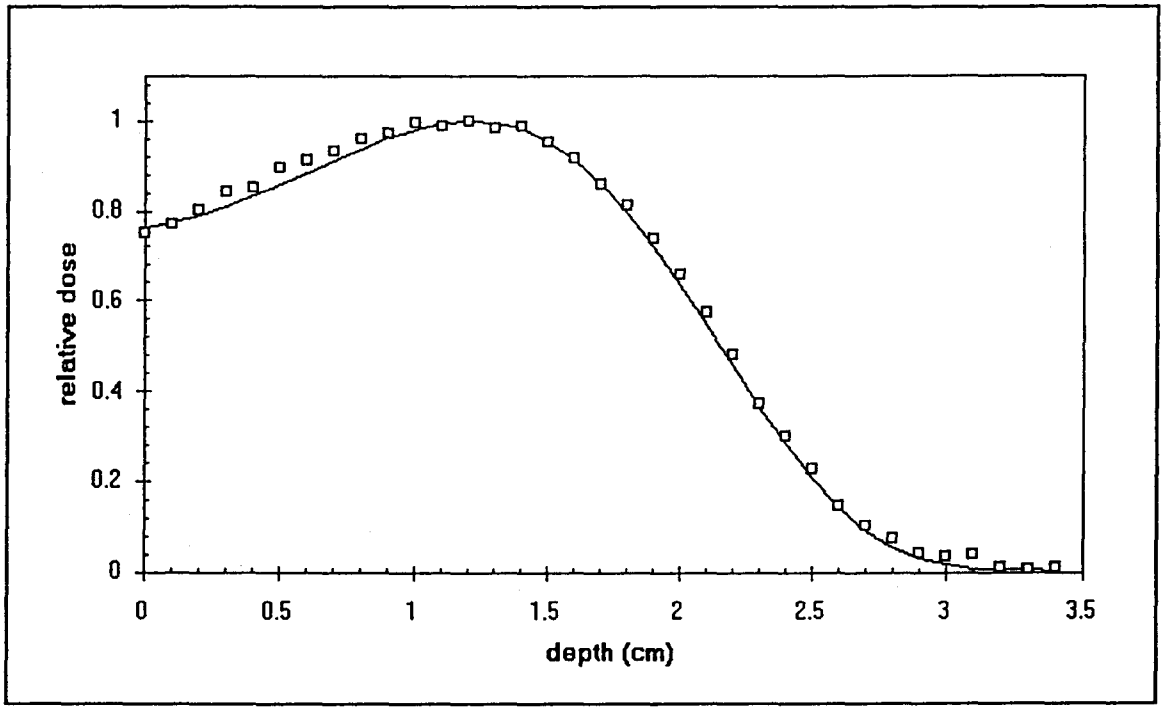

Figure 7.22: Radiochromic film (line) and diode detector (□) measured depth-dose in water. Nominal dose at d_{max} is approximately 20Gy

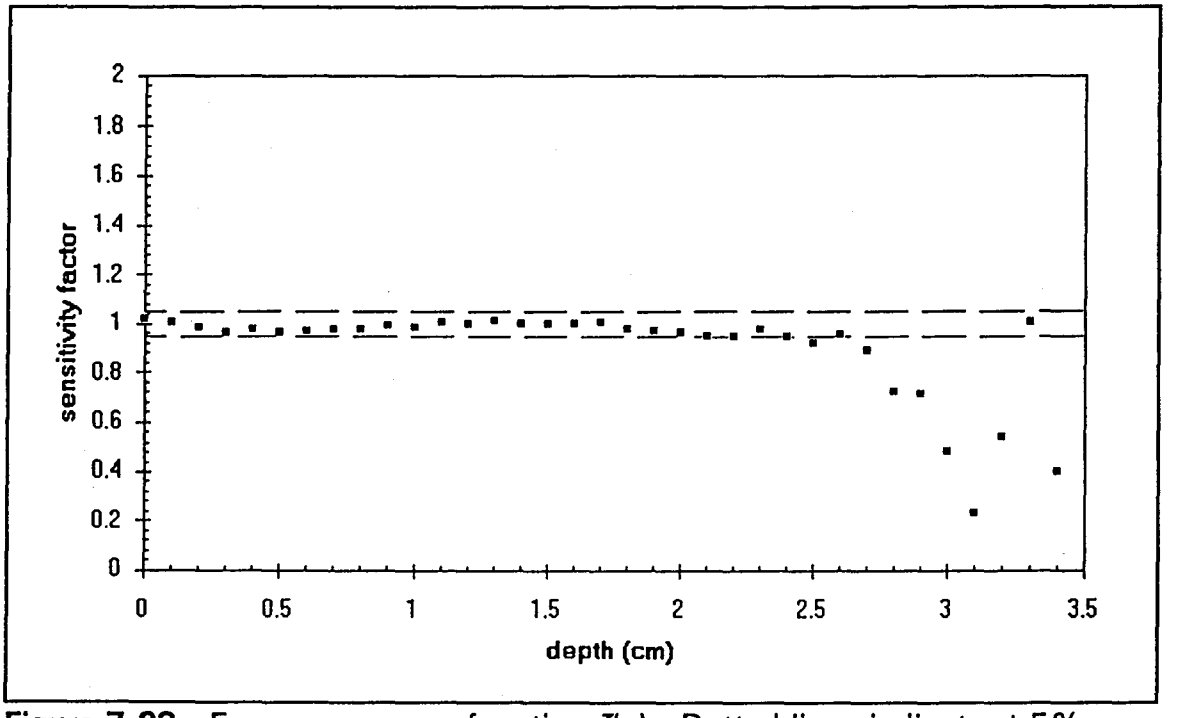

Figure 7.23: Energy response function $\zeta(x)$. Dotted lines indicate $\pm 5\%$

7.5 Backscatter Experiments

The dose enhancement ratio DER(x') and backscatter factor B(x') were calculated from the Monte Carlo data and the experimental strip films for each of the five geometries and three depths of interface. The coordinate system x' was taken as the axial distance (in g/cm^2) upstream from the interface (x'=0) in the polystyrene phantom. In addition, DER(0) and B(0) were determined for each case from the spot film measurements, for which spot films were placed directly at the interface, perpendicular to the beam central axis.

7.5.1 Data Analysis

Monte Carlo Output

Each energy deposition data point in a dose scoring region was assigned a numerical index i such that i=0 corresponded to the dose scoring region adjacent to the interface. x_i' was taken at the centre of each dose scoring region, all of which were 0.1mm in width. Thus:

$$x_i'(g/cm^2) = \rho \times (i \times 10^{-2} + \frac{10^{-2}}{2})$$

where $\rho = 1.045$ g/cm^2 is the density of polystyrene. The dose per unit fluence $D_j(x_i')$ and dose enhancement factors for scatterer j are given by:

$$D_j(x_i') = D_{i,j}$$
$$DER_j(x_i') = 1 + B_j(x_i') = \frac{D_j(x_i')}{D_0(x_i')}$$

where $D_0(x_i')$ is the dose for the homogeneous case. The relative uncertainty in DER(x') was determined as the square root of the sum of the squares of the relative uncertainties predicted by the Monte Carlo code for energy deposition in the corresponding subzones.

It was discovered that the uncertainty estimate for energy deposition, which is expressed as percentage error to one significant figure in the TIGER output, is formatted through truncation rather than rounding (Prestwich 1994). That is, errors in the range of 1.00 to 1.99 are shown as "1". To compensate, each output percent error was incremented by 0.5% in order to obtain a realistic estimate of the true error.

Spot Films

The average pixel value for each spot film was provided by Radiological Imaging Technologies using the following methodology. For each film, a central region of interest (2mm away from the film edge) was selected. A median test was applied to remove points corresponding to film defects (i.e. dust, scratches), and the pixel values of all remaining points within the region of interest were subsequently averaged. The average pixel value for each film was then corrected for system response using the RCF function (Section 7.4) to determine true optical density. Dose enhancement ratios were determined as the ratio of optical densities of the heterogeneous and corresponding homogeneous spot films.

Strip Films

Analysis of the strip films involved the following steps:

1. Extraction of PV_i data along a central band of the film and determination of mean and standard deviation at each depth (Section 7.4.1)
2. Location of fold artifact (solid backscatterer) or proximal edge (air-polystyrene films) and imposition of the x′ coordinate system
3. Correction for system response (RCF function) and subtraction of background to determine the net optical density profile $OD_0(x')$ and $OD_j(x')$ for each film

4. Determination of DER(x') and B(x')

The ratio of the dose received by a strip film used in the heterogenous geometry at a particular depth to that of the corresponding location in the homogeneous case was used to determine DER(x') and B(x'). Although the step size of the RIT113 scanner corresponded to the width of the dose scoring regions in the Monte Carlo simulations, the films were held at an angle of 10° to normal in the measurement phantom. Therefore, the effective step size relative to the beam central axis in the experiments was $\Delta x' = 100\rho \cdot \cos(10°)$ or 10.29mg/cm^2. In analyzing these films there was the added complication that the location of the interface ($x' = 0$) had to be determined for each film. Alignment of film data was accomplished by making use of the fold artifact.

The characteristic spike of the fold artifact was found relatively easily on each film with the noted exception of the air-polystyrene films (which were not folded). A plot of the depth-dose profiles determined for the films used in the homogeneous geometry for each of the three interface depths (Figure 7.24) shows the position and magnitude of the fold artifacts. In the coordinate system used, the abscissa corresponds to the distance upstream from the distal film edge in terms of the number of steps. Given the step size (100μm), the orientation of the film, and the thickness of the measurement phantom, the point corresponding to $x' = 0$ was determined. This position was nominally

located at 4 ± 1 step from the peak of the fold artifact for these three films. Thus, the fold artifact peak was taken as $x' = -4 \cdot 10^{-2} \cdot \cos(10°) \cdot \rho$ or $-41.3 mg/cm^2$.

The fold artifact was used as a reference point for the x′ coordinate system for all films for which a solid backscatterer was present. Figure 7.25 shows the normalized depth-dose profiles from the same three homogeneous strip films depicted in Figure 7.24, aligned using the fold artifact. The coordinate system used corresponds to depth along the beam central axis such that $x = 0$ is at the surface of the phantom. The excellent agreement between dose measurements on different films at the same depth can be seen particularly in films at depths R_{20} and R_5, and the relative positions of the fold peak and true interface location can be seen. For the air-polystyrene films, the origin of x′ was calculated based on the distance from the proximal (upstream) edge of the film.

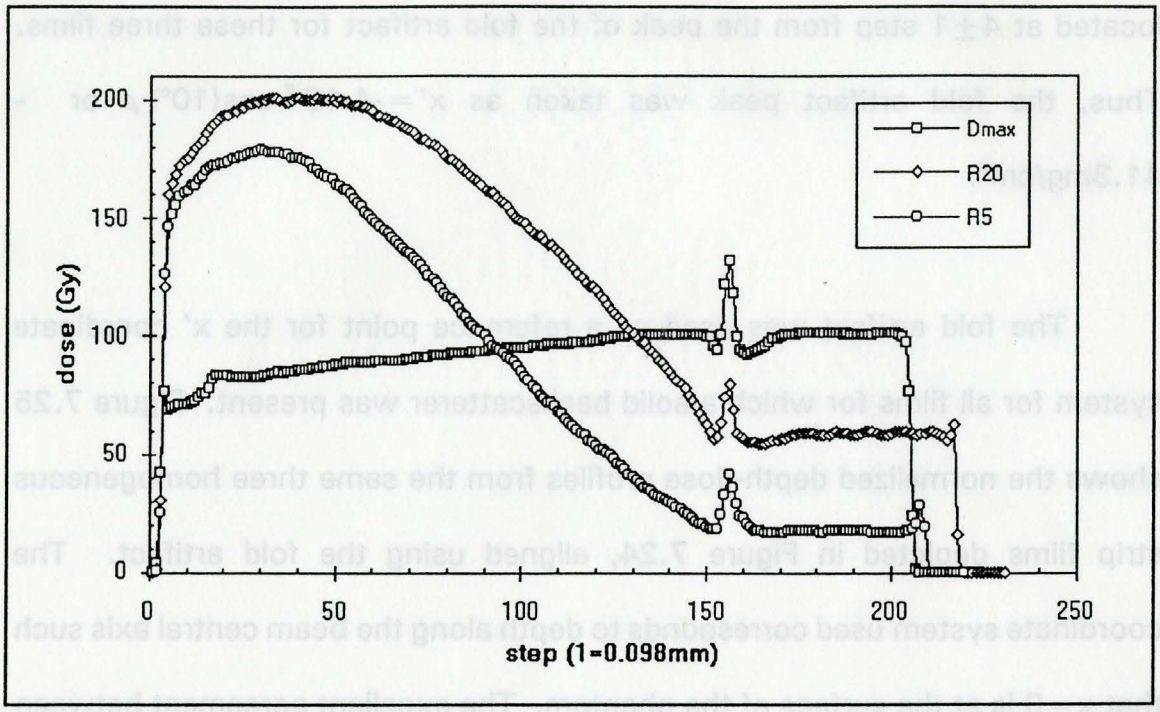

Figure 7.24: Homogeneous films at d_{max}, R_{20}, and R_5, showing fold artifact spikes

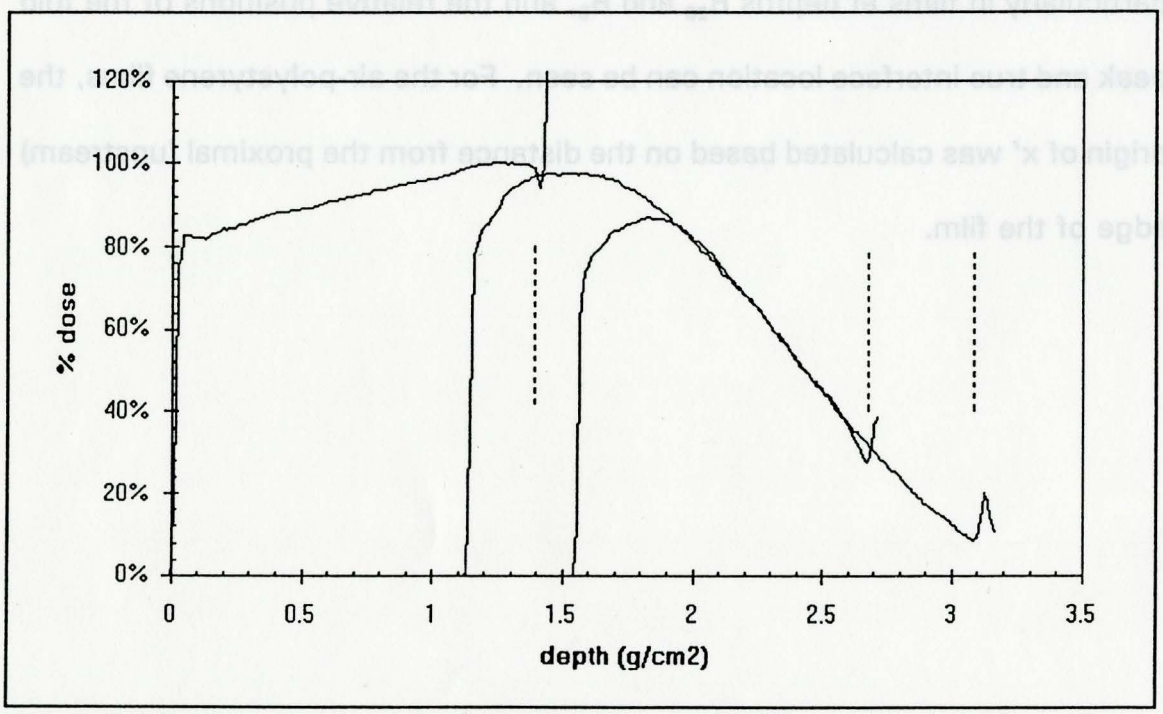

Figure 7.25: Alignment of the homogeneous strip films using the fold artifact. Interface locations are shown as vertical bars (dotted).

7.5.2 Characterization of Backscatter

From preliminary analysis of the Monte Carlo data, it was observed that a single exponential function provided good fit to the backscatter DER(x') data in most cases. Previous studies with isotropic β-sources and slab geometry (Nunes 1991) have used both single and double exponential relationships to characterize the backscatter factor. Fitting of double exponential functions to the data in this work provided no significant increase in correlation for all geometries used. Thus, single exponential least-squares fitting was performed exclusively for all data.

Equations of the following form were fitted to the DER(x') data from the Monte Carlo simulations and strip film measurements:

$$DER(x') = 1 + a_0 + a_1 e^{-x'/x_0}$$

The factor a_0 was put equal to 0 for the Monte Carlo data and equal to 0.00 ± 0.03 for the strip film measurements. The variation in the latter can be explained by random variation in the dose received during each irradiation, and the introduction of a_0 was a means to reduce the associated error. The parameter x_0 is defined as the relaxation length. In order to characterize B(x'),

the experimental data was shifted by a_0 as determined above prior to subtraction of unity:

$$B(x') = DER(x') - a_0 - 1$$

Thus, this process results in the following fit for B(x'):

$$B(x') = B(0)\, e^{-x'/x_0}$$

where B(0) is the estimate of the backscatter factor at the interface.

7.5.3 Point Measurements of B(0) from TIGER and Spot Film Results

Table 7.5 shows a comparison of the backscatter factors determined by spot film measurements and those predicted by the Monte Carlo simulations for the 0.1mm polystyrene region immediately adjacent to the interface. In this table, Δ represents the difference between monte carlo predicted and experimentally determined backscatter factors in terms of the number of standard deviations:

$$\Delta = \frac{B_{tiger} - B_{spot}}{\sqrt{\sigma^2_{tiger} + \sigma^2_{spot}}}$$

Thus, experimental spot film results and Monte Carlo predictions show agreement within one standard deviation (σ) in the backscatter factors for the

4 scatters at each of the 4 interface depths, with the exceptions of air at d_{max} and bismuth at R_5 which showed agreement at 2σ. In addition, a χ^2 test showed no significant variation between experiment and simulation data.

Table 7.5: Backscatter Factor at interface B(0) from spot film measurements and Monte Carlo calculations

Interface Location	Scatterer	TIGER mean ± S.D.		Spot Film mean ± S.D.		Δ (S.D.)
d_{max}	Air	-0.16	0.03	-0.21	0.03	1.4
	B.E.P.†	0.10	0.05	0.09	0.02	0.2
	Copper	0.37	0.05	0.36	0.03	0.2
	Bismuth	0.68	0.07	0.75	0.04	-1.0
R_{20}	Air	-0.12	0.03	-0.10	0.02	-0.7
	B.E.P.	0.10	0.02	0.12	0.02	0.9
	Copper	0.36	0.04	0.32	0.03	0.9
	Bismuth	0.71	0.03	0.68	0.04	0.7
R_5	Air	-0.08	0.07	-0.02	0.02	-0.9
	B.E.P.	0.24	0.07	0.22	0.03	-0.7
	Copper	0.43	0.09	0.35	0.03	-0.9
	Bismuth	0.92	0.11	0.78	0.04	1.3
				χ^2_{11}		9.15
				significance: $0.25 < p < 0.50$		

† Cortical bone equivalent plastic

7.5.4 Spatial Distribution of Backscatter B(x): TIGER and Strip Film Results

Figures 7.26 through 7.37 show the backscatter factor, as a function of mass-distance from the interface (upstream) within the measurement phantom, for each of the three interface locations and four heterogeneous scatterers. Experimental results (+) and Monte Carlo predictions (O) are compared in each plot and a single exponential fit to each is indicated as a solid line. Since the perturbation caused by the fold artifact was seen to affect the first 3-5 data points for each measurement, weights of zero were assigned to these points in the course of fitting. Spot film values were included with the strip film data as the first point, at a nominal depth of 50μm, prior to fitting. This point, and all remaining points, were assigned equal weight in the fitting, while excluded points received a weight of zero. Summaries of the estimates for the backscatter factor B and relaxation length x_0 obtained through the fitting process are presented in Tables 7.6 and 7.7, respectively.

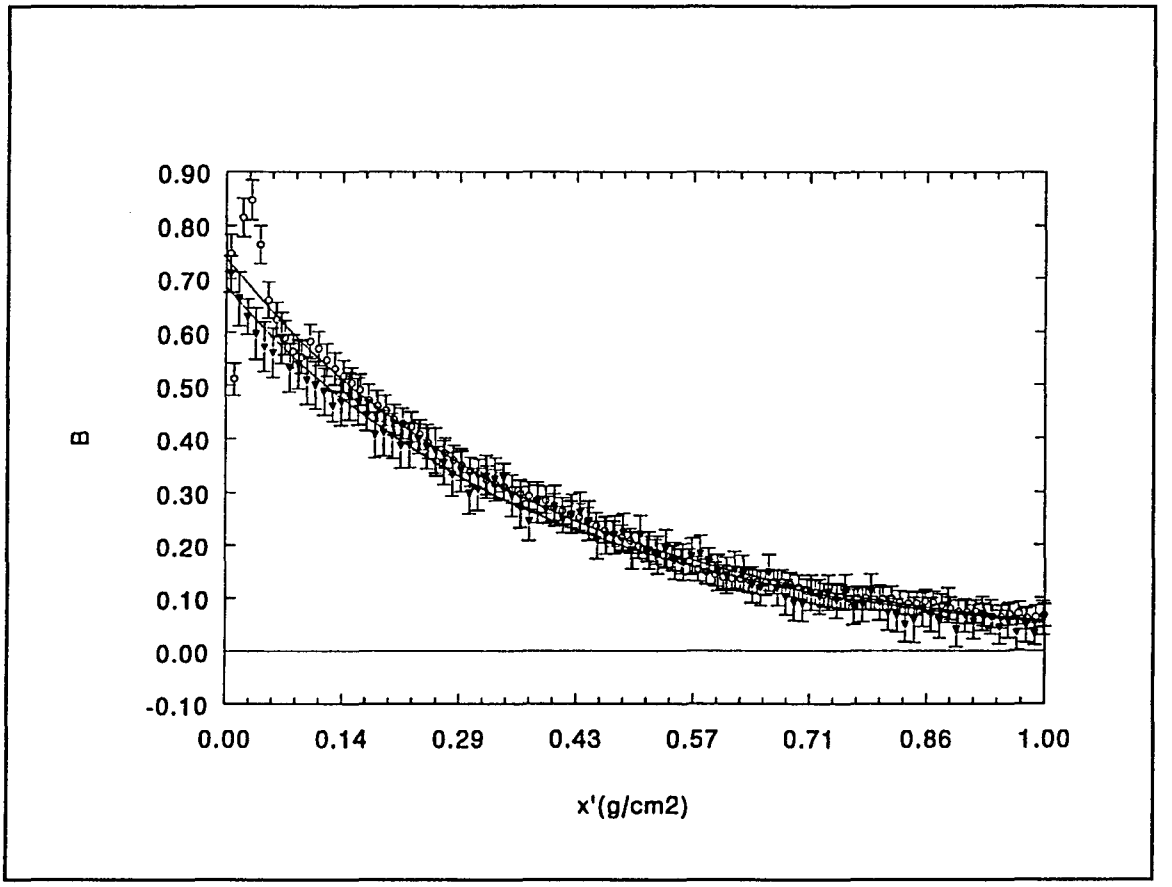

Figure 7.26: B(x′) for bismuth at d_{max}, strip film measurements (+) and TIGER simulation (○).

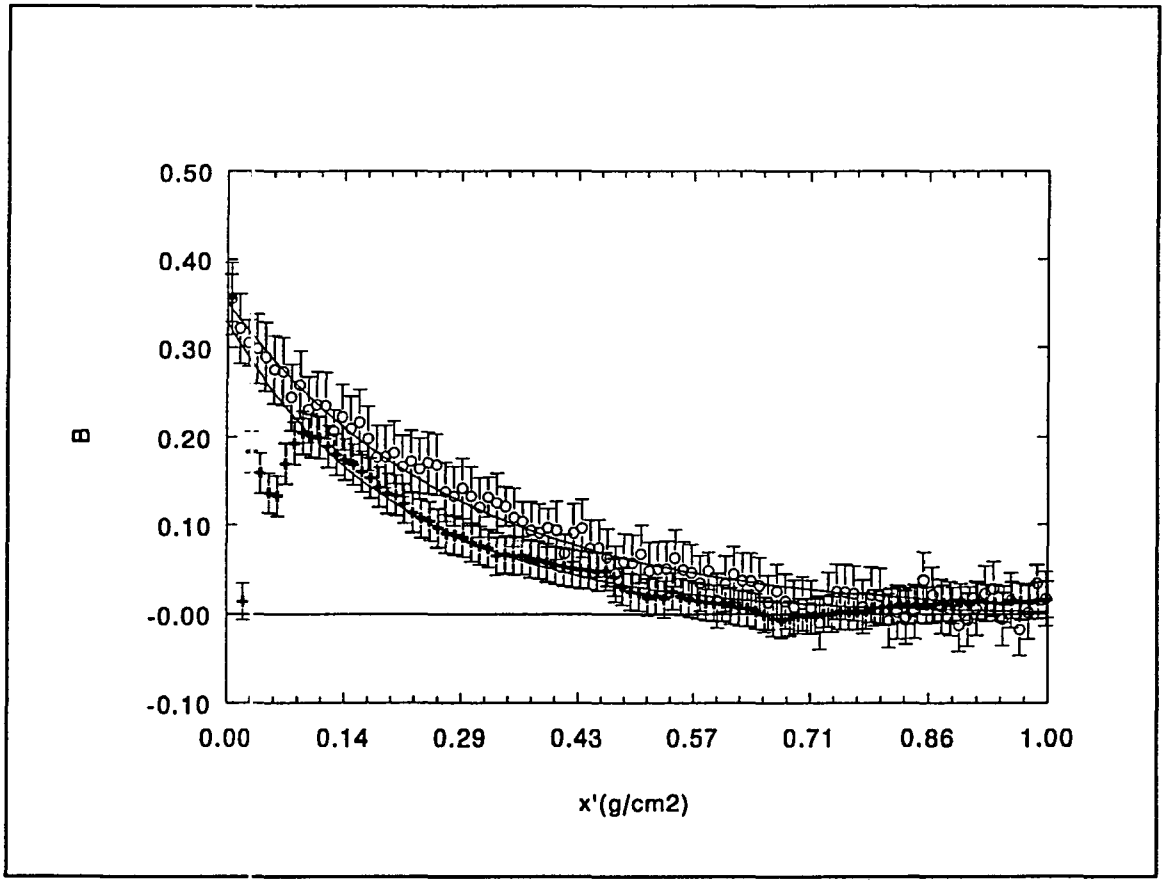

Figure 7.27: B(x') for copper at d_{max}, strip film measurements (+) and TIGER simulation (○).

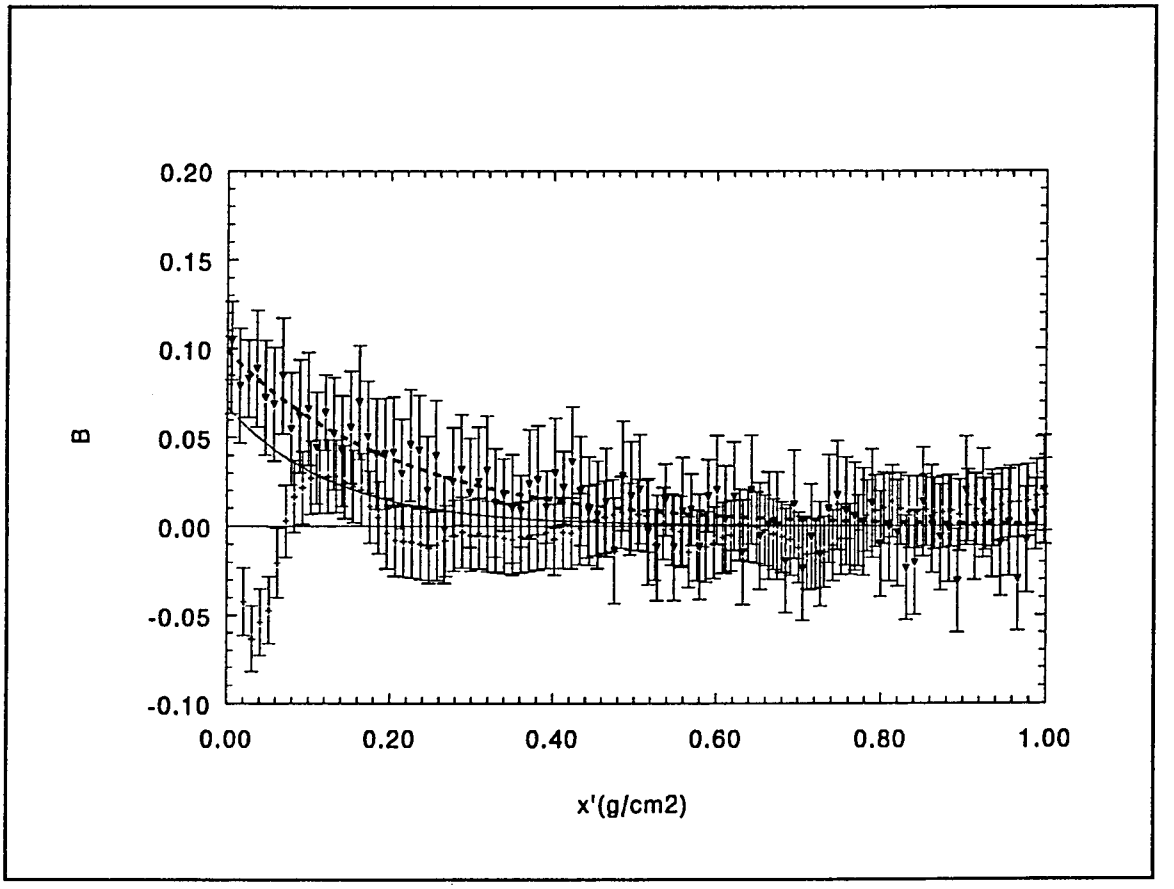

Figure 7.28: B(x') for bone-equivalent plastic at d_{max}, strip film measurements (+) and TIGER simulation (○).

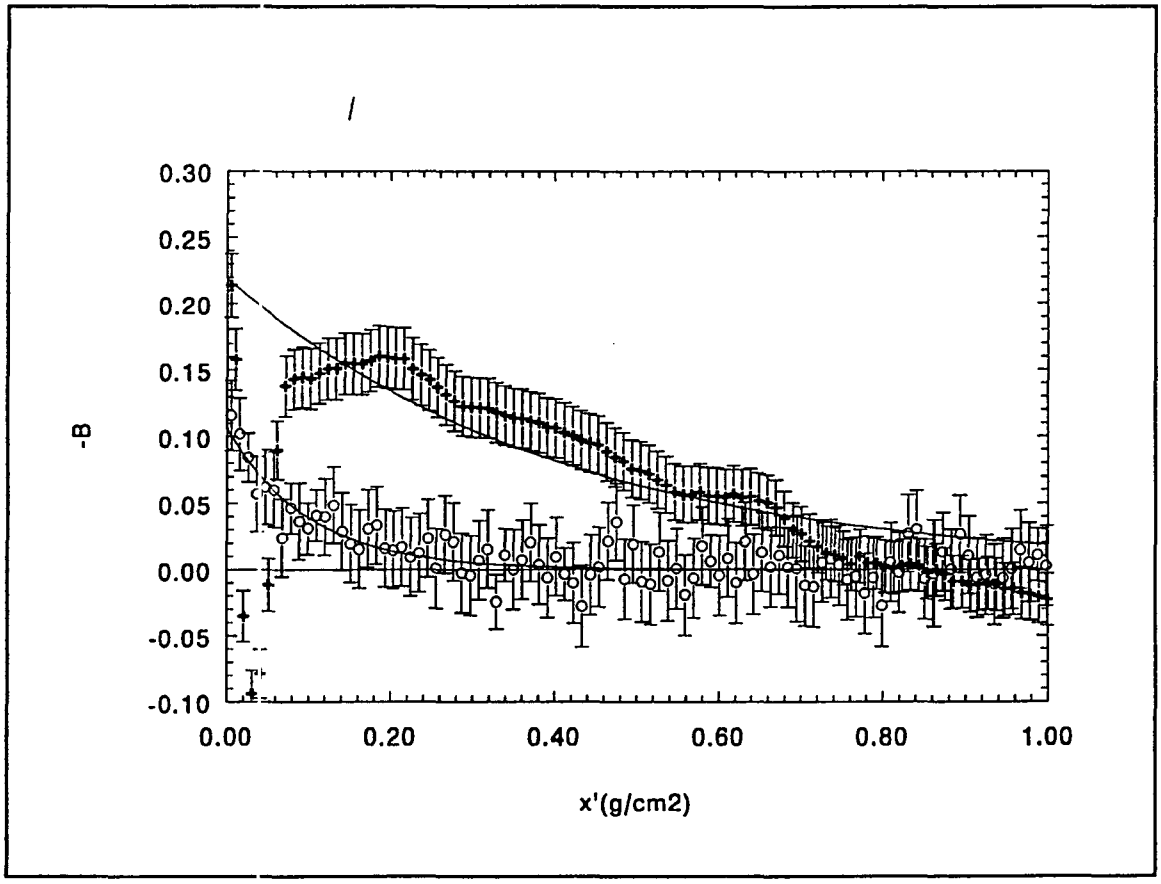

Figure 7.29: B(x') for air at d_{max}, strip film measurements (+) and TIGER simulation (○).

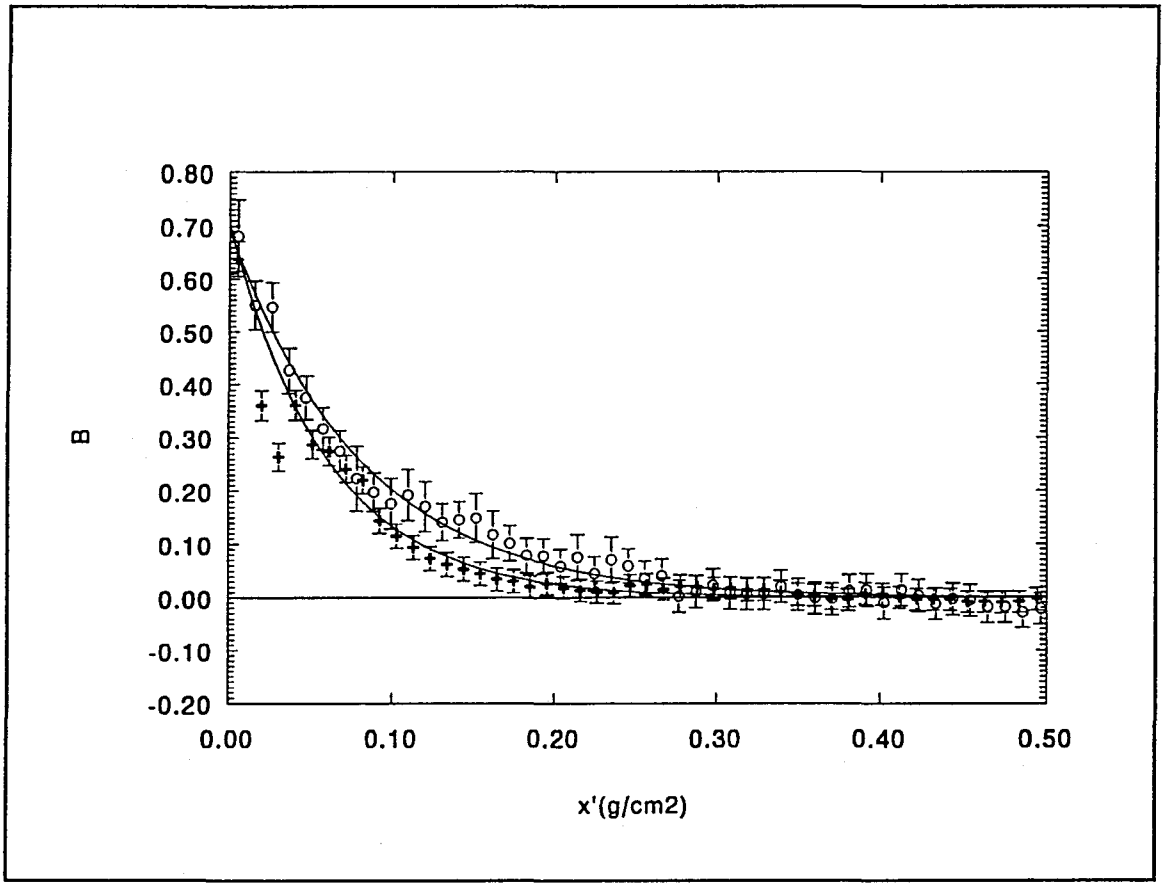

Figure 7.30: B(x') for bismuth at R_{20}, strip film measurements (+) and TIGER simulation (○).

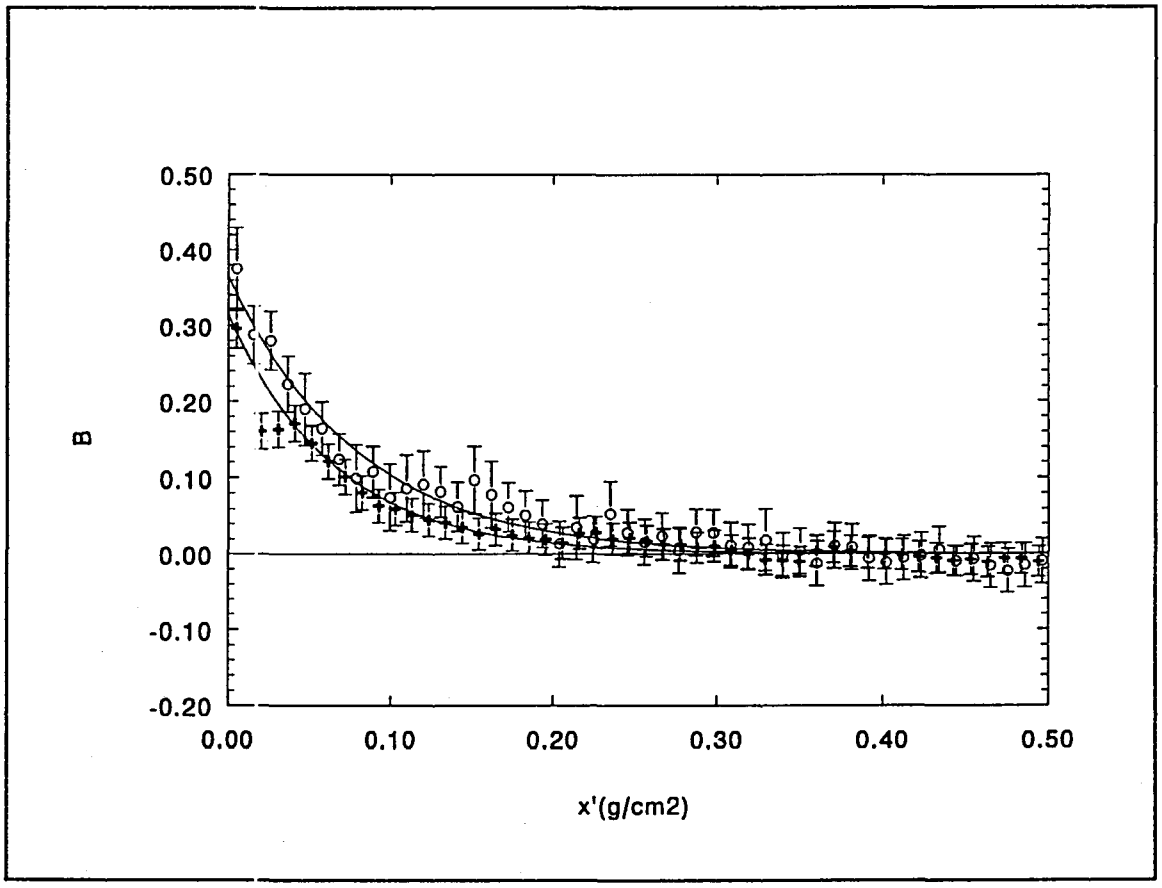

Figure 7.31: B(x') for copper at R_{20}, strip film measurements (+) and TIGER simulation (○).

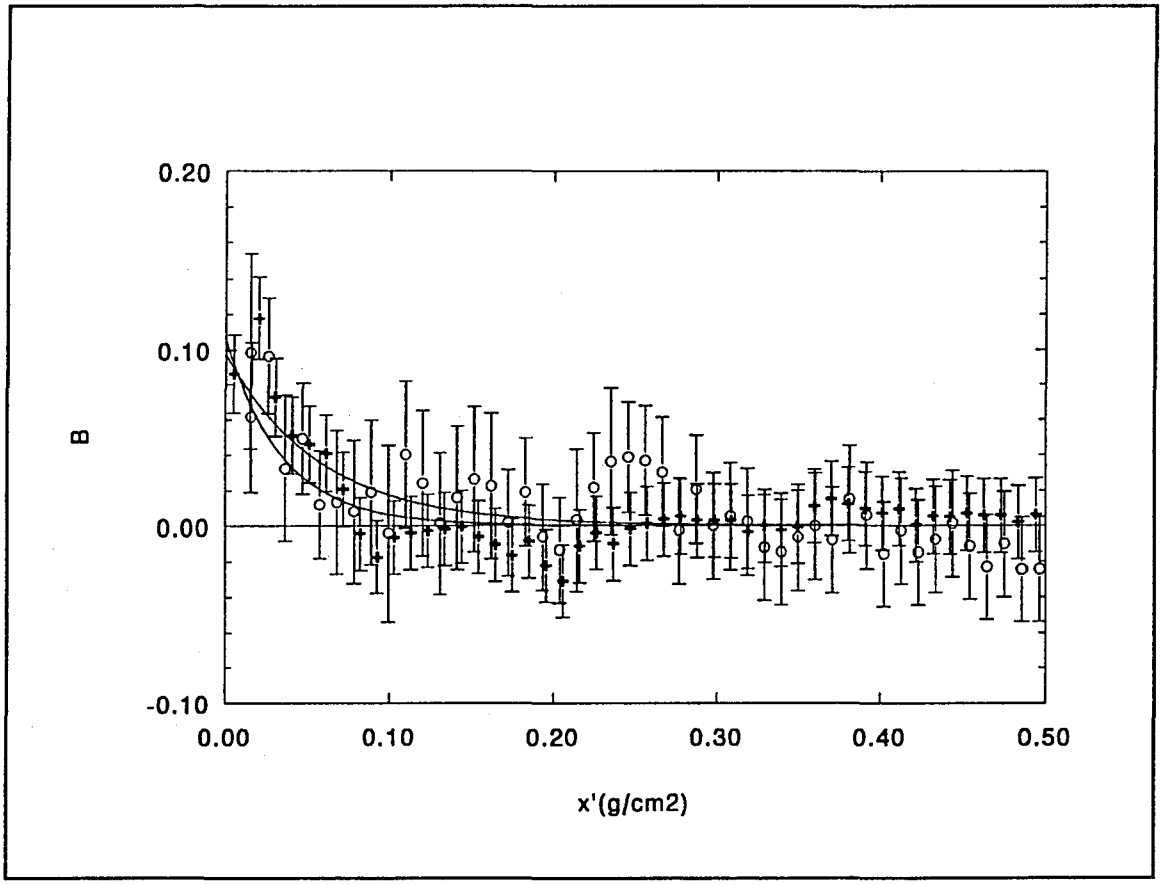

Figure 7.32: B(x') for bone-equivalent plastic at R_{20}, strip film measurements (+) and TIGER simulation (O)

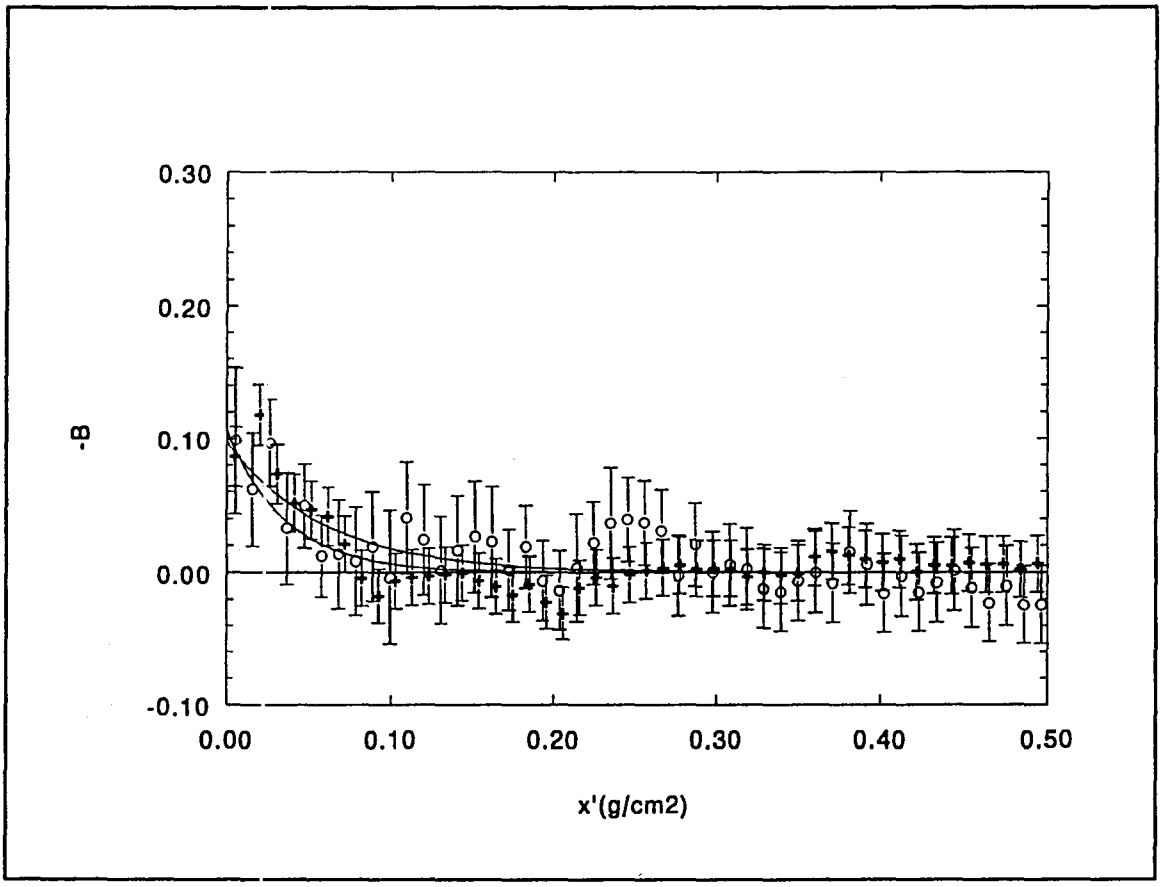

Figure 7.33: B(x') for air at R_{20}, strip film measurements (+) and TIGER simulation (○).

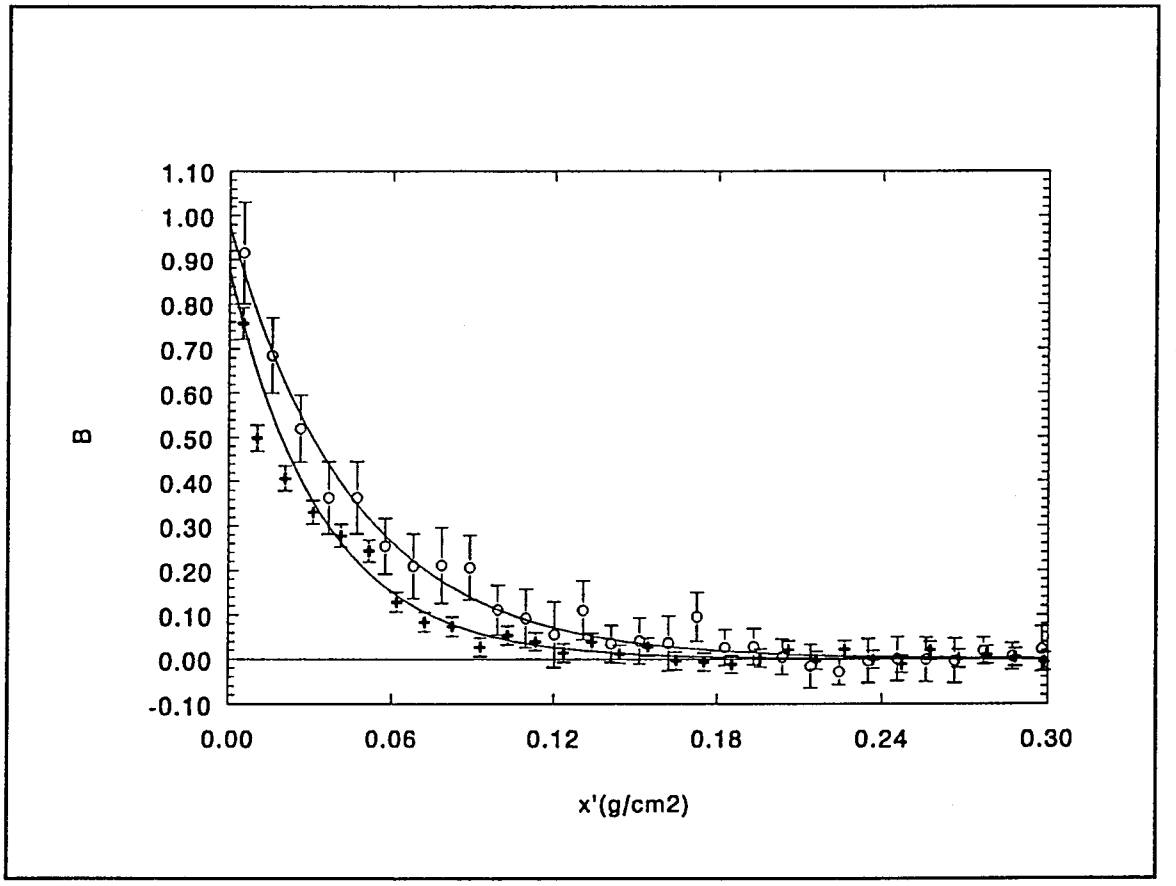

Figure 7.34: B(x') for bismuth at R_5, strip film measurements (+) and TIGER simulation (○).

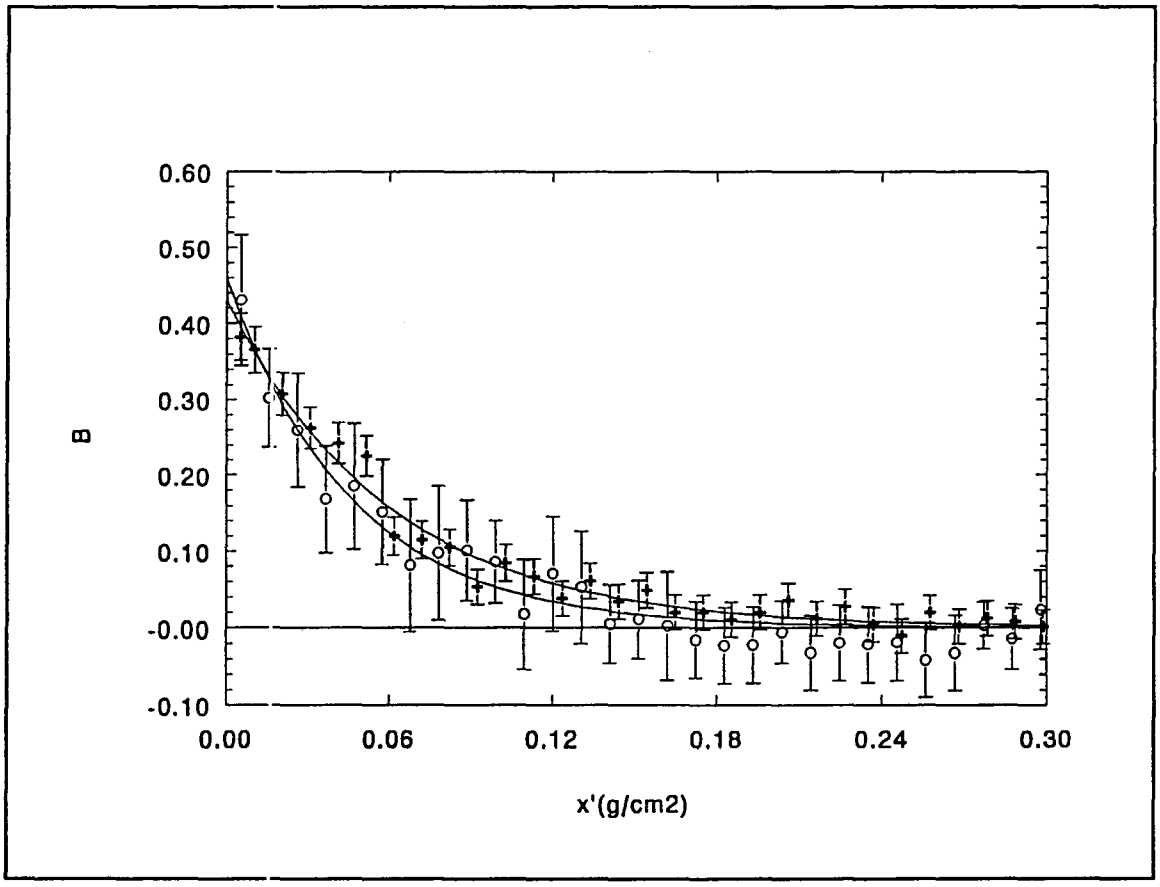

Figure 7.35: B(x') for copper at R_5, strip film measurements (+) and TIGER simulation (○).

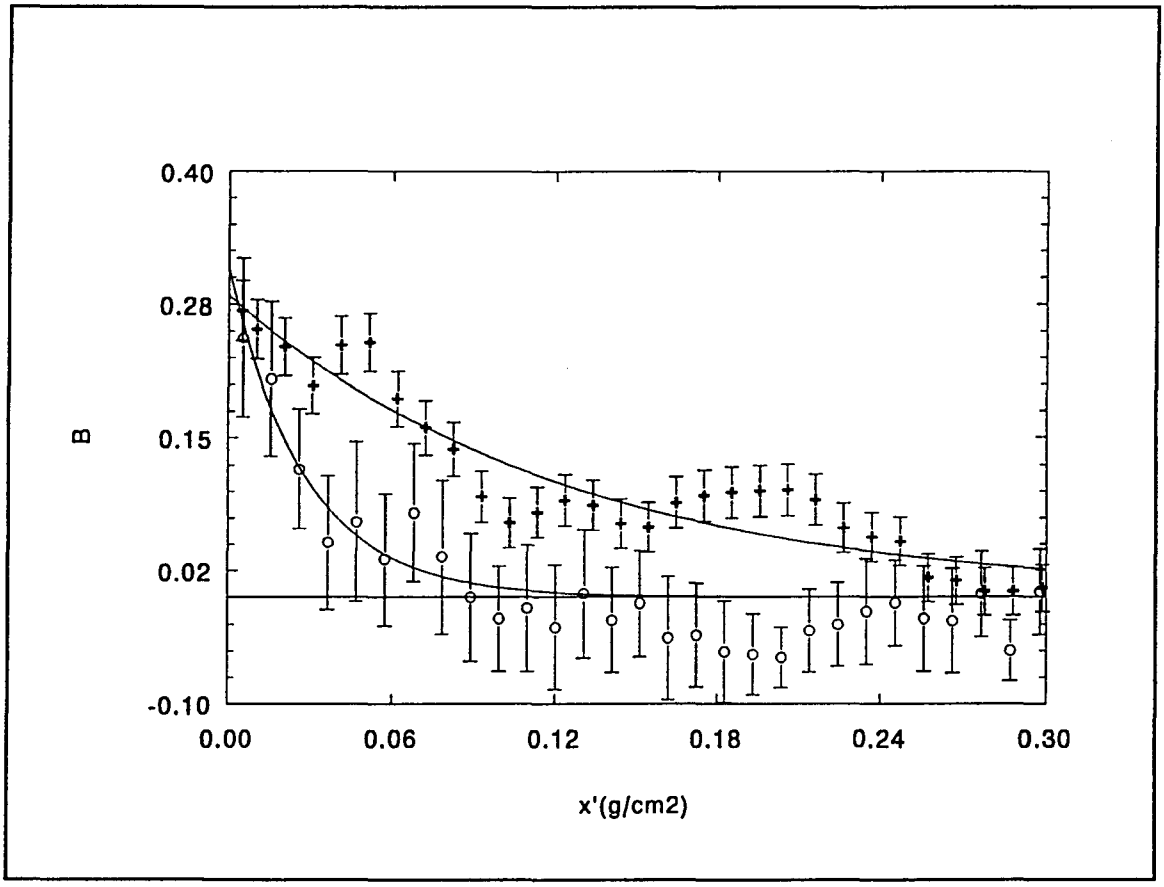

Figure 7.36: B(x') for bone-equivalent plastic at R_5, strip film measurements (+) and TIGER simulation (○).

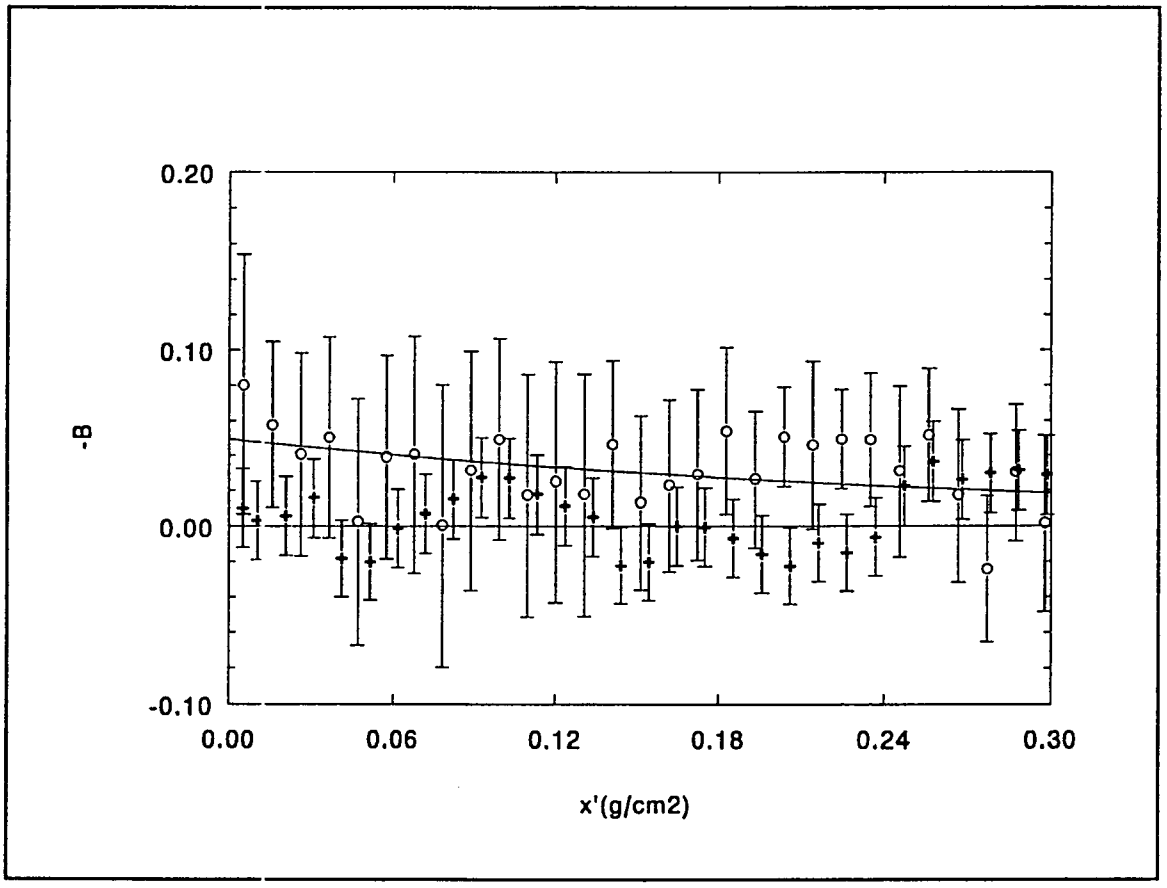

Figure 7.37: B(x′) for air at R_5, strip film measurements (+) and TIGER simulation (○).

Table 7.6: Backscatter factors B(0) from single exponential fitting of strip film and Monte Carlo results

Interface Location	Scatter-er	TIGER			Strip Films			
		mean	S.D.	$r^{2\,\dagger}$	mean	S.D.	r^2	Δ (S.D.)
d_{max}	Air	-0.106	0.009	0.63	-0.219	0.008	0.83	9.4
	BEP	0.099	0.006	0.74	0.0763	0.009	0.54	2.1
	Copper	0.351	0.006	0.97	0.328	0.006	0.97	2.7
	Bismuth	0.684	0.007	0.99	0.738	0.004	0.99	-7.7
R_{20}	Air	-0.16	0.02	0.69	-0.163	0.008	0.89	-0.14
	BEP	0.1	0.01	0.53	0.11	0.01	0.60	-0.71
	Copper	0.36	0.01	0.96	0.315	0.008	0.98	3.5
	Bismuth	0.69	0.01	0.98	0.7	0.01	0.99	-0.71
R_5	Air	-0.049	0.006	0.40	0	0.0001	0.20	-8.2
	BEP	0.31	0.02	0.77	0.28	0.03	0.79	-0.83
	Copper	0.46	0.02	0.93	0.43	0.02	0.96	1.1
	Bismuth	0.98	0.02	0.98	0.87	0.02	0.99	3.9
						χ^2_{11}		242
						significance $p << 0.005$		

† degrees of freedom adjusted coefficient of determination

Table 7.7: Relaxation lengths x_0 from single exponential fitting of strip film and Monte Carlo results

Interface Location	Scatter-er	TIGER			Strip Films			
		mean	S.D.	r^2	mean	S.D.	r^2	Δ (S.D.)
d_{max}	Air	0.10	0.01	0.63	0.4	0.02	0.83	-13
	BEP	0.21	0.02	0.74	0.06	0.01	0.54	6.7
	Copper	0.28	0.07	0.97	0.207	0.007	0.97	1.0
	Bismuth	0.39	0.01	0.99	0.389	0.006	0.99	0.09
R_{20}	Air	0.04	0.006	0.69	0.24	0.04	0.90	-4.9
	BEP	0.06	0.01	0.53	0.035	0.007	0.60	2.0
	Copper	0.079	0.003	0.96	0.065	0.002	0.98	3.9
	Bismuth	0.081	0.002	0.98	0.057	0.002	0.99	8.5
R_5	Air	0.30	0.05	0.40	0.06	0.13	0.20	1.7
	BEP	0.028	0.003	0.77	0.12	0.04	0.79	-2.3
	Copper	0.046	0.003	0.93	0.065	0.005	0.96	3.3
	Bismuth	0.046	0.001	0.98	0.037	0.001	0.99	6.4
						χ^2_{11}		401
						significance $p << 0.005$		

Good general agreement between the experimental results and Monte Carlo simulations for the majority of geometries can be seen on the preceding figures. From Table 7.6, it can be seen that the incorporation of many data points offers greater precision for the predicted backscatter values over the single point measurements (Table 7.5).

Significant differences were found between the backscatter factors derived from the experimental results and those from the Monte Carlo simulations for the following cases:

- •Air: d_{max} and R_5
- •B.E.P. none
- •Bismuth: d_{max} and R_5
- •Copper: d_{max} and R_{20}

With respect to the fitted relaxation lengths, agreement between the two data sets is relatively poor. Agreement within one standard deviation σ was found for both Copper and Bismuth at d_{max}. In addition, B.E.P at R_{20} and air and R_5 showed agreement at 2σ. For the latter, the apparent agreement can be attributed to the large error associated with the experimentally determined value (>200%), due to poor correlation.

7.5.5 Application of Empirical Backscatter Relationships

The variation of the backscatter factor with the empirical backscatter relationships described in Section 2.5 are plotted in Figures 7.39 and 7.40. A function of the form $y = k \bullet (g - g_0)$ was fitted to data for each depth to test the applicability of these relationships. In this analysis, g and g_0 were the empirical expressions for the heterogeneous scatterers and for polystyrene, respectively. Proportionality constants k for each fit are shown in Table 7.8. Since the conditions of semi-infinite lateral geometry were not maintained for air, backscatter factors obtained from air interface data have been excluded from this analysis.

Table 7.8: Proportionality Constants for Empirical Backscatter Relationships

Data Set		$B \propto \sqrt{[Z(Z+1)/A]}$		$B \propto \log(Z+1)$	
		k	r^2	k	r^2
d_{max}	TIGER	0.198 ± 0.008	.99	0.025 ± 0.01	.98
	Experiment	0.198 ± 0.004	.99	0.026 ± 0.02	.94
R_{20}	TIGER	0.19 ± 0.01	.98	0.026 ± 0.01	.98
	Experiment	0.188 ± 0.007	.99	0.025 ± 0.02	.96
R_5	TIGER	0.27 ± 0.03	.92	0.036 ± 0.03	.96
	Experiment	0.24 ± 0.03	.92	0.033 ± 0.002	.97

No significant differences in the proportionality constants derived from experimental data and simulations for either empirical relationship were found for all data sets. In addition, results for d_{max} and R_{20} were found to be consistent, yet significantly different from those for R_5 to 3 standard deviations (>99% confidence level).

Figure 7.38: Empirical backscatter factor relationship (Baily 1980)

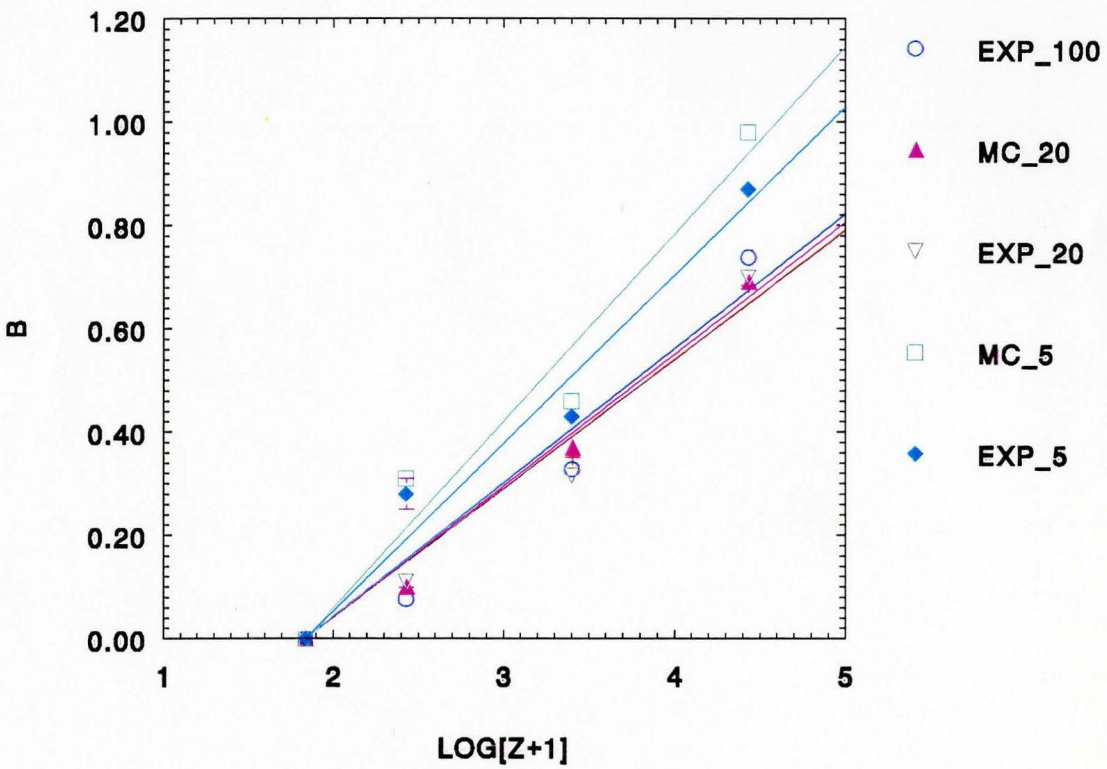

Figure 7.39: Empirical backscatter factor relationship (Mladjenovic 1970)

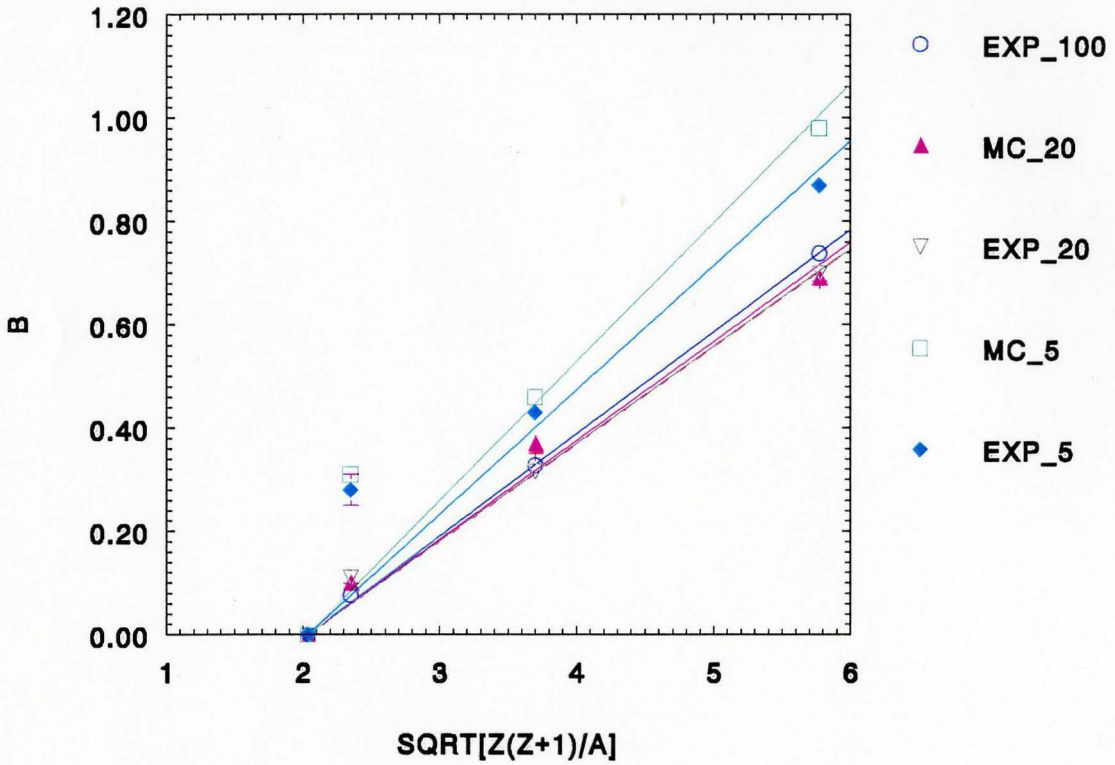

PART IV: DISCUSSION AND CONCLUSIONS

8. Techniques and Results

8.1 Determination of Beam Energy Spectra for Monte Carlo Simulations

The 6MeV electron beam spectrum for the linear accelerator used in the experiments was determined to enable consistent Monte Carlo simulation of experimental conditions. Methods were developed to first obtain the beam energy distribution at 100cm SSD, and then to correct that spectrum for energy degradation in the air gap resulting from variation in SSD. The former was determined as the combination of a set of monoenergetic energy deposition kernels in water, for which weights were optimized to match experimental data. The SSD correction was made by applying the CSDA energy loss model.

Monte Carlo simulation of the depth-dose distribution in polystyrene, based on an input beam spectrum derived from the application of the above two methods, showed high correlation with parallel plate measurements. Thus, there is good evidence to suggest that the spectrum determined through this method is an accurate representation of the true spectrum. This self-consistency does not, however, preclude the effects of systematic errors in the Monte Carlo simulation itself.

In comparing the derived energy spectrum for linac 21-C with the work of Ding *et al.* (Ding 1994), it was observed that the method employed in this work provided good overall agreement with the energy spectrum derived from Monte Carlo simulation of the treatment head using a different code. However, overestimation of the low energy component of the beam spectrum derived in this work relative to that of Ding *et al.* was found. The latter incorporated three-dimensional geometry and thus included the effects of oblique incidence of fluence at the surface.

Large low energy tails were seen in the derived spectra for spectra determined for each of the three machines in this work. It is likely that the methodology used overestimated this component, since the angular distribution of the incident fluence is not considered in the one-dimensional geometry assumed for the generation of the energy deposition kernels. Electrons in the beam may have experienced significant large angle scattering and highly inelastic scattering within the treatment head (Deasy 1994). These electrons, arriving at the treatment surface obliquely, will therefore deposit their energy in shallower depths than normally incident electrons. Thus, the apparent fluence required to generate the shallow depth-dose response, assumed to be perpendicularly incident in this method, will be greater than the actual fluence at low energies. The optimization process compensates for this effect by artificially elevating the low energy components.

Application of the CSDA model was found to be an adequate means of determining the electron beam energy spectrum at 60cm SSD from data at 100cm SSD. It should be noted that this approach also neglects the effects of scatter and thus is likely to be applicable only to small excursions, relative to the electron range, from the SSD of the known (or derived) incident energy fluence spectrum.

In summary, this work and the work of other investigators (Kovář 1983, Altschuler 1992) have shown that electron beam energy spectra can be successfully derived through variance reduction optimization techniques involving monoenergetic energy deposition kernels and standard depth-dose measurement data. In addition, this work has demonstrated that correction for SSD can be achieved through application of the CSDA model for energy degradation in the corresponding air gap.

8.2 Radiochromic Film Dosimetry

8.2.1 Sensitometry of GAFChromic Type 37-041 Film

The characteristic absorption spectrum of irradiated radiochromic film was investigated and found to have several implications on techniques of dose recovery. It was observed that spectral selection can affect both the linearity and sensitivity of response. These effects can be explained by the locations of absorbance peaks and troughs within the spectrum, and by the dose-induced shift in the entire spectrum. For example, many commercial film digitizers use a HeNe laser source (632.8nm). Since this wavelength corresponds to the trough of two absorbtion peaks, this arrangement provides excellent linearity of response but relatively low sensitivity. Similarly, since the characteristic shape of the spectrum was found to be invariant with dose, broadband densitometers can also be expected to provide linear response. It was observed that sensitivity could be maximized by selecting wavelengths corresponding to the major absorbtion peak at ~660nm.

In comparing the two systems used in the spectrophotometry and sensitometry analyses, the RIT113 scanning densitometry system showed substantially higher precision in optical density measurements. The relatively high errors associated with measurements made with the spectrophotometer

can be attributed to electronic noise and temperature-induced drift in the diode detector of the instrument. The RIT113 system featured a temperature controlled photo-multiplier tube (PMT), and thus exhibited less noise. In addition, the PMT offers a greater range of sensitivity in terms of measurable optical density and hence, absorbed dose. A scanning densitometer similar to the RIT113 system with provision for spectral selection and/or frequency-domain scanning would be advantageous. This could be accomplished by replacing the HeNe laser source with either a tunable laser source, or with a broadband source and coupling of the detector through a monochromater.

While the manufacturer of GAFChromic Type 37-041 film quotes a minimum sensitivity of 7.5Gy, this work showed that accuracy to within 1% was achieved with the RIT113 scanning densitometry system over the range of doses from 300Gy to 2Gy. Thus, the minimum sensitivity is below 2Gy at 632.8nm. In addition, it was demonstrated that the lower limit on sensitivity could be improved through spectral selection. It is therefore conceivable that measurements in the sub-Gray range may be attainable using this film through scanning over a frequency range encompassing the main absorption peak (i.e. 630nm to 690nm) for each dose reading, rather than reliance on single wavelength measurements.

The response of GAFChromic Type 37-041 film was observed to exhibit significantly different response to irradiation with ^{60}Co and 6MeV electron radiations in this work, and previous investigators have observed a photon energy dependence for this film (Chiu-Tsao 1994). These findings contradict claims by the distributor of this film, and no similar energy dependence was observed for the less sensitive Type 37-040 film (McLaughlin 1990). However, no energy dependence was seen for nominal 6MeV electrons, over the region from the surface ($<E_0>=5.1MeV$) to R_{20} ($<E>=0.8MeV$). These observations can be explained by the inherently different energy deposition mechanisms of photon and electron radiations. As discussed in Chapter 2, electrons undergo torturous paths in media, experiencing a large number of small energy deposition events in a slowing-down process. While electron stopping power is relatively insensitive to energy for $E \geq 0.1MeV$, photon interaction cross-sections exhibit a strong dependence on energy, particulary over the region $E < 2MeV$ where photoelectric effect is the dominant interaction mechanism (Knoll 1989). A rigorous investigation of the energy response of GAFChromic Type 37-041 film to various qualities of photon and electron radiations was not reported at the time of the writing of this report. Such an investigation is certainly warranted.

8.2.2 Experimental Technique: Strip Film Measurements

Novel Radiochromic film dosimetry techniques were developed for this work in the collection and analysis of strip film measurements of depth-dose distributions resulting from various backscattering geometries. The following section describes some of the implications of these techniques, including the presence of film handling artifacts, alignment of the film, and interpretation of data collected.

Artifacts

In the course of conducting preliminary experiments in this work, it was observed that the dose recovered from regions within approximately 2mm from a film edge was perturbed. This artifact was likely due to detection of source light that had scattered about the film edge. In order to compensate for this effect, films were folded during backscattering experiments such that the readable portion of film would be extended past the position of the interface. The resultant permanent fold artifact served a useful role as marker for precise alignment of film data. This artifact, however, was seen to perturb the distribution of optical density in a region (0.3-0.5mm) immediately upstream of the interface, rendering data in this region unusable. Loss of this data was partially compensated for by the inclusion of spot film data in the analysis of strip film results; however, several critical data points were lost for each strip

film measurement. Since the fitting process used employs a χ^2 variance reduction algorithm, and B(x') decreases exponentially from the interface, the fitting process is intrinsically more sensitive to points near the interface where B is the largest. In addition, the relatively small distance over which non-trivial backscatter occurred, particulary in the case of results at R_5, would have compounded this effect. Thus, it would have been advantageous to have been able to recover distribution of optical density on strip films up to the interface.

One possible solution to the problem of data corruption near the interface due to the above film handling artifacts would be to extend the film strip into the backscatterer. The backscattering materials would thus be split into two segments (as the measurement phantom was), or have a slot cut, into which the film would extend. This design would also have the advantage of providing measurement of the dose within the second layer material downstream from the interface.

Alignment

Alignment of the strip film data made use of the fold artifact as a marker. This offered a distinct advantage over alignment using the proximal film edge since the positioning error due to misalignment of the film during scanning was minimized for points nearest the interface. It is possible that some of the discrepancies observed in experiments, particularly those with air as the

scatterer, were due to misalignment, rather than real phenomena. Since the proximal edge of the film was used as the point of reference for the film for the polystyrene/air interface, positioning errors would have been maximal at the critical points near the interface.

It was assumed in the analysis that film alignment between homogeneous and heterogeneous in the process of dose enhancement calculation was accurate to within one step, or approximately 0.1mm. It was thus assumed that the width of the fold artifact and the position of its peak was highly reproducible relative to the location of the interface in all films. Good agreement between the observed backscatter factor for the spot films and the backscatter amplitude for the strip films suggests that film alignment was satisfactorily achieved. If similar experiments are to be conducted in the future, marking of reference points on the film at either edge of the phantom would enable precise alignment of all films, thus minimizing the effects of alignment errors.

Point Spread Function

Since the source-detector arrangement of the scanning densitometer had a finite spot size, and the backscatter factor varies non-linearly with distance, some inherent averaging would have occurred in the scanning of each point along the dose profiles recorded in strip films. The effect of this averaging

process would be to underestimate the magnitude of B(x') in the region near the interface, and to subsequently underestimate the backscatter amplitude at the interface. While measurement of the point spread function PSF for the scanning densitometer was beyond the scope of this work, a more thorough analysis involving the determination of the PSF would determine whether this effect is significant. If this averaging was found to be significant, de-convolution of the observed optical density profile with the PSF could provide a more accurate measure of the spatial distribution of backscatter recovered from film data.

8.3 Heterogeneity Experiments

8.3.1 Comparison of Experimental Results and Monte Carlo Simulations

Backscatter factors determined from spot films placed at the interface in each backscattering experiment were compared directly to those predicted by TIGER simulation. Since the dose scoring regions in the latter were of equivalent thickness to the film (~0.1mm), the region immediately upstream from the interface provided reasonable simulation of the region occupied by film during the experiments. Backscatter factors calculated from the experimental results and simulations showed agreement for all scattering materials at all interface depths, within their respective limits of uncertainty.

Standard errors predicted for the backscatter factor from both methods are relatively large, particularly in situations where the backscatter amplitude B is small (i.e. air and bone). Characterization of the variation of backscatter factor with distance from the interface through curve fitting provided more precise estimation of B through the incorporation of a large number of data points.

Fitting of the data for high atomic number materials (copper and bismuth) showed consistently high correlation with the single exponential function at

each interface depth. For the air and bone-equivalent-plastic scatterers, correlation was considerably lower, yet reasonable (with the exception of the data for air at R_5 where correlation was extremely poor). While good general agreement was found between the backscattering amplitude determined for experimental and Monte Carlo results, significant differences were found for two solid scatterers (Bi at d_{max} and Cu at R_{20}). Results for air showed significant differences at two interface depths, d_{max} and R_5; however, poor correlation in the latter may discount this finding.

Relaxation lengths determined for the backscatter function showed increases in relaxation length with both atomic number of the scatterer and with energy. These trends are both consistent with the model of backscatter presented in Section 2.5, since higher values of these two factors lead to an increase in the energy of the backscattered electrons. Significant differences in the relaxation lengths determined for experimental and simulation data were found, however, for the majority of cases considered. In general, the relaxation lengths predicted by the Monte Carlo code TIGER were larger than those determined experimentally (exceptions include air interfaces, and bismuth and copper at R_5). Thus, the average upstream distance in which backscattered electrons travel (and deposit their energy) predicted by the code was greater than that observed in the experiments. A similar pattern was observed by Nunes (1992) in the comparison of extrapolation chamber measurements and

simulations using the CYLTRAN code (this work characterized the backscatter in air/Mylar and aluminum/Mylar interfaces using an isotropic ^{32}P β-source). These data may suggest that the ITS codes overestimate the energy of backscattered electrons, or underestimate the stopping power of such low energy electrons.

The discrepancies found between Monte Carlo predictions and the results of the strip film experiments discussed above may point to deficiencies in the Monte Carlo code in dealing with the complex interactions governing electron backscatter phenomena. However, they might also be the result of systematic errors introduced through the experimental techniques (Section 8.2.2) or those introduced in the specification of input parameters for the simulations (i.e. beam energy distribution). There is a lack of benchmark electron backscatter data applicable to the conditions of the experiments in this work (Eisen 1972, Seltzer 1987, Nunes 1991, Tabata 1992, Kwok 1994). In addition, since replicate measurements were not made, the magnitude of random errors due to the data recovery methods could not be quantified absolutely. Thus, definite conclusions cannot be made as to the source or significance of these discrepancies from this data alone.

8.3.2 Characterization of Backscatter

The following general trends in the variation of backscatter with atomic number and with electron energy for the solid scatterers were observed. For a given energy distribution (i.e. depth of interface), backscatter was seen to increase with atomic number. In addition, empirical relationships of the forms $B \propto \sqrt{\frac{Z(Z+1)}{M}}$ (Mladjenovic 1970) and $B \propto \log(Z+1)$ (Baily 1980) for backscatter showed good general agreement with experimental and Monte Carlo results. Backscatter was the greatest for each solid scatterer at the lowest energy (R_f). However, the backscatter factors at d_{max} and R_{20} for these materials consistently showed no significant difference, while those at R_5 were substantially higher. The backscatter factor for the polystyrene/air interface was observed to decrease with depth of interface. The following discussion will attempt to explain these findings in light of the underlying physics of electron backscatter and in the context of work by previous researchers.

In this work, the energy dependence of backscatter was investigated. Selectivity in the energy spectrum at the interface was achieved by increasing the thickness of the first layer of polystyrene in the phantom. Hence, it was possible to vary the average energy of the electrons at the interface, while

keeping the initial energy constant. Because of this arrangement, it is important to consider that the fluence, which is highly forward-directed at the surface, becomes more isotropic with depth. Electrons at greater depths of interface therefore experience, on average, greater obliquity of incidence and require smaller scattering angles from scattering interactions to re-emerge from the scatterer. Backscatter is thus expected to increase both with obliquity and with depth. This pattern in the variation of backscatter with obliquity has been observed through the work of Berger (1963), in the calculation of electron albedo from the backscattering of isotropic point sources and electron beams at various angles of incidence. In Chapter 4 it was stated that backscatter increases as energy is decreased. Since the decrease in energy with depth is accompanied by an increase in isotropy, it follows that the increase in backscatter with depth due to energy would be compounded by the increase in backscatter due to isotropy.

When the results for solid scatterers are analyzed under this light, the increase in backscatter observed at R_5 for each material, relative to the two shallower depths, is consistent with the above arguments. However, the backscatter factors for each material at d_{max} and R_{20} did not show significant differences even though the difference in average energy for d_{max} and R_{20} (0.41MeV) is greater that for R_{20} and R_5 (0.21MeV), and the fluence at d_{max} is expected to be more forward-directed than that at R_{20}. Therefore, the

invariance of backscatter over d_{max} and R_{20} is not explained by the effects of energy or angular fluence distribution discussed.

Since the lateral dimensions of the phantom are much smaller than the electron range in air, conditions of laterally infinite geometry do not apply to air interfaces. It can thus be assumed that the presence of air is best represented by a vacuum, since it is extremely unlikely that an electron backscattered from air would re-enter the measurement phantom in the film-containing region, if at all. Fluence which crosses the interface is effectively lost, and the air interface experiments and simulations therefore serve to measure the backscatter due to the presence of a homogeneous scatterer. The above description would therefore predict an increase in the magnitude of the backscatter factor with depth of interface for the polystyrene-air interface. However, the opposite effect was observed in both experiment results and Monte Carlo simulations. Kwok *et al.* (Kwok 1994) have investigated the backscatter factor for low energy β-sources (^{32}P, ^{204}Tl, and ^{147}Pm; end point energies 1.710MeV, 0.766MeV, and 0.224MeV, respectively) and they have also observed an increase in the backscatter with increasing energy for tissue-air interfaces.

Experimental data obtained by Klevenhagen *et al.* (Klevenhagen 1982) for high energy electron backscatter show a monotonic decrease in the electron backscatter factor with energy above 5-7MeV and indicate a peak in

backscatter over this region. Subsequent experiments and additional Monte Carlo simulation at lower energies ($\geq$3.3MeV) performed by Tabata and Ito (Tabata 1992) also suggest that the electron backscatter factor may initially increase with energy, reach a maximum, and then decrease monotonically. They also found that the relationship between B and Z showed very little variation for mean energies of 3.3MeV and 5.5MeV. In this work, it was similarly observed that the relationships of B versus Z (based on the two empirical expressions) showed insensitivity to electron energy at d_{max} ($<E>=2.3$MeV) and R_{20} ($<E>=0.79$MeV). The electron backscatter factor at lower energy (R_5), however, was seen to increase significantly in this work, as evidenced by the backscattering data and the fitting of the empirical backscatter relationships.

Nunes (1992), in Monte Carlo simulation of the backscatter factor for monoenergetic low energy electrons, has reported an initial increase in the backscatter factor over the range of 0.1MeV to 0.5MeV, which is followed by a decrease in the region of 0.8MeV to 1.8MeV. While this is consistent with the variation in backscatter with energy observed in this work, there is an obvious discrepancy between these findings and those of Klevenhagen (1982) and Tabata and Ito (Tabata 1992).

Clearly, there is a need for further investigation of electron backscatter phenomena at low energies, particularly over the region 0-5MeV and for air interfaces, in which the effects of both the energy and angular distributions of fluence are properly taken into account.

9. Summary and Recommendations for Future Work

The primary objective of this project, quantification of absorbed dose perturbation at tissue interfaces, has been satisfactorily met. In addition, the radiochromic film dosimetry and Monte Carlo simulation tools and methodologies, which have been developed in the process of executing this work, have been demonstrated to be useful and applicable beyond the scope of this specific problem.

The results of the backscattering experiments and Monte Carlo simulations showed good general agreement; however, several discrepancies were found between observed phenomena and Monte Carlo predictions. Further investigation of the sources of these discrepancies is required in order to determine whether they arose from deficiencies in either experimental or simulation techniques. The methodologies employed in this work are believed to be sound. Thus, the generation of replicate data and implementation of improvements to experimental techniques discussed in Section 8.2.2 should verify the sources and significance of these discrepancies conclusively and provide data in the critical region very close to the interface.

In a broader sense, there is a need for further investigation of backscatter phenomena at low electron energies (0-5MeV) since current data in this region is ambiguous. The source of this ambiguity can be traced to the different conditions under which experiments have been conducted. Specifically, the angular and energy distributions of electron fluence must be incorporated into the analysis in order to establish suitable benchmark data in this nebulous region. It is hoped that this work has contributed to that end, and that it will be extended in further studies to provide a clear understanding of backscatter phenomena in this region.

Radiochromic film dosimetry techniques were found to be well suited for this investigation. It is expected that this medium will become an established dosimetry tool within the medical physics community for both research and clinical dosimetry applications in the near future. There is, however, a need for rigorous sensitometry of Type 37-041 GAFChromic film in order to quantify its energy response characteristics. In addition, further work with this media, aimed at determining and improving its minimum sensitivity, should be undertaken.

APPENDIX I

PROGRAM LISTING: BEAMSPEC.BAS (QuickBASIC)

```
REM     BEAMSPEC.BAS                    Fuad Khan 1994
REM
REM     ------------------------------------------------------
REM
REM     This program uses a variance reduction algorithm to
REM     determine the beam energy spectrum for 6MeV linear
REM     accelerators. Monoenergetic energy deposition kernels
REM     from Monte Carlo simulation are input from the file
REM     datafile$ (in this case A:\16DATA.ASC).
REM
REM     MAIN PROGRAM
REM     Beginning from the highest energy bin, weights are
REM     sequentially optimized. Weights are adjusted in order
REM     to minimize a variance reduction statistic calculated
REM     from the weighted composite monoenergetic depth-dose
REM     distribution and measurement data.
REM
REM     Subroutine NORMALIZE
REM     This subroutine first calculates the composite depth-dose
REM     curve based on the weighted average of the composite
REM     energy deposition kernels, from the current weights.
REM     This is then normalized (Dmax=1) to correspond to
REM     measurement data and the nu-squared statistic is
REM     calculated for M data points.
REM
REM     Subroutine: GETDATA
REM     The user specifies the input file containing normalized
REM     (Dmax=1) measured depth dose data (at 1mm intervals,
REM     over 34mm) for the linac to be analyzed, and the output
REM     weights file.
REM
REM     Subroutine: HISTOGRAM
REM     Displays the weights as a histogram throughout the
REM     optimization process
REM
```

```
REM     Subroutine:  OUTFILE
REM     Writes current weights to file at each outer iteration
REM     step i.
REM
REM     ------------------------------------------------------

REM define global variables

        datafile$ = "a:\16data.ASC": REM Monte Carlo data file

        inc = .0001
        N = 34: REM number of data points in data file
        MM = 16: REM nummber of energy bins in data file

        DIM x(N), Dm(N)
        DIM DE(MM, N)
        DIM D(N)
        DIM w(MM)
        DIM oldw(N)

REM  get input data

        GOSUB GETDATA

REM first iteration

                SCREEN 2
                GOSUB NORMALIZE:
                oldNu = nu

REM **** main program loop *****

ITERATE:
        FOR I = M TO 1 STEP -1

100             LOCATE 1, 4: PRINT "+"
                w(I) = w(I) + inc:
                GOSUB NORMALIZE
                IF nu < oldNu THEN oldNu = nu: GOTO 100
                w(I) = w(I) - inc

200             LOCATE 1, 4: PRINT "-"
                w(I) = w(I) - inc
```

```
150
            IF w(l) < 0 THEN w(l) = 0: GOTO 300: REM dissallow negative
weights
            GOSUB NORMALIZE
            IF nu < oldNu THEN oldNu = nu: GOTO 200
            w(l) = w(l) + inc

            LOCATE 1, 4: PRINT " "
            REM update display

300           GOSUB HISTOGRAM

      NEXT l

      GOSUB OUTFILE

      GOTO ITERATE

      END: REM redundant

REM ***** SUBROUTINES *****

NORMALIZE:

      REM re-normalize weights and calculate Nu-squared statistic

            SUM = 0
            FOR i = 1 TO M
                  SUM = SUM + w(i)
            NEXT i
            FOR i = 1 TO M
                  w(i) = w(i) / SUM
            NEXT i

      REM calculate weighted depth-dose estimate: D(x(j))

            FOR j = 1 TO N
                  D(j) = 0
                  FOR i = 1 TO M
                        D(j) = D(j) + w(i) * DE(i, j)
                  NEXT i
            NEXT j

      REM normalize
```

```
        MAX = 0
        FOR j = 1 TO N:
            IF D(j) > MAX THEN MAX = D(j)
        NEXT j
        FOR j = 1 TO N: D(j) = D(j) / MAX: NEXT j

    REM calculate Nu-SQUARED

        nu = 0
        FOR j = 1 TO N
            nu = nu + ((D(j) - Dm(j)) ^ 2) / Dm(j)
        NEXT j
        IF INKEY$ <> "" THEN GOSUB HISTOGRAM
        LOCATE 1, 1: PRINT I, nu: PRINT inc
        RETURN

REM ***** ***** **

HISTOGRAM:
        IF INKEY$ = "i" THEN GOSUB 7000: REM change increment
        IF INKEY$ = "q" THEN GOSUB OUTFILE: END
        CLS
        xinc = 30
        ymax = 300
        x = 40: y = 190
        PSET (x, y)

        FOR kh = 1 TO M
            LINE -(x, 190 - ymax * w(kh))
            x = x + xinc
            LINE -(x, 190 - ymax * w(kh))
            LINE -(x, 190)
        NEXT kh

        LINE -(x, 190)
        LINE -(40, 190)
        LOCATE 25, 3: PRINT "bin:";
        LOCATE 25, 11:
        FOR i = 2 TO M STEP 2
            PRINT i; "   ";
        NEXT

    RETURN
```

```
7000    PRINT "old inc = "; , inc;
      INPUT ",new inc = "; inc
      RETURN

REM ***** *****

GETDATA:

      REM prompt user for filenames

            INPUT "Number of Bins ", M
            PRINT M
            INPUT "Weights File ", infile$
            PRINT infile$
            INPUT "Depth Dose Datafile ", depdose$
            PRINT depdose$

      REM read in weights file

            OPEN infile$ FOR INPUT AS #2
                  FOR i = 1 TO M
                        INPUT #2, w(i)
                  NEXT i
            CLOSE #2

      REM read in Monte Carlo data

            OPEN datafile$ FOR INPUT AS #1
            FOR j = 1 TO N
                  INPUT #1, x(j)
                  FOR i = 1 TO MM
                        INPUT #1, DE(i, j)
                  NEXT i
                  INPUT #1, z
            NEXT j
            CLOSE #1

      REM read in measured depth-dose

            OPEN depdose$ FOR INPUT AS #1
            FOR i = 1 TO N
                  INPUT #1, x(i), Dm(i)
            NEXT i
```

```
            FOR j = 1 TO N
            PRINT : PRINT x(j), Dm(j),
                  FOR i = 1 TO MM
                        PRINT DE(i, j),
                  NEXT i
            NEXT j

            RETURN

REM ***** *****

OUTFILE:      REM write current weights to  file

            OPEN infile$ FOR OUTPUT AS #2
            FOR i = 1 TO M
                  WRITE #2, w(i)
            NEXT i
            CLOSE #2

            RETURN

REM ***** END OF FILE *****
```

REFERENCES

Altschuler, M.D., P. Bloch, E.L. Buhle and S. Ayyalasomayajula 1992 3d dose calculations for electron and photon beams *Phys. Med. Biol.* **37** (2) (391-411)

Andreo, P. 1991 Monte Carlo Techniques in Medical Radiation Physics *Phys. Med Biol.* **36** (861-920)

Attix, F.H. 1986 *Introduction to Radiological Physics and Radiation Dosimetry* Toronto: John Wiley and Sons, Inc.

Baily, N.A. 1980 Electron backscattering *Med. Phys.* **7** (5) (514-519)

Berger, M.J. 1963 Monte Carlo Calculation of the penetration and diffusion of fast charged particles in *Methods in Computational Physics Vol.1* eds. B. Alder, S. Fernback, and M Rotenberg New York: Academmic Press (135-215)

Berger M.J. 1971 Distribution of absorbed dose around point sources of electrons and beta particles in water and other media *J. Nucl. Med.* Supplement No.5 (5-23)

Bialobzyski, P.J. 1987 *Electron dose distribution near planar tissue-bone interfaces* MSc Project McMaster University: Hamilton, Ontario

Brahme, A., and H. Svensson 1976 Specification of electron beam quality from the central-axis depth-absorbed distribution *Med. Phys.* **3** (95-102)

Cenic, A. 1994 *Evaluation of the response of a new radiochromic dosimeter to low gamma radiation doses* BSc Research Project McMaster University: Hamilton, Ontario

Chiu-Tsao, S.T., de la Zerda, A., Lin, J., Kim, J.H. 1994 High-sensitivity GafChromic film dosimetry for ^{125}I seed, *Med Phys.* **21** (5)

Cross, W.G. 1968 Variation of beta dose attenuation in different media *Phys. Med. Biol.* **13** (4)

Deasy, J.O., R.P. Almond, and M.T. McEllistrem 1994 The spectral dependence of electron central-axis depth-dose curves *Med. Phys.* **21** (9)

Ding, G. 1994 private communication

Dutreix, J. and Dutreix A. 1969 Film dosimetry of high energy electrons *Ann N.Y. Acad. Sci.* **161** (33-42)

Eisen, H., Rosenstein, M., and Silverman, J. 1972 Electron depth-dose distribution measurements in two-layer slab absorbers *Radiation Research* **52** (429-447)

Evans, R.D. 1955 *The Atomic Nucleus* London: McGraw Hill Book Co. Inc.

Halbieb, J.A., R.P. Kensek, T.A. Mehlhorn, G.D. Valdez, S.M. Seltzer, and M.J. Berger 1992 *ITS Version 3.0: The Integrated TIGER Series Coupled Electron/Photon Monte Carlo Transport Codes* SAND91-1634, Sandia National Laboratories, Albequerque, New Mexico

Harder, D. 1966 in *Biological Aspects of Radiation Quality* STI/DOC/10/58 Vienna, IAEA

Harvey, R.A., L.L. Haas, and J.S. Laughlin 1952 Betatron cancer therapy, *Radiology*, **58**

ICRU Report 21 1974 *Radiation dosimetry: electrons with initial energies between 1 and 50 MeV* International Commission on Radiation Units and Measurements, 7910 Woodmont Avenue, Bethsda MD 20814, U.S.A

ICRU Report 35 1984 *Radiation Dosimetry: Electron Beams with Energies between 1 and 50MeV* International Commission on Radiation Units and Measurements, 7910 Woodmont Avenue, Bethsda MD 20814, U.S.A

ICRU Report 37 1984 *Stopping Powers for Electrons and Positrons* International Commission on Radiation Units and Measurements, 7910 Woodmont Avenue, Bethsda MD 20814, U.S.A

Khan, F.M. 1984 *The Physics of Radiology* Williams and Wilkins Baltimore U.S.A.

Khan, F.M., K.P. Doppke, K.R. Hogstrom, G.J. Kuther, R. Nath, S.C. Prasad, M. Rozenfeld, and B.L. Werner 1991 Clinical electron-beam dosimetry: Report of AAPM Radiation Therapy Committee Task Group No.25 *Med. Phys.* **18** (1)

Klevenhagen, S.C., 1988 Current status of electron therapy - clinical and physical aspects, *Brit. Jour. Radiol. Supplement* **22**

Klevenagen, S.C., G.D. Lambert, and A Arbabi 1982 Backscattering in electron beam therapy for energies between 3 and 35 MeV *Phys. Med. Biol.* **27** (3)

Kovář I., J. Novontnỳ, Z. Kovář, P. Jiroušek and S. Vávra 1983 Calculation of energy spectra for therapeutic electron beams from depth-dose curves *Phys. Med. Biol.* **28** (12)

Kwok C.S., M. Irfan, M. Woo, and W.V. Prestwich 1987 effect of tissue inhomogeneity on beta dose distribution of ^{32}P *Med. Phys.* **14** (1)

Kwok C.S., P.J. Bialobzyski, and S.K. Yu 1991 Effect of tissue inhomogeneity on dose distribution of continuous activity of low-energy electrons in bone marrow cavities with different topologies *Med. Phys.* **18** (3)

Kwok C.S. 1994 private communication

Landau L. 1944 On the Energy Loss of fast Charged Particles by Ionization *Journal of Physics* **8** (4) (201-205)

McCracken, D.D. 1953 The Monte Carlo Method *Science* **192** (90-96)

McLaughlin, W.L., A. Miller, K. Pejtersen, and W. Batsberg Pedersen 1977 Radiochromic plastic films for accurate measurement of radiation absorbed dose and dose distributions *Radiat. Phys. Chem* **10** (119-127)

McLaughlin, W.L., A. Miller, R.M. Uribe, S. Kronenberg and C.R.d Seibertritt 1985 "Energy dependence of radiochromic dosimeter response to x- and γ-rays", High Energy Dosimetry, IAEA Publication STT/PUB/691, Vienna (397-424)

McLaughlin, W.L., Yun-Dong, C., Soares, C.G. 1991 Sensitometry of the response of a new radiochromic film dosimeter to gamma radiation and electron beams, *Nuclear Instruments and Methods in Physics Research* A302

McLaughlin, W.L., Soares, C.G., Sayeg, J.A., McCullough, E.C., Kline, R.W., Wu, A., Maitz, A.H. 1994 The use of a radiochromic detector for the determination of stereotactic radiosurgery dose characteristics, *Med. Phys.* **21** (3)

Meigooni A.S. and I.J. Das 1987 Parameterization of depth dose for electron beams *Phys. Med. Biol.* **32** (6)

Mladjenovic, M. 1973 *Radioisotope and radiation physics, An introduction* New York: Academic Press

Meuench, P.J., A.S. Meigooni, and R. Nath 1991 Photon energy dependence of the sensitivity of radiochromic film and comparison with silver halide film and LiF TLDs used for brachytherapy dosimetry, *Med. Phys.* **18** (4)

Nunes, J.C. 1991 *Boundary electron and beta dosimetry - quantification of the effects of dissimilar media on absorbed dose* PhD Thesis McMaster University: Hamilton, Ontario

Peters, V. 1994 private communication

Prestwich, W.V. 1994 private communication

Prestwich, W.V., J. Nunes, and C.S. Kwok 1989 Beta dose point kernels for radionuclides of potential use in radioimmunotherapy *J. Nucl. Med.* **30** (1036-1046)

Raeside, D.E. 1976 Monte Carlo Principles and Applications *Phys. Med. Biol.* **21** (181-197)

Ramani, R., Lightstone, A.W., Mason, D.L.D., O'Brien, P.F. 1994 The use of radiochromic film in treatment verification of dynamic stereotactic radiosurgery, *Med. Phys.* **21** (3)

Ritt, D. 1994 private communication

Rogers, D.W.O., and A.F. Bielajew Monte Carlo techniques of electron and photon transport for radiation dosimetry in Kase, K.R., E.B. Bjärngard, F.H Attix 1986 *The Dosimetry of Ionizing Radiation Volume III.* San Diego: Academic Press, Inc.

Rutherford, E. 1911 The scattering of alpha and beta particles by matter and the structure of the atom *Philosophical Magazine* **20** (669-688)

Saylor, M.C., Tamaroo, T.T., McLaughlin, W.L., Khan, H.M., Lewis, D.F., and R.D. Schenfele 1988 A thin film recording medium for use in food irradiation, *Radiat. Phys. Chem*, **31** (529-536)

Schultz, R.J., p.R. Almond, J.R. Cunningham, J.G. Hlt, R. Loevinger, K.A. Wright, R. Nath, and G.D. Lempert 1983 A protocol for the determination of absorbed dose from high-energy photon and electron beams, *Med. Phys.* **10** (6)

Seltzer S.M. and M.J. Berger 1987 Energy deposition by electron, bremsstrahlung, and ^{60}Co gamma-ray beams in multi-layer media *Appl. Radiat. Isot.* **38** (5)

Tabata, T. and Ito, R. 1992 Simple calculation of the electron-backscatter factor *Med. Phys.* **19** (6)

Turner, J.E., H.A. Wright and R.N. Hamm 1985 A Monte Carlo Primer for Health Physicists *Health Physics* **48** (717-33)

Wierzbicki, W., and E.B. Podgorsak 1994 An analytical expression for electron central axis depth doses *Med. Phys.* **21** (6)

Wyman, D., private communication

Yu, S.K. 1989 *Dosimetry of electron sources near planar tissue interfaces* MSc Project McMaster University: Hamilton, Ontario